Universidade de Aveiro Departamento de Engenharia de Materiais e Cerâmica
Ano 2017

Ricardo Manuel Fonseca Lopes Silva

Heteroestruturas de óxido metálico/nanotubos de carbono para condensadores de dupla camada elétrica

Metal oxide/carbon nanotubes heterostructures for electric double layer capacitors

Universidade de Aveiro
Ano 2017
Departamento de Engenharia de Materiais e Cerâmica

Ricardo Manuel Fonseca Lopes Silva

Heteroestruturas de óxido metálico/nanotubos de carbono para condensadores de dupla camada elétrica

Metal oxide/carbon nanotubes heterostructures for electric double layer capacitors

Dissertação apresentada à Universidade de Aveiro para cumprimento dos requisitos necessários à obtenção do grau de Doutor em Ciência e Engenharia de Materiais, realizada sob a orientação científica do Doutor Rui Ramos Ferreira e Silva, Professor Associado do Departamento de Engenharia de Materiais e Cerâmica da Universidade de Aveiro, e co-orientação científica do Doutor Nicola Pinna, Professor do Departamento de Química da Universidade de Humboldt

This work was developed within the scope of the project CICECO-Aveiro Institute of Materials, POCI-01-0145-FEDER-007679 (FCT Ref. UID/CTM/50011/2013), financed by national funds through the FCT/MEC and when appropriate co-financed by FEDER under the PT2020 Partnership Agreement.

Apoio financeiro da FCT no âmbito do III Quadro Comunitário de Apoio.
FCT grant SFRH/BD/90844/2012

o júri

presidente

Prof. Doutor Amadeu Mortágua Velho da Maia Soares
Professor Catedrático da Universidade de Aveiro

Prof. Doutor Mário Guerreiro Silva Ferreira
Professor Catedrático da Universidade de Aveiro

Prof. Doutor Nicola Alessandro Pinna
Full Professor at the Humboldt-Universität, Berlim, Alemanha

Prof. Doutor Mato Knez
Professor at the Technical University of Navarra (TECNUN), San Sebastian, Spain e Professor (Research) at the IKERBASQUE Foundation for Science, Bilbao, Spain

Prof. Doutor António Jorge Duarte de Castro Silvestre
Professor Coordenador do Instituto Superior de Engenharia de Lisboa

Prof. Doutor Lifeng Liu
Investigator Principal at the International Iberian Nanotechnology Laboratory (INL)

agradecimentos

The work presented in this manuscript was developed in a joint collaboration between the Department of Materials and Ceramic Engineering/CICECO-Aveiro Institute of Materials, University of Aveiro, Aveiro, Portugal and Institut für Chemie, Humboldt-Universität zu Berlin, Berlin, Germany.

First and foremost, I am most grateful to my supervisors, Prof. Dr. Rui Silva and Prof. Dr. Nicola Pinna, for giving me the opportunity to begin this PhD adventure and for driving me through it. I would like to say that I greatly appreciated their confidence, enthusiasm, advice, help and understanding during these four years. I would like to acknowledge the examination committee. In particular, Prof. Dr. Mato Knez and Prof. Dr. António Silvestre for agreeing to be external examiner and for carefully checking this manuscript.

Drª. Rosário Soares and António J. S. Fernandes, from University of Aveiro, are acknowledged for their technical assistance and fruitful discussion on X-ray reflectrometry, grazing incident X-ray diffraction and Raman measurements, respectively. MSc Marta Ferro, MSc Bruno Almeida, Drª. Ana V. Girão and Drª. Guylhaine Clavel, from University of Aveiro and Humboldt-Universität zu Berlin, respectively, are acknowledge for their help and contribution in scanning electron microscopy and transmission electron microscopy. Drª. Joyce R. Araujo, Prof. Dr. Carlos A. Achete and Dr. Patrick Amsalem, Prof. Dr. Norbert Koch from Materials Metrology Division, INMETRO, Brazil and Humboldt-Universität zu Berlin, respectively, are acknowledged for their contribution in X-ray photoelectron spectroscopy measurements and interpretation. I would also to acknowledge Dr. Alexandre Bastos and Yafei Fan from University of Aveiro and Humboldt-Universität zu Berlin, respectively for your support and assistance in the electrochemical measurements.
I would like to thank, all the people working at the University of Aveiro and Humboldt-Universität zu Berlin that helped me.

This work received the financial support from FCT (Fundação para a Ciência e a Tecnologia) for the grant SFRH/BD/90844/2012. This work was also developed within the scope of the project CICECO-Aveiro Institute of Materials, POCI-01-0145-FEDER-007679 (FCT Ref. UID /CTM /50011/2013), financed by national funds through the FCT/MEC and when appropriate co-financed by FEDER under the PT2020 Partnership Agreement.

palavras-chave

Deposição por camada atómica, óxidos metálicos, deposição química em fase de vapor, nanotubos de carbono, heteroestruturas, condensadores eletroquímicos.

resumo

O presente estudo teve como objetivo principal a elaboração e caracterização de hétero-estruturas hibridas tridimensionais (3D) de nanotubos de carbono alinhados verticalmente e revestidos com óxido de manganês para aplicações em condensadores eletroquímicos como elétrodos livres de aditivos.

Numa primeira fase, foram desenvolvidas metodologias para o crescimento de nanotubos de carbono puro e para nanotubos de carbono dopados com azoto, em substratos isoladores e metálicos, por deposição química em fase de vapor. Foi dada especial atenção ao crescimento direto de nanotubos de carbono alinhados verticalmente no substrato metálico (Inconel®600) e sua aplicação em elétrodos livres de aditivos à base de carbono. Posteriormente, foi desenvolvido um processo inovador para a deposição de óxido de manganês (Mn_3O_4) por deposição por camada atómica para o revestimento de nanoestruturas, como os nanotubos de carbono, para a elaboração de heteroestruturas. Estas foram devidamente caracterizadas como materiais para aplicações em eléctrodos. A eficiência electroquímica dos eléctrodos atinge um máximo para o nanocompósito de nanotubos de carbono puro/óxido de manganês revestidos com 600 ciclos por deposição por camada atómica e apresenta uma capacitância de 78.68 mF cm^{-2} a 5 mV s^{-1}. Este resultado pode ser atribuído ao efeito cooperativo entre os componentes do nanocompósito e uma utilização eficaz dos materiais ativos. Provou-se que um material nanocompósito que englobe a capacitância da dupla camada elétrica, bem como a estrutura condutora dos nanotubos de carbono e a pseudo-capacitância dos óxidos metálicos é de grande interesse devido ao seu mecanismo duplo de armazenamento de carga e as vantagens de cada mecanismo são exploradas nestes novos dipositivos híbridos.

Este trabalho foi realizado na Universidade de Aveiro e na Universidade de Humboldt (Berlim), beneficiando das infraestruturas adequadas à execução do trabalho experimental de ambas as instituições e das competências complementares das equipas de investigação associadas. Devido à natureza multidisciplinar da área de investigação onde este doutoramento se insere, a colaboração com outras instituições internacionais valorizaram a discussão dos resultados obtidos e fundamentaram os novos materiais desenvolvidos.

keywords

Atomic layer deposition, metal oxides, chemical vapor deposition, carbon nanotubes, heterostructures, electrochemical capacitors.

abstract

The purpose of this work was the elaboration and characterization of hybrid three-dimensional (3D) arrays of vertically aligned carbon nanotubes coated with manganese oxide heterostructures for application as binder-free electrodes in electrochemical capacitors.

In the first stage, methodologies to grow pure and nitrogen doped vertically aligned carbon nanotubes arrays on nonmetallic and metallic substrates by thermal chemical vapor deposition have been developed. Particular attention was devoted to obtain vertically aligned carbon nanotubes arrays grown directly on metallic conductive substrates (Inconel®600) and their application in binder-free carbon-based electrodes.

Subsequently, as one of the main points of this work, a novel manganese oxide (Mn_3O_4) atomic layer deposition process has been developed for coating nanostructures, such as carbon nanotubes, for the elaboration of heterostructures which were further used and characterized as electrodes materials. The electrochemical performance of the electrodes reaches a maximum for the pure carbon nanotubes/manganese oxide nanocomposite coated with 600 ALD cycles exhibiting a specific capacitance of 78.68 mF cm^{-2} at 5 mV s^{-1}. This result could be attributed to the synergetic effect between the components in the nanocomposite and an effective utilization of the active materials. Therefore it was demonstrated that a nanocomposite material comprising electric double layer capacitance together with the conductive framework of the carbon nanotubes and pseudocapacitive metal oxides is of great interest due to its dual charge storage mechanism and the advantages of each mechanism are exploited in these new hybrid devices.

This work was carried out at University of Aveiro and at Humboldt-Universität zu Berlin due to complementary avaivable expertises and equipments, and also benefits of several international collaborations due to the multidisciplinar nature of the research field.

Index

List of Figures

List of Tables

Abbreviations and Acronyms

AC	Amorphous carbon
AFM	Atomic force microscopy
ALD	Atomic layer deposition
BF-STEM	Bright field scanning transmission electron microscopy
BSE-SEM	Backscattered electrons scanning electron micoscopy
CBED	Convergent beam electron diffraction
CNTs	Carbon nanotubes
CV	Cyclic voltammetry
DoE	Design of experiments
DP	Diffraction pattern
DF	Dark field scanning transmission electron microscopy
EDLCs	Electric double layer capacitors
EDS	Energy dispersive X-ray spectroscopy
EELS	Electron energy loss spectroscopy
EIS	Electrochemical impedance spectroscopy
FAT	Fixed analyzer transmission
FFT	Fast Fourier transform
GDOES	Glow discharge optical emission spectroscopy
GCD	Galvanostatic charge-discharge
GIXRD	Grazing incident X-ray diffraction
GPC	Growth per cycles
HOPG	High oriented pyrolytic graphite
HRTEM	High resolution transmission electron microscopy
JCPDS	Joint committee on powder diffraction

LO	Longitudinal optical mode
N-CNTs	Nitrogen doped carbon nanotubes
PVD	Physical vapor deposition
SAED	Small area electron diffraction
SE-SEM	Secondary electrons scanning transmission electron microscopy
SEM	Scanning electron microscopy
STEM	Scanning transmission electron microscopy
TCVD	Thermal chemical vapor deposition
TEM	Transmission electron microscopy
UHV	Ultra-high vacuum
VACNTs	Vertically aligned carbon nanotubes
VA-N-CNTs	Vertically aligned nitrogen doped carbon nanotubes
XPS	X-ray photoelectron spectroscopy
XRD	X-ray diffraction
XRR	X-ray reflectivity

Symbols

a = b = c	Lattice parameter
A	Ampere
Å	Ångström
Al_2O_3	Alumina
Ar	Argon
C_2H_2	Acetylene
Cr	Chromium
C_{sp}	Specific capacitance

E	Energy density
eV	Electron volt
F	Farad
Fe	Iron
H_2	Molecular hydrogen
Hz	Hertz
I	Current
I(E)	Instantaneous current
IR	Ohmic or voltage drop
LaB_6	Lanthanum hexaboride
Mn	Manganese
Mn_3O_4	Hausmannite (manganese oxide)
N	Nitrogen
NH_3	Ammonia
NiO	Nickel oxide
P	Power density
Si	Silicon
SiC	Silicon carbide
SiO_2	Silica
S/N	Signal to noise ratio
Ta	Tantalum
V	Volt
ZnO	Zinc oxide
-Zi	Internal resistance (imaginary)
Zr	Internal resistance (real)

Greek symbols

Ω	Ohm
π	Bonding orbital
π*	Antibonding orbital
ΔE	Potential range
Δt	Discharge time
θ	Scattering angle
ν	Scan rate
λ	Wavelength

Motivation, objectives and thesis organization

The aim of this thesis is the development of hybrid 3D-arrays of vertically aligned carbon nanotubes coated with transition metal oxide to be used as binder-free electrodes in the field of energy storage systems as supercapacitors. These heterostructures allow combining the electrochemical double layer capacitance of the carbon nanotubes and pseudocapacitance provided by the late transition metal oxide in the charge storage. The development of new and high-efficient electrochemical capacitors is critical for addressing the crucial problems of limited availability of fossil fuels and environmental concerns. On the other hand, these electrochemical energy storage systems can also play a key role in efficient utilization of sustainable and renewable energy sources, such as wind and solar energies.

Among the transition metal oxides, manganese oxide was the selected candidate for replacing the widely used ruthenium oxide which is known as one of the best performing pseudocapacitive materials. The main disadvantages of the latter oxide are the high price and the limited availability which greatly limit its application. In contrast, manganese oxide is naturally abundant, having a relative low cost, environmentally friendly nature, and has high theoretical capacitance. However, the poor electrical conductivity of the manganese oxide limits its applications in supercapacitors. One possible strategy to solve this drawback is to create carbon nanotubes-manganese oxide nanostructured electrodes, to take advantage of both the excellent electrical conductivity of the nanotubes and the high capacitance of the manganese oxide. This way, the electrochemical performance is enhanced by the combination of properties but also by enlarging the contact area between the electrode and the electrolyte.

To achieve high specific capacitance, manganese oxide synthesis methods must provide uniform and conformal coatings of the high surface area electrode (i.e. carbon nanotubes) with nanoscale control of coating thickness. In this context, the atomic layer deposition technique is especially well suited to fulfill these requirements without compromising the support characteristic properties.

The novelty of this work thus lies in the ability to directly grow dense aligned carbon nanotubes on a metallic current collector by chemical vapor deposition (CVD) and coat them with manganese oxide by atomic layer deposition (ALD). As a result, a “ready to use” nanocomposite supercapacitor electrode is prepared. This nanocomposite could be ideal structure for high performance area-limited configurations such as microelectromechanical systems or on-chip devices (i.e. micro-scale energy systems).

The work presented in this thesis was developed in a joint collaboration between the Department of Materials and Ceramic Engineering/CICECO-Aveiro Institute of Materials, University of Aveiro, Aveiro, Portugal and the Institut für Chemie, Humboldt-Universität

zu Berlin, Berlin, Germany, and is divided into main parts: (i) growth of pure and nitrogen doped vertically aligned carbon nanotubes arrays on nonmetallic and metallic substrates by thermal chemical vapor deposition and (ii) the development of a novel strategy of atomic layer deposition of manganese oxide for the elaboration of the vertically aligned carbon nanotubes arrays/manganese oxide heterostructures (nanocomposites) electrodes. This thesis is presented in the form of a compilation of four scientific papers covering the above issues and published in relevant journals of this research area and one last chapter (scientific paper in preparation) reporting a comparative study of the electrochemical properties of nitrogen doped- and pure-carbon nanotubes/manganese oxide nanocomposites as electrodes materials. Before their presentation, an introduction (concept approach and experimental design) is addressed in Chapter I. Finally, the last chapter describes the main conclusions regarding the results obtained under this PhD thesis.

Chapter I

Introduction

This general introduction is organized mainly into two parts. In the first part, it is intended to give some description of the synthesis techniques to obtain three dimensional (3D) nanostructured metal oxide/carbon nanotubes (CNTs) heterostructures targeting energy storage and conversion systems. Particular emphasis was placed on the 3D carbon-based nanostructures coated with pseudocapacitive materials like metal oxides or conductive polymers for electrochemical capacitor applications, as schematically presented in Figure 1. The design of 3D carbon-based nanostructures is definitely important since each of the respective building block's properties can be greatly enhanced if an appropriate nanostructure is chosen.

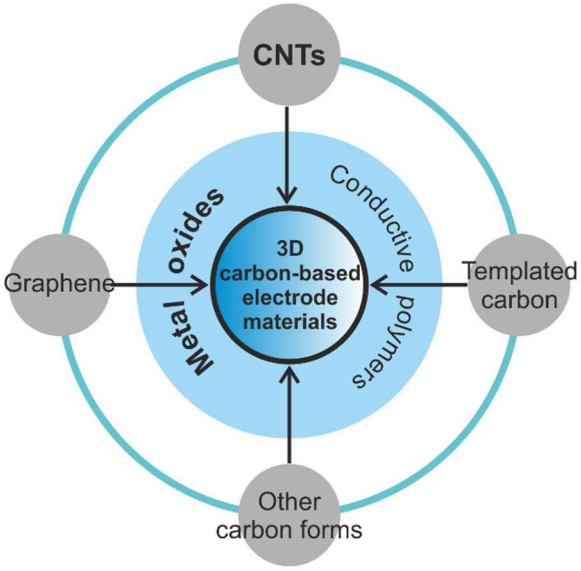

Figure 1. 3D carbon-based electrode materials from different types of carbon nanostructures and their combination with pseudocapacitive materials.

The second part deals with the main experimental techniques used in the accomplishment of this work, such as X-ray photoelectron spectroscopy (XPS), electron scanning microscopy (SEM) electron transmission microscopy (TEM) and electrochemical measurements techniques (cyclic voltammetry, galvanostatic charge/discharge and

electrochemical impedance spectroscopy). It is not the intention to give a complete and stringent description of the mentioned techniques, as they can be found well documented in the literature. Therefore, a brief description of the working principles for each technique is introduced, being outlined their key factors, in order to easily follow by the reader the work here presented and discussed. All in all, the purpose of this chapter is to provide a sense of the literature contents on the elaboration of heterostructures and their characterization, since the stat-of-the-art of the main scientific achievements is deeply reviewed in the introduction of each publication (in Chapters II, III, IV, V and VI).

I.1. Synthesis techniques of 3D-nanostructured carbon nanotubes/metal oxide hybrid materials

The growing demand for clean energy by the modern society has made essential the development of new high performance and environmentally friendly materials for energy storage and conversion. As a matter of fact, the rising levels of environmental pollution caused by the consumption of fossil energy sources are considered as the foremost challenge that mankind faces in nowadays. Therefore a renewable clean energy supply that can support the sustainable development of the global economy and society becomes mandatory. In this regard, increased energy production from the wind power and the solar implies efficient energy storage systems, needed to make the best of the electric energy generated from these renewable, intermittent sources. In addition to this, another great challenge facing current researchers is to develop new and highly efficient energy storage devices, to address the fast growing demand of electronic devices and the development of hybrid electric vehicles, as well as, the next-generation of all-electric vehicles.

In this line, new technologies for energy storage, such as nanotechnology must be sought in the development of these novel and efficient energy storage systems. Indeed, nanotechnology is an emerging interdisciplinary and comprehensive field of research that has been booming in different areas during the recent decade, including materials science, electronics and optics, medicine, environment, energy, and so on. Currently, the advance in materials science and engineering reached the point where materials can be tailored on the atomic scale to suit specific application.

Among the various energy storage systems, to meet the above requirements, chemical storage devices (batteries) and electrochemical capacitors (also called, supercapacitors) have drawn increasing attention mainly due to their excellent performance, becoming a major target of research and development. However, supercapacitors can offer several benefits when compared to batteries including high power density, short time needed for full charging, good cycling stability, excellent reversibility and environmental friendliness, since no heavy metals are used.

As a matter of fact electrochemical capacitors have been used in a variety of applications ranging from portable consumer electronics, computer memory backup systems, and hybrid electric vehicles to large scale power and energy management [1,2]. A typical example is the use of electrochemical capacitors in the emergency doors on Airbus A380 to help operate the aircraft's heavy doors. In the view of what has been mentioned above, it is reasonable to state that batteries alone are unable to provide the full solution for electric energy storage.

Electrochemical capacitors can be often distinguished into two categories, depending on the storage mechanism, as well as on the active materials used: electric double layer (EDLCs) where the capacitance arises from the pure electrostatic charges accumulated at

the electrode/electrolyte interface, such as carbon-based active electrode materials with high surface area [3,4]; and the pseudocapacitors, in which fast and reversible oxidation/reduction or Faradaic charge reactions of the electroactive species take place at or near the electrode surface, made of metal oxides [5,6] or conducting redox polymers [7,8]. The supercapacitors referred to as composite hybrids, consist in composites of carbon nanostructured materials and other nanomaterials, combining EDLC and pseudocapacitve features in hybrid electrochemical device [9].

It is generally accepted that the most important part of the supercapacitor is its electrode material. As the performance of these devices depends intimately on the properties of their components' materials, considerable attention has been paid to the research and development of the key materials. In general, the supercapacitors electrodes are fabricated from nanoscale materials that have high surface area and optimal porosity. In this way, various carbon-based materials are the most common electrode materials mainly due to their interesting properties including stability, low-cost, easy availability, nontoxic nature and environmental friendliness. In this context, activated carbons, carbon aerogels, carbon nanotubes, carbon nanofibers and graphene have been well study for EDLCs [6,10]. Obviously, each type of carbon structure has its strengths, limitations and operational conditions.

Among these examples of carbon nanostructures, carbon nanotubes, as a typical one-dimensional nanosized tubular material, have gained wide popularity as a promising electrode material for a new generation of supercapacitors [11]. Along this literature analysis, vertically aligned carbon nanotubes arrays (VACNTs) will be focused since are those studied in the present thesis.

In fact, VACNTs have been explored as materials in supercapacitors applications due to their outstanding characteristics including superior electrical and mechanical properties, high surface area, good electrochemical stability and open tubular network [11]. This open tubular network is ideally suited for loading other electrochemically active materials and favours fast ion and electron transportation. Therefore, an electrode composed from VACNTs has some merits for the capacitive performance. In Figure I.1, the conducting paths for electrolyte ions and electrons in the aligned CNTs array are schematically compared with activated carbon. The electrode composed from activated carbon (AC) particles and a binder has a large internal resistance because of both many contact points between the particles and insulating binder material (Figure I.1b). In contrast, if the CNTs are aligned on a current collector, the internal resistance is reduced because both ion and electron conductive paths are simplified as shown in Figure I1a. In addition, CNTs themselves usually have higher conductivity than AC [12].

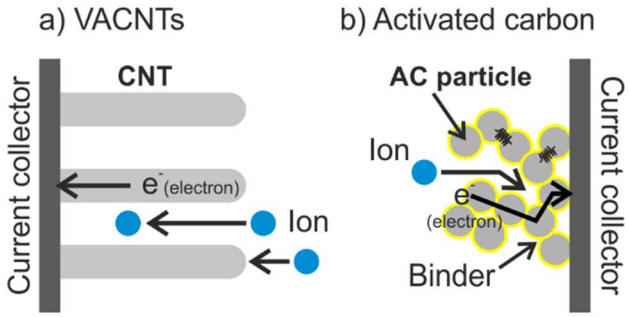

Figure I.1. Schematic representation comparing conducting paths for electron and electrolyte ion in (a) aligned carbon nanotubes (VACNTs) and (b) granular activated carbon (AC); adapted from reference [12].

In view of what has been discussed above and taking into account that bonding carbon nanotubes to the current collector is one of the major problems accompanying their application in supercapacitors, it is of great importance to have VACNTs arrays directly grown on metallic current collectors [13]. On one hand, this approach solves the problem of adhesion of nanotubes on metallic substrates and fulfills the requirement for substrate electroconductivity i.e., low contact resistance (Figure I.2). On the other hand, such a one-step method is also advantageous because it avoids laborious procedures for incorporating materials into the electrode support, consisting in mixing active materials with binding additives to form a paste or slurry, and then spread on current collector. In particular, including the use of binders may occlude the surface of the nanotubes [14]. Adding polymer binders not only increases the "dead volume" in electrode materials, but also affects the electrochemical properties.

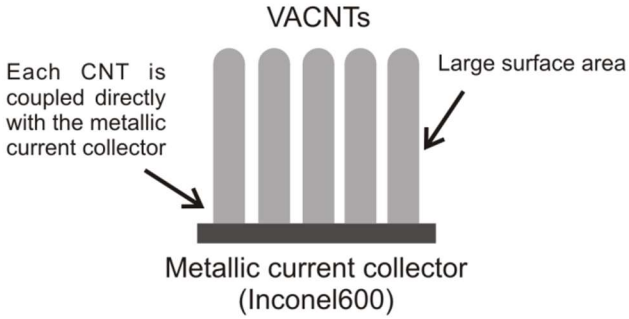

Figure I.2. Schematic illustration of a binder-free VACNTs electrode (drawing not to scale). Since each individual CNT is coupled directly with the metallic current collector, there is no need for extra binders to construct devices.

As mentioned above, the large surface area of the VACNTs framework not only permit loading of active electrode materials but also facilitates an easy access of electrolytes to the

electrode. In this way, it is expected an improvement in the overall electrochemical performance by the enlarging of electrode-electrolyte interface.

From the point of view of materials, one effective way is to combine the three dimensional (3D) VACNTs framework with pseudocapacitive materials. As a result, the nanocomposite electrode, consisting of a conductive nanotubular network coated with a pseudocapacitive metal oxide, will benefit from both mechanisms of electric double layer capacitance and pseudocapacitance.

The elaboration of these VACNTs/metal oxide heterostructures is not straightforward, especially in terms of the control over quantity, dispersion and coating degrees and homogeneity of the metal oxide coating layer. In this context, atomic layer deposition (ALD) is one of the most attractive techniques for the preparation of carbon nanomaterials-metal oxide heterostructures, due to its simplicity, reproducibility and the high conformality of the obtained films. This deposition technique is capable of controlling the decoration or the deposition of a support at atomic scale whilst preserving the supports characteristic properties [15-17]. In contrast to chemical vapor deposition (CVD), the precursors for ALD are kept separate and exposed sequentially. Ideally, each precursor forms a monolayer on the substrate, and the excess vapor is removed (purged off with an inert gas) before the next precursor is introduced. Purging by inert gas in between the reactions steps not only prevents mixing of precursors in the gas phase but, in addition removes by-products of the surface reaction and secures that there is minimum of impurities in the deposited coating. This process is then repeated until the deposited film reaches the desired thickness. This means that, the thin film thickness can be precisely determined by the number of coating cycles. Another advantage of ALD is that a layer can be deposited at lower substrate temperatures (from room temperature -RT- to 300˚C) compared to CVD. Since the adsorption of the precursor to the surface is mainly thermally driven, there exists a so-called ALD temperature window in which the ALD process takes place. The principle of ALD is schematically shown in Figure I.3. As an example, the film thin growth cycle for a binary compound (Al_2O_3) from gaseous precursors ($Al(CH_3)_3$ and H_2O) onto a substrate already bearing hydroxyl groups, is presented.

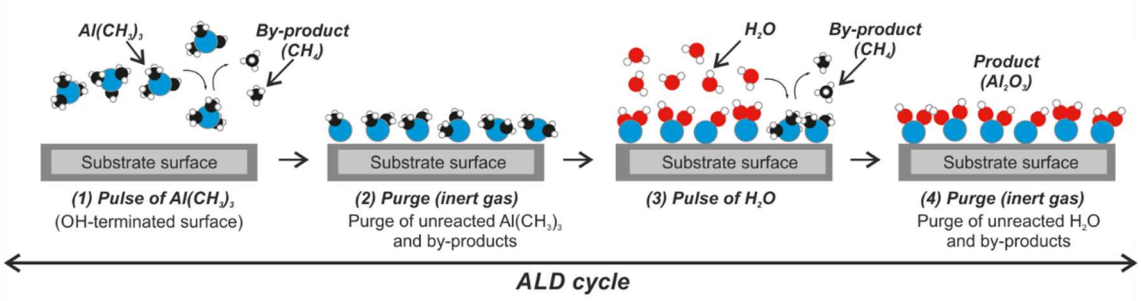

Figure I.3. Schematic demonstration of an ALD process. The precursors are introduced one at a time with a purge cycle in between. The cycle is repeated to deposit additional monolayers to achieve the targeted film thickness.

Among the described benefits of ALD, one of the most important characteristics is the excellent conformality. Since ALD is based on self-limit surface reactions of the precursors, conformality is inherent. As an example of a good conformality, a bright field transmission electron micrograph of an ALD of manganese oxide thin film in a bamboo-like commercial carbon nanotube, is shown in Figure I.4a. A darker contour is nicely seen in the inside and outside of the nanotube thus proves that the nanotube is coated with a material of larger electronic density. This is a very useful feature for many applications in nanotechnology since the basic building blocks for nanotechnology are not limited to planar type substrates [18]. As a matter of fact, ALD has been used by the microelectronics industry as the technique of choice for the production of next generation metal-insulator-metal capacitors in dynamic random access memory (DRAMs) as well as to deposit gate oxide in complementary metal-oxide-semiconductor (CMOS) transistors [19].

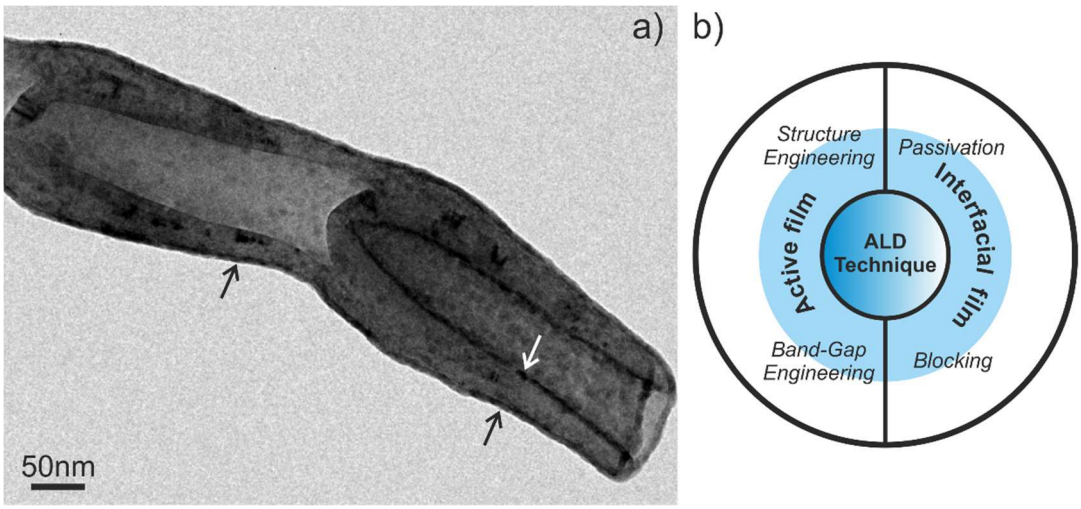

Figure I.4. BF-TEM image (a) of a bamboo-like commercial carbon nanotube coated with ALD of manganese oxide. The darker contrast observed inside (marked with white arrow) and outside (marked with black arrow) of the nanotube walls is assigned to the conformal manganese oxide coating. It is worth to mention that this nanotube was coated by the novel manganese oxide atomic layer deposition process developed under the present PhD thesis. Schematic representation (b) of the functions of ALD technique for instance in energy research field.

Owing to ALDs unprecedented capability for uniform and conformal deposition of electrochemical active materials on high surface area, high aspect ratio 3D substrates (mostly carbon nanotubes) and their hierarchical structure is widely sought to enhance material loading in supercapacitors electrodes. Therefore it is expected to lead to drastic increases in areal storage density [20]. The low temperatures characteristic of ALD processes are suitable for most current collector substrates. In contrast, CVD requires higher temperatures while sol-gel methods usually need post annealing to burn out the organic materials. Compared with physical vapor deposition (PVD), which requires high vacuum conditions, ALD can often be done in less demanding vacuum conditions, and for some processes even at atmospheric pressure [20]. It is reasonable to anticipate that ALD will be continually explored (*cf.* Figure I.4b) and subsequently expanded into new fields

that benefit from the combination of atomically precise synthesis and conformality. On the basis of advantages described above, the binder-free VACNTs electrode approach for building VACNTs/metal oxide heterostructures has great potential towards the supercapacitors electrodes fabrication. The resulting nanocomposites merge the properties of the components in such a way that new properties distinguish from those of either building block were created. In particular, the hybridization of CNTs with metal oxides creates a new class of functional materials.

VACNTs can be synthesized by various methods, but only catalytic thermal vapour deposition (TCVD) has been shown to directly grow dense aligned CNTs, ranging from μm/cm scale length, commonly called as a VACNT forest or array [21]. The alignment is caused by their high packing density, which forces the vertical growth [22]. This is directly correlated to the narrow distribution of the nanosized catalyst particles where the nanotube nucleation and growth process takes place. There is another important factor for the determination of the number of walls, that is, the diameter of catalyst particles. The number of wall of the CNTs increases with an increase in the diameter.

In this synthesis method, the decomposition of the carbon source and the CNT formation take place on the surface of previously made catalyst particles (mostly, transition metal particles, such as Fe, Ni, Co) supported on a substrate, usually a silicon (Si) wafer. Figure I.5a illustrates the “tip growth” mechanism, where the catalyst particle is lifted up during the growth [23,24]. Contrarily, as sketched in Figure I.5b, the catalyst particles remain on the substrate surface, the so-called “base growth” mechanism.

In this manner, the CNT growth process involves heating a catalytic metal at elevated temperatures in a tube furnace, using a carbon gas source through the tube reactor, over a period of time. The general mechanism in this process is the dissociation of the carbon gas source molecules, catalyzed by the transition metal, and saturation of carbon atoms in the metal nanoparticle. Precipitation of carbon from the metal particle leads to the formation of single or multiwall CNTs. When the catalyst particle becomes inactive, the CNT growth stops, this is generally due to the overcoating of the catalyst with amorphous carbon and further conversion of the metal into metal carbide. The difference of growth mode is often explained in terms of adhesion force between the catalyst and the substrate. While a strong interaction promotes the base growth mechanism, a weak contact promotes the tip growth and the CNTs diameters can be controlled by the catalyst particle size. There are different techniques to prepare active catalyst for VACNTs growth. Usually, thin metallic catalyst films are deposited using sputtering or e-beam evaporation. These deposition techniques are also employed to deposit oxide thin films e.g. alumina, which will act as a diffusion barrier or buffer layer in order to hinder the metal catalyst diffusion into the substrate, or the intermixing of the catalyst and substrate. This catalyst-assisted method involves multiple steps including preparation of the catalyst and/or supporting materials and then the growth process. In contrast, the catalyst-free or self-catalytic growth, the substrate (e.g.

metallic substrates) itself can provide catalytic active sites for the CNTs growth, without a prior ex-situ deposition of a catalyst and oxide buffer layer (Figure I.5c).

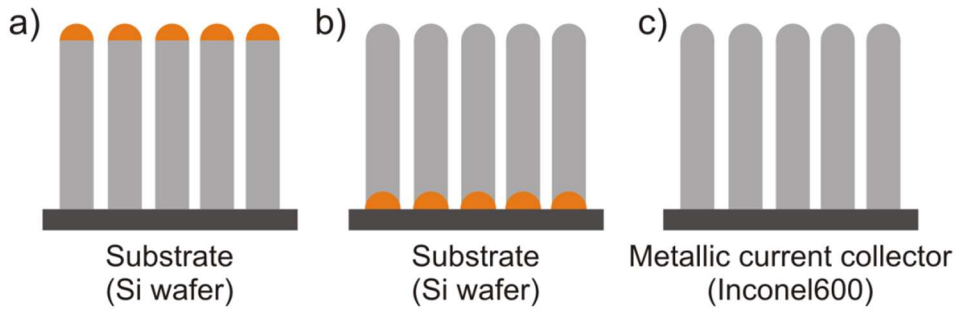

Figure I.5. Schematic illustration of VACNTs growth on two different substrates: pre-coated substrate with catalyst particles, color coded in orange (a,b) and catalyst-free substrate (c). Three growth types could be distinguished: (a) tip growth and (b,c) base growth (drawing not to scale).

For instance, Inconel®600 metallic substrate contains catalytic components for CNTs growth, meaning that there is no need to deposit catalyst and oxide buffer layers any more. In this context, the main elements of the Inconel®600 are Ni, Cr, and Fe, which can act as catalyst for the CNTs growth, especially the Ni and Fe. From a practical viewpoint, the Inconel®600 surface prior to CNTs growth is pretreated with a thermal annealing in air, changing its morphology and surface elemental composition [25]. This pretreatment process will considerably influence the growth efficiency. Therefore, it is advantageous to grow directly VACNTs on metallic substrates because they can preserve superior conductivity at the CNT-metal interfaces, without depositing any oxide buffer layer.

Zhang *et al.* have reported the use of a carbon nanotube array framework, which is directly grown on metallic substrate (Ta foil) as the support to fabricate manganese oxide-carbon nanotube array composite electrode by electrodeposition synthesis process [26]. The authors stated that the nanotubes were directly grown by e-beam evaporation on Ta foils but these substrates were coated with Al_2O_3 buffer layers (20 nm in thickness), which were used to enhance the carbon nanotube array growth efficiency. In addition to this, an external catalyst (pyrolyzing iron (II) phthalocyanine) was used to promote the nanotubes growth by CVD. In fact, this strategy follows the same procedures to those used to prepare insulating substrates, such as the growing of CNTs on the benchmark silicon substrate, highlighting also the effort needed to have CNTs arrays directly grown on metallic substrates by TCVD, without a prior ex-situ catalyst. On the other hand, the obtained manganese oxide-carbon nanotube array composite electrode presented a very good charge storage capacity. This result can be attributed to the synergetic effect between the CNTs conductive network and the pseudocapacitive property of manganese oxide. For instance, the pseudocapacitance mechanism of manganese oxide (e.g. MnO_2) in aqueous electrolyte is based mainly on two types of chemical reactions that involve the surface (i)

adsorption/desorption and (ii) intercalation/deintercalation of electrolyte cations (M^+) on MnO_2, which can be expressed as follows:

$$(MnO_2)_{surface} + M^+ + e^- \leftrightarrow (MnO_2{}^-M^+)_{surface} \quad \text{(i)}$$

$$MnO_2 + M^+ + e^- \leftrightarrow MnOOM \quad \text{(ii)}$$

where $M^+ = Na^+$ or K^+. This proposed mechanism involved a redox reaction between the III and IV oxidation states of manganese (Mn) and explain the MnO_2 charge storage behavior [27].

Nevertheless, the well-distribution of manganese oxide throughout the nanotube surface should be considered for achieving higher electrochemical performance. Particularly, the inert surface nature of as-grown nanotubes can be unfavorable for the metal oxide deposition, either as particle or as a film. In order to improve the manipulation of the CNTs, various oxidative treatments have been pursued to modify the CNTs surface by the covalent attachment of chemical groups (i.e. oxygen-containing functional groups) [28-31]. Apart from covalent functionalization, nitrogen (N) doping of the CNTs appears as an alternative and promising approach to modify their inert surface nature [32]. Nitrogen is considered the most effective foreign atom for the doping process of the CNTs in comparison with other elements such as boron or phosphorous [33,34]. Furthermore, nitrogen embedding in the surface of CNTs also leads to the formation of surface defects, resulting in significant changes in morphology, electrical conductivity, and chemical reactivity [32]. This has the advantage that these nitrogen doped CNT structures can be achieved during the TCVD growth which can be called as *"in situ"* doping, avoiding the need of additional post-growth chemical treatments. The synthesis procedures of the N-doped CNTs is similar to those used in the growth of pure aligned CNTs. However, a nitrogen source (e.g. NH_3) is added to the reaction mixture and the nitrogen content in N-doped CNTs depends on the solubility of the nitrogen in the catalyst nanoparticle at the temperature maintained during the synthesis. The grown N-doped CNTs exhibit a bamboo-like structure, which consist in a compartment region and wall, as illustrated in Figure I.6. At least, three different types of nitrogen incorporation can be found in N-doped CNTs structures: pyridinic, pyrrolic and quaternary nitrogen (Figure I.6e) [35].

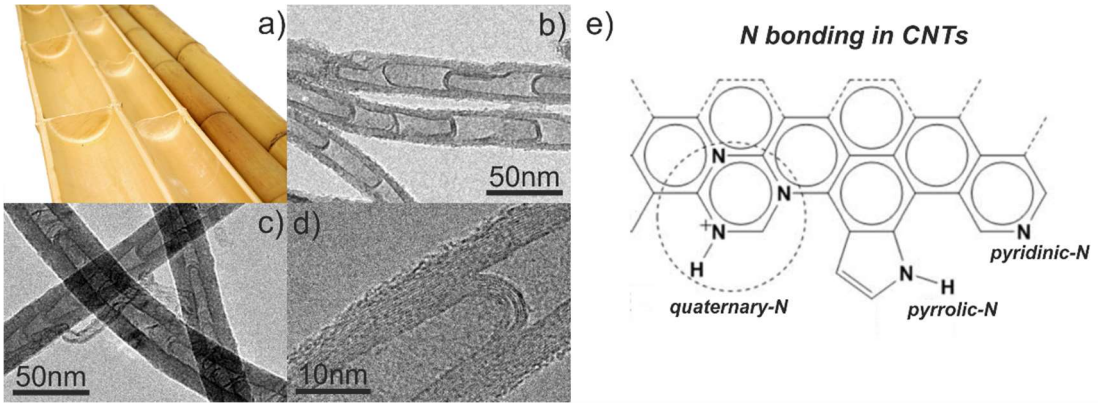

Figure I.6. Optical image of the natural bamboo structure (a) TEM images (b,c) and HRTEM image (d) of the as-prepared N-doped CNTs. It is worth to mention that these N-doped nanotubes were grown by TCVD process developed under the present PhD thesis. Schematic representation of the N bonding configurations in CNTs (e) adapted from reference [35].

Since nitrogen is more chemically reactive than the carbon atoms in the network, its presence can be exploited as possible anchoring and nucleation points during the metal oxides deposition, making them ideally suited as a support for a second material that can be deposited onto their surface either as particle or as a film. For example, the ALD precursor needs to react with the initial surface species on the very first ALD cycle. As consequence, the coverage and uniformity of ALD deposited thin films strongly depend on the surface chemistry of the substrate. A lack of uniform and dense nucleation sites would produce a non- or incomplete coating, which can be explained by the poor interfacial interaction between the nanotubes and the metal oxide precursors. It is worthy to mention that one of the foremost challenges in nanotechnology fabrication is reaching atomic control in thin films growth, to achieve controlled thickness and conformal deposition of a support at the nanoscale. Moreover, this has to be achieved while preserving the supports characteristic properties. All in all, the tailoring of surface functionalization nature can be used to control ALD film growth and it has been used to elaborate various metal oxide/carbon nanotubes heterostructures, for applications in different fields [36].

Finally, the one-step electrode preparation strategy for binder-free hybrid capacitors, the aim of this PhD thesis, is briefly presented. As above described, it is based on the 3D-nanostructured VACNTs/metal oxide hybrid arrays.

As a result, a nanocomposite electrode formed by a 3D-array of VACNTs, supported on conductive Inconel®600 substrate, coated with metal oxide is obtained (Figure I.7a). For comparison, Figure I.7b provides a generic schematic illustration for the electrode preparation procedures from vertically aligned carbon nanotubes on the benchmark silicon (Si) substrate, which was pre-coated with a thin film of catalyst, prior to the CVD growth process.

In this case, the VACNTs are covered with a Pt mesh (current collector) and a conductive additive film to preserve the vertical alignment and to form a strong contact. Afterwards, the Si substrate is removed with KOH. In contrast, herein proposed one-step electrode preparation strategy avoids all these laborious and complicated processes and simplifies the electrode fabrication process.

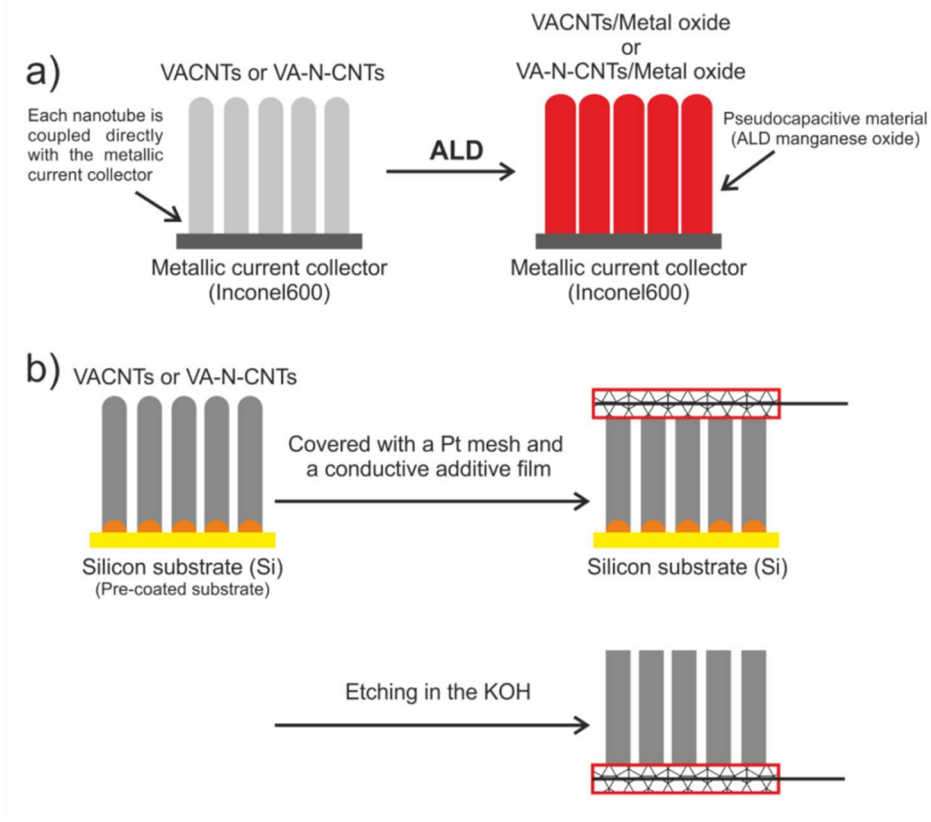

Figure I.7. (a) Conceptual illustration of 3D vertically aligned carbon nanotube/manganese oxide nanocomposite electrode for binder-free electrochemical (hybrid) capacitors. (b) Schematic illustration for the electrode preparation procedures from vertically aligned carbon nanotube array on silicon substrate .This last procedure was inserted for comparison purpose (drawings not to scale).

I.2. Characterization techniques

I.2.1. Supercapacitors performance characterization

Up to now, the principles underlying supercapacitor electrode materials selection and strategies to engineer these materials were presented. In continuation, testing techniques to evaluate supercapacitors performance including instruments and measurements of key metrics will be further introduced.

Typically, an electrochemical double layer capacitor (EDLC) or supercapacitor consists of two electrodes immersed in an electrolyte solution, with a voltage potential across the current collector. A dielectric separator between the two electrodes prevents charge propagation between the electrodes, as illustrated in Figure I.8. The specific capacitance and charge storage of a supercapacitor intimately depend on the electrode materials used. Therefore, the material composition of a supercapacitor has mainly two requirements: (i) it must be sufficiently electrical conductive to transport charge carriers to the interface with the electrolyte and (ii) it must be electrochemically stable [37]. A material which is reactive with the electrolyte would be unsuitable for long term electrochemical cycling. Additionally, the electrode material must also have high surface area, since it was thought as the primary requirement to have high capacitance. The capacitance of EDLCs is proportional to the effective surface area of electrode and is inversely proportional to the thickness of electric double layer (EDL). In this context, activated carbons with a large surface area have been employed as electrode materials being currently the main components of commercial supercapacitors [37].

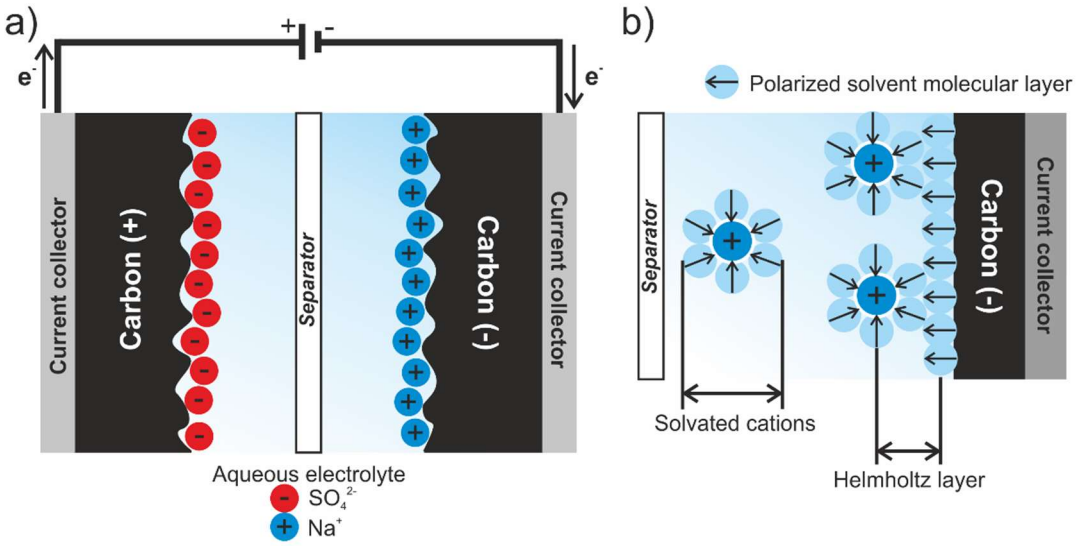

Figure I.8. Scheme view (a) of an electricochemical double layer capacitor (EDLC), with two layers of capacitive storage. The negative plate attracts positive ions and the positive plate atrracts the negative ions in the electrolyte. EDLC illustration of Helmholtz layer (b).

Besides the electrodes, other necessary component of a supercapacitor is the electrolyte. The electrolyte must meet the criteria of electrochemical stability and ionic conductivity as well as low toxicity. Aqueous, non-aqueous or solid state, are the three classes arising on the basis of the electrolyte system. One primary difference between electrolytes performance is the electrolyte potential stability window. In this way, aqueous salt solutions electrolytes have a limited stability window of ~1 V, whereas non-aqueous electrolytes, including organic and ionic liquids, have shown stability window of 2 and 3.4 V, respectively [38]. Additionally, the affinity of the electrolyte for the electrode active material must also be considered, as well as, the sizes of cation and anion of the electrolyte. In fact, a good electrolyte wetting of the full electrode surface is necessary for double-layer formation. While liquid electrolytes are most commonly applied for macroscale supercapacitor applications, the solid state electrolytes are particularly interesting for microscale and flexile applications. For example, an aqueous electrolyte/polymer gel such as hydroquinone/H_2SO_4/poly(vinyl alcohol) is commonly used as a solid state electrolyte where redox electrochemical active compounds were combined with the polymer gel electrolyte [39]. It is worth to note that aqueous electrolytes solutions must be de-aerated before electrochemical measurements to eliminate dissolved oxygen.

Before presenting a detailed discussion of the electrochemical characterization techniques, distinction between two and three electrode measurements should be done. Normally, the two electrode system is typically used to characterize fully fabricated devices or prototypes, while the three electrode system is advantageous for examining the fundamental electrochemical properties of the electrode material system [13,40]. For fundamental studies on the single electrode, conventional three electrode configuration cell can be used, as illustrated in Figure I.9. The characterization of the electrode material is evaluated by doing measurements against counter and reference electrodes. Typically, platinum (Pt) is used as counter electrode which supplies the necessary current during measurement. On the other hand, the reference electrode consists in a material with a well-known redox potential, e.g. the saturated calomel electrode, which is composed of the mercury(I)/mercury chlorine (Hg/Hg_2Cl_2) redox pair or silver/silver chlorine (Ag/AgCl) electrode. This reference electrode is used to accurately measure the potential at the working electrode to a known reference. The working electrode material is the key component that determines the electrochemical performance of the supercapacitor. In general practice, the working electrode material powders are mixed with some binding additives to form a paste, and then coated on current collector mesh or foil. Normally, the electrode thickness is a few micrometers to sub-millimeters size, depending on the active materials. The mass of active materials in the electrode must be known and preferably the electrode volume should be measured. In summary, the three electrode configuration cell is valuable for determining electrochemical specific material characteristics, allowing the accurately determination of the specific capacitance of the supercapacitors materials.

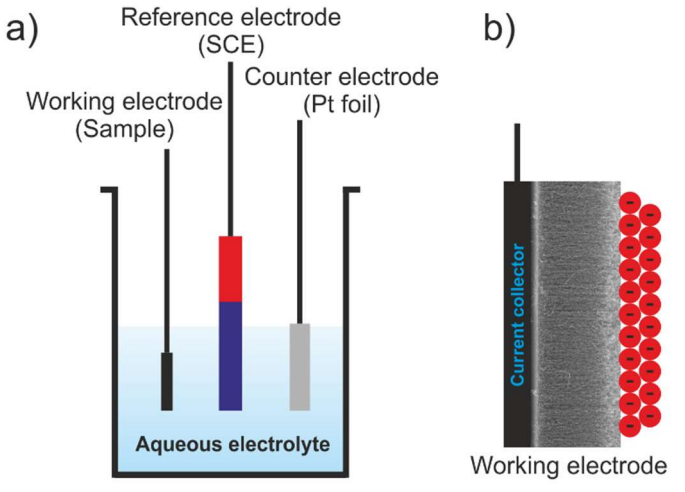

Figure I.9. Schematic illustration of: (a) three electrode configuration measuring cell (beaker type cell) and (b) half-cell system for three electrode measurements (sample in a).

In the case of three-electrode configuration cell, the electrode performance is commonly evaluated by cyclic voltammetry (CV), galvanostatic charge-discharge (GCD) and electrochemical impedance spectroscopy (EIS). In essence, all these test techniques can be used to measure the three fundamental parameters: voltage, current, and time. Other metrics, including the specific capacitance, operating voltage, equivalent series resistance, the time constant, energy and power performance of supercapacitors, can be derived from them [40].

For a three-electrode cell, the voltage potential applied to the working electrode is the one shown on the X-axis of the cyclic voltammogram (CV) chart (and on the Y-axis of the constant current diagram) and is based on the particular reference electrode used. The speed of the potential change in mV s^{-1} is designated as scan rate or sweep rate (ν), and the range of potential change is called the potential window or operation potential. When the capacitance is simply originated from the EDL, CV curve is characterized by its classic rectangular shape. However, the CV curve is not always rectangular, this is marked if the pseudocapacitance is added and with increasing resistance the CV curves also become distorted and even asymmetric [12]. CV is useful as a quick screening procedure to identify potential capacitor materials and CV testing is also suitable in practice to determining the potential window. In addition, the specific capacitance of the supercapacitors materials can be obtained by integration the CV curves. Therefore, in three electrode configuration, the specific capacitance (C_{sp}) of the electrode materials can be calculated using the following equation (1) [37]:

$$C_{sp} = \frac{\int I(E)dE}{2v(E_2 - E_1)A} \qquad \text{Equation (1)}$$

where C_{sp} is the specific capacitance in (F g^{-1}), $I(E)$ is the instantaneous current in A, v is the scan rate in V s^{-1} and $(E_2\text{-}E_1)$ is the potential range in V and A is the electrode area in

cm^2. For supercapacitors, where the mass or volume are too small, and the footprint area (cm^2) of one electrode is used instead; their specific capacitance must be normalized by this footprint area (mF cm^{-2}).

Galvanostatic charge-discharge (GCD) technique involves repetitive charging and discharging of the working electrode at a constant current level. The potential is monitored as a function of the time and normally a plot of the potential vs. time (s) is the output. If a step change in current is visible in this plot, it means that, an instantaneous voltage drop when switching from charging to discharging occurred. This voltage drop is often known as the IR drop, which arises from the ohmic resistances in the system. These resistances result from the combination of electrode/electrolyte resistance and contact resistances [37,40]. GCD can also be conveniently used to study the cycling stability of the supercapacitor to probe the lifetime cyclability of the electrode material. Moreover, by using a three-electrode cell, the specific capacitance can also be calculated according to the following equation (2) [37]:

$$C_{sp} = \frac{I\Delta t}{\Delta E A} \qquad \text{Equation (2)}$$

where I refers to discharge current in A, Δt represents the discharge time in s and ΔE is the potential range in V and A is the electrode area in cm^2. Similar to CV, when other factors than EDL contribute to the capacitance, GCD curves deviates from the linear relationship.

Electrochemical impedance spectroscopy (EIS) measures the impedance of a power cell as a function of a wide range of frequency (from 1 mHz to 1MHz), by applying a low amplitude alternative voltage (usually 5 mV or 10 mV) superimposed on a steady state potential. It is a technique used to measure and analyze the resistance at various interfaces such as electrode/electrolyte and contact resistance. The resulting data are usually expressed graphically in a Bode plot, to demonstrate the cell response between the phase angle and frequency, and in a Nyquist plot, to show the imaginary and real parts of the cell impedances on a complex plane. The charge transfer resistance is given from the diameter of a semicircle in a Nyquist plot. However, numerical values of the resistance by Nyquist plot are not precise because perfect semicircles are not usually obtained. For example, the Nyquist plot for a typical supercapacitor would resemble to vertical line along the imaginary axis in the low frequency region. The equivalent series of the electrode can also be obtained from the intersection of the Nyquist plot at x-axis.

Besides lifetime cycling performance, power density and energy density are also performance metrics for evaluating supercapacitors. These two metrics are mostly directly relevant to the end applications. They normally are evaluated in gravimetrically or volumetrically in W kg^{-1} or W L^{-1} for power density, to describe the efficiency in energy uptake/delivery; and in Wh kg^{-1} or Wh L^{-1} for energy density to demonstrate the amount of electrical energy stored or deliverable [39]. The energy density (E) can be calculated by use equation (3):

$$E = \frac{1}{2}CV^2\left(\frac{1}{3600}\right)$$ Equation (3)

where C is the specific capacitance in F cm^{-2} obtained from CV or galvanostatic discharge, and V is the maximum accessible potential window in V. The power density is given by equation (4):

$$P = \frac{E}{\Delta t}$$ Equation (4)

where Δt represents the discharge time obtained from GCD. However, the estimation of the energy density and power density for the whole device is frequently impracticable. This is mainly due to the fact that, for in frequent cases where the focus is to probe for novel materials, distant types of current collectors, new cell designs and the final products may not be in the form of well packaged cell. In summary, for supercapacitors materials analysis and prospect, all three techniques described above can be employed with different emphases in three electrode configuration cell.

As discussed above, depending on the electrode materials, two types of energy storage can occur in supercapacitors. The first, as in, electric double layer capacitors e.g. carbon based materials store charges electrostatically via physisorption of the electrolyte ions. The second, as the case of pseudocapacitive materials e.g. metal oxide or conductive polymers, involves a fast surface redox reaction. On the other hand, supercapacitors based on hybrid electrode materials which combine these two charge storage mechanisms, resulting in improved device characteristics.

Therefore, it is of great importance to investigate the morphology and surface chemistry of the electrode materials, which directly influence the ultimate performance and/or efficiencies of supercapacitors. In the particular case of the present thesis, the electrodes consist of coated vertically aligned carbon nanotubes with metal oxide (e.g. manganese oxide) via atomic layer deposition. The characterization of this type of heterostructures is very important, especially the interconnection between the two different materials and their nanostructure in terms of morphology, size and shape.

I.2.2. Scanning electron microscopy (SEM)

The morphology of the obtained vertically aligned carbon nanotubes/metal oxide heterostructures can be revealed by scanning electron microscopy (SEM) images, recorded using secondary electron (SE) and backscattering electron (BSE) detectors. The image recorded with SE will show the structural details of the coating, while BSE images, will show the distribution and location of the higher atomic number material (e.g. manganese) on the surface of the nanotubes. An additional electron interaction of major importance in the SEM occurs when the primary electron collides with specimen and ejects a core electron from an atom in the solid. The excited atom will decay to its ground state by emitting either characteristic X-ray photon or an Auger electron. The X-ray emission signal can be sorted by energy dispersive X-ray detector. These distributions are characteristics of the element that produced them and the SEM can use these signals to produce elemental images that show the spatial distribution of particular elements in the field of view. Energy dispersive X-ray spectroscopy (EDS) can be used for chemical analysis, using the elemental mapping or elemental line scan profile, which will reveal the distribution of the metal and the oxygen over the coated nanotubes. In fact, elemental mapping recorded in the SEM allow a fast screening of the homogeneity and elemental composition of the film. Although, due to the limited spatial resolution of EDS performed in the SEM, it is insufficient to evaluate the homogeneity at nanoscale. This means that a large volume of sample will produce X-ray emission for any position of the smaller primary beam, and consequently the spatial resolution of this type of image will rarely be better than 0.5 μm [41]. Nevertheless, the EDS elemental mapping will be sufficient to confirm the interpretation of the contrast variation of the BSE SEM images. Briefly, the main components of SEM are electron column, scanning system, detector(s), image display and recording, vacuum system and electronics, as illustrated in Figure I.10. The electron column of the SEM consists of an electron gun and two or more electromagnetic lenses operating in vacuum. The electron gun generates electrons and accelerates them to energies ranging from 1 to 30 keV. The main purpose of the electromagnetic lenses and apertures is to create a small, focused electron probe on the specimen. These microscopes can generate an electron beam at the specimen surface with spot size less than 10 nm in diameter, while still carrying enough current to form acceptable image. As the beam interacts with the specimen it creates various signals (such as secondary and backscattered electrons, characteristic X-ray and so on), all can be appropriately detected. All these signals are the product of strong electron-specimen interactions, which depends on the energy of the incident electrons and the nature of the specimen. The resolution of SEM images at high magnifications is primarily determined by the size of the incident electron probe, the stability of the microscope and the specimen, and the inherent properties of the signal-generation processes.

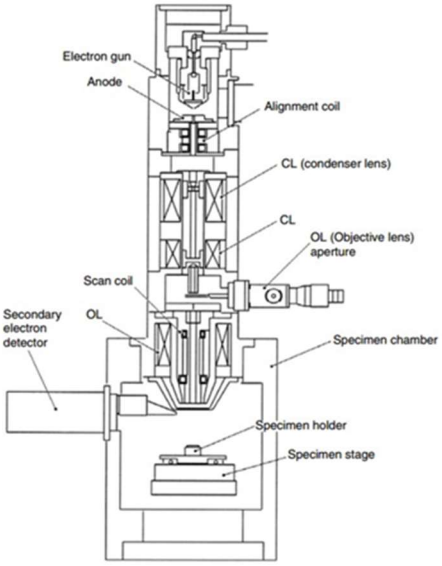

Figure I.10. Schematic diagram of a SEM instrument. The specimen stage, electron beam scanning coils, signal detection, and processing system provide real-time observation and image recording of the specimen surface.

I.2.3. Transmission electron microscopy (TEM)

In addition to the SEM studies, the transmission electron microscopy (TEM) investigations will be essential to assess the performance of ALD deposition, i.e., if the metal oxide will lead to a homogeneous coating of the outer and inner walls of the nanotubes as well as the interface between the materials. High resolution TEM (HRTEM) and electron diffraction (selected area electron diffraction, SAED) experiments will reveal the crystallinity of the as-deposited metal oxide film.

TEM has become a successful characterization technique in materials science. TEM's strong card are its high lateral spatial resolution and its capability to provide both image and diffraction information from a single sample. Indeed TEM can achieve atomic scale lateral resolution, but no depth information is obtained because the technique works by having the probe electron beam transmitted through a sample that is up to 200 nm thick. However, sample preparation in TEM is critical, since the sample sizes accepted are usually less than 3 mm in diameter and 200 nm in thickness (so that the electron beam can pass through the sample). In addition, the highly energetic beam of electrons used in TEM, interacts with sample matter to produce characteristic radiation and particles (Figure I.11). These signals often are measured to provide materials characterization using energy dispersive X-ray spectroscopy (EDS), electron energy loss spectroscopy (EELS), secondary and backscattered electron imaging, just to mention a few possible techniques [41].

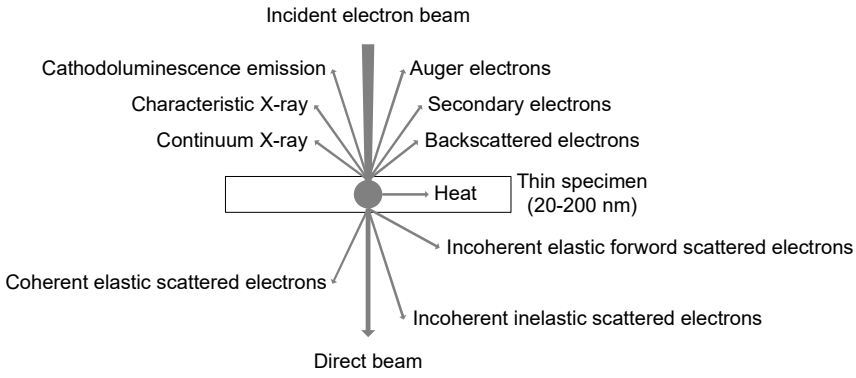

Figure I.11. Signals generated when an energy beam of electrons interacts with a thin specimen. Most of these signals are used in analytical electron microscopy.

The TEM instrument is characterized by three main components: the illumination system, objective lens/stage, and imaging system. The illumination system comprises the gun and the condenser lenses, and its role is to take the electrons from the source and transfer them to the thin sample. The objective lenses and the sample holder/stage is the heart of the TEM. Here is where all of the beam sample/specimen interactions take place as well as the two fundamental TEM operations occur, namely, the creation of the various images and diffraction patterns (DP) that are subsequently magnified for viewing and recording. The imaging system uses a several lenses to magnify the image or the DP produced by objective lens and to focus on the viewing screen or computer display via a detector, CCD, or TV camera [42]. Figure I.12 reveals a schematic diagram of a TEM instrument, showing the location of a thin sample and principal lenses and apertures within a TEM column.

The illumination system can be operated in parallel beam or in convergent beam mode. The parallel beam mode is used primarily for selected area diffraction, SAED and TEM imaging. In diffraction mode, an electron DP is originated from the sample are illuminated by the electron beam, the DP is equivalent to an X-ray DP: a single crystal will produce a spot pattern, a polycrystal will produce a ring pattern and a glass or amorphous will produce a series of diffuse halos.

In image mode produces an image of the illuminated sample area and this image can contain contrast brought about by mainly two mechanisms: mass thickness contrast and diffraction contrast. The contrast in the images is obtained either by selecting specific electrons or excluding them from the imaging system. The images can be formed either bright field (BF) or dark field (DF) images by selecting the direct or scattered electrons, respectively. The direct or a scattered electron beam is selected with the objective aperture.

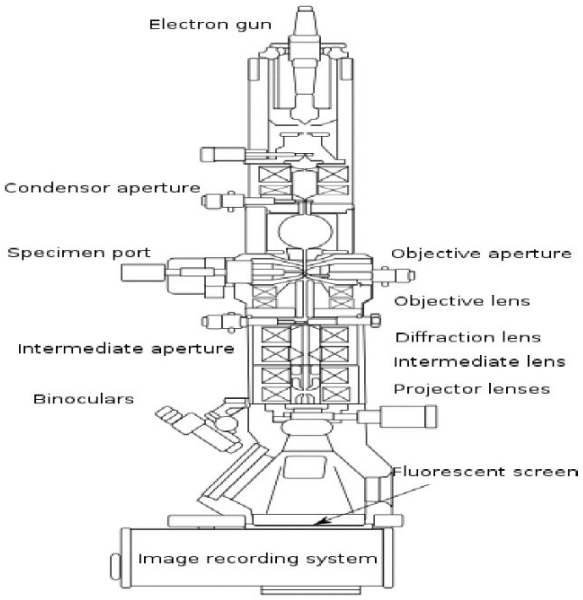

Figure I.12. Schematic diagram of a TEM instrument. This scheme shows the location of a thin sample and principal lenses and apertures within a TEM column.

Another example of imaging techniques in TEM is high resolution transmission electron microscopy (HRTEM). HRTEM is made possible by using a large diameter objective aperture that admits not only the transmitted beam, but at least one diffracted beam as well. Selecting several beams allows a structure image to be formed. The many lattice fringes intersect and give a pattern of dark (or bright) spots corresponding to atom columns. In fact these fringes represent direct resolution of the Bragg diffracting planes; the contrast is referred as phase contrast. Additionally, HRTEM images are capable of providing the information about local atomic structures, which are most useful for identifying individual defects in crystals and studying the atomic arrangements at interfaces between heterostructures.

The second illumination mode is the convergent beam mode. It is used mainly for scanning (STEM) imaging, analysis via X-ray and electron spectroscopy and convergent beam electron diffraction (CBED).

In a STEM the direct or scattered beams are selected in an equivalent way but use detectors rather than apertures. The insertion of BF on axis detector will gather the direct beam (Figure I.13a) on the other hand the insertion of an annular DF (ADF) (Figure I.13b) will gather the scattered beam. In summary, BF and DF images can be formed with direct or scarred beam, respectively.

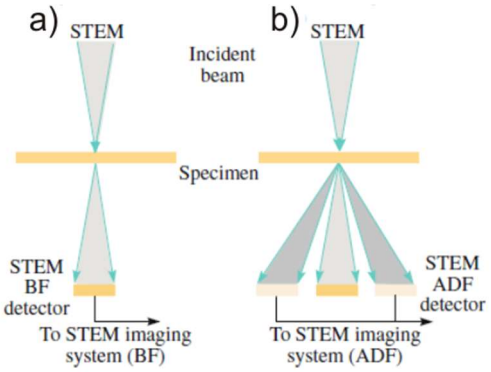

Figure I.13. Selection of the beam in STEM: (a) direct beam, (b) BF on axis detector and scattered beam. Annular dark field (ADF) detector, adapted from reference [42].

STEM has the advantage of being able to efficiently collect electrons that are scattered through large angles, using high angular annular dark field (HAADF) detector, as shown in Figure I.14.

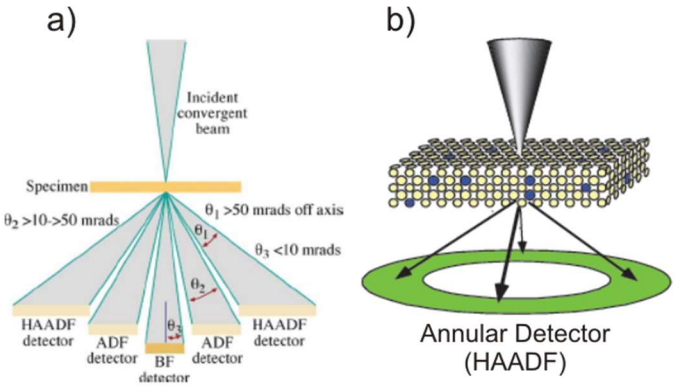

Figure I.14. Schematic of the HAADF detector setup for Z-contrast imaging in a STEM. (a) Conventional ADF and BF detectors and (b) HAADF detector, that gathers electrons scattered through $\theta_1 > 50$ mrads, adapted from reference [42].

HAADF imaging is also known as Z-contrast imaging where heavy atoms having large, positively charged nuclei, scatter electrons more effectively and to higher angles of deflection (Figure I.14b), that do light atoms. In this context, HAADF imaging in STEM will show show the distribution and location of the higher atomic number material (i.e. metal component) on the outer and inner walls of the nanotube, as the contrast will be selected such that the metal oxide (Z-contrast) coating will be seen while the carbon support remains nearly invisible.

Finally, an example of coated nanotubes with ALD of manganese oxide is given, in Figure I.15a. On one hand, the uniformity of the coating along the whole surface of the nanotubes is revealed by darker contrast regions in the BF-TEM image (Figure I.15a). On the other hand, the morphology of the obtained heterostructures is nicely shown by SEM images recorded using the secondary (SE) or backscattered electron (BSE) detector, respectively (Figure I.15b,c). The SE image provide structural details of the coating while the BSE image offers further information about the distribution of the manganese (brighter contrast) on the nanotube.

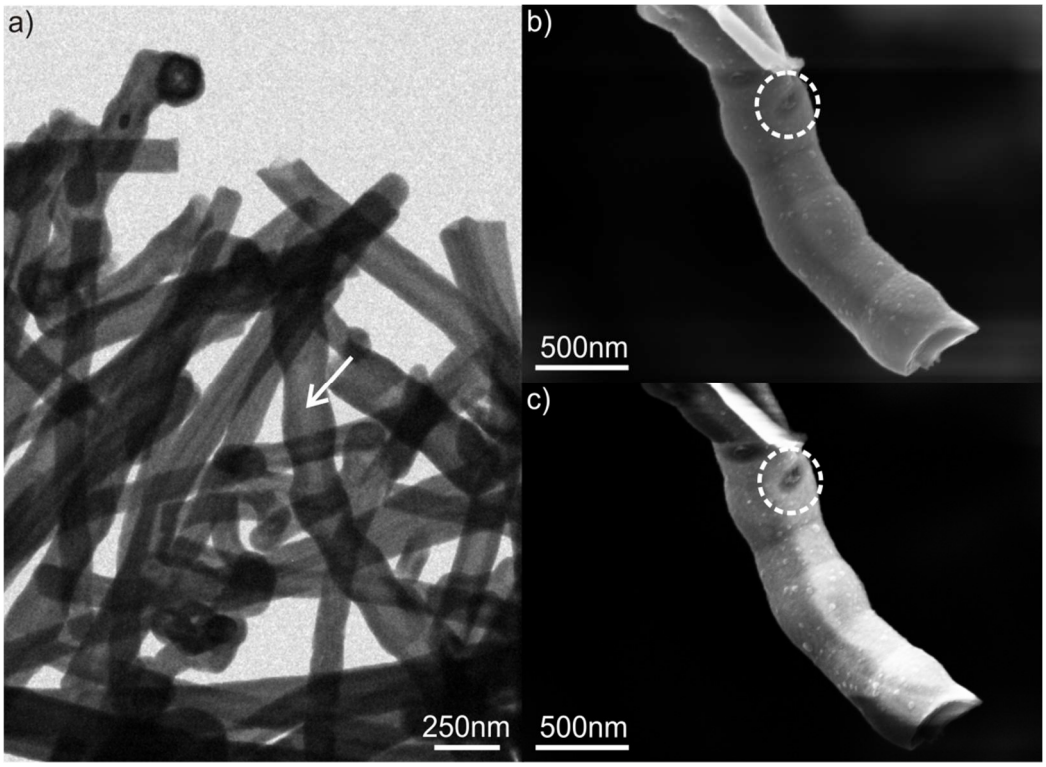

Figure I.15. Overview BF-TEM image (a) and SEM image using secondary electrons (b) and backscattered electrons (c) acquired at low acceleration voltage (5 keV) of commercial carbon nanotubes coated with ALD of manganese oxide. The coated bamboo-like commercial carbon nanotube labeled with a white arrow in (a) is shown in (b,c). In order to highlight the manganese oxide deposition film, defective regions in the coating are indicated by dashed circle (b,c) It is worth to mention that these nanotubes were coated by the novel manganese oxide atomic layer deposition process developed under the present PhD thesis.

I.2.4. X-ray photoelectron spectroscopy (XPS)

The electron microscopy characterization techniques should and will play an important role in understanding the nature of nanosystems. As a matter of fact, electron microscopy and the associated analytical techniques can provide information on the physical-chemical properties of individual nanocomponents, as well as, the spatial relationships among these nanocomponents. In line with these characterization techniques of nanosytems, the X-ray photoelectron spectroscopy also provides a means of elemental identification which can also be quantified via measurement of integrated photoelectron peak intensities and the use of a standard set of sensitivity factors to give a surface atomic composition.

X-ray photoelectron spectroscopy (XPS) is an invaluable tool for the characterization of valence states and the associated chemical structure of thin films, and this information can be correlated directly with the functional property of the film. Consequently, this surface characterization technique is relevant in the evaluation of the results presented in this thesis, namely, in the determination of surface electronic states of nanostructured carbon based electrode materials. Hence, this technique helps to explain the obtained electrochemical results, particularly, the oxidation states of the pseudocapacitive metal oxides. Moreover, the XPS technique can also be used to probe the elemental composition of the carbon nanotubes, for example the nitrogen species in the graphitic network of the nitrogen doped CNTs. These data would lead certainly to an establishment of a correlation between the doping agent concentrations on the nitrogen content. Due to that, a brief explanation of this technique is following presented.

All materials and structures interact with their environment through surfaces. Consequently, the importance of surface as opposed to bulk analysis is increasingly recognized in the design and development of advanced materials. Electron emission spectroscopy, such as, X-ray photoelectron spectroscopy (XPS) has the capability for microanalysis of the few atom layers of solid sample [43]. This technique is broadly used for chemical surface characterization, which leads to a surface definition. For that, it is necessary to distinguish the following terms: surface in general, physical surface and experimental surface. Surface in general, is the “outer portion” of a sample of undefined depth. Physical surface is the outermost atomic layer of the sample. Experimental surface is that portion of the sample with which there is significant interaction with particles or radiation used for excitation. It is the volume of sample required for analysis, or the volume corresponding to the escape of the emitted radiation of particles, whichever is larger [44].

In XPS, the energy carried by an incoming X-ray photon is absorbed by the target atom, raising it into an excited state from which it relaxes by the emission of a photoelectron with kinetic energy equal to the difference between the incident X-ray energy, the binding energy of the level concerned, and the work function. Electrons are emitted from all energy

levels of the target atom, and, hence, the electron energy spectrum is characteristic of the emitting atom type and may be thought of as its XPS fingerprint. Lines in the spectrum are labeled according to the energy level from which they originated [43].

The XPS chemical shift is probably the most important feature of the technique. The chemical shift is referred to small changes in electron energy that are the results of the chemical environment of the emitting atom. The origin of the chemical shift is attributed to the charge of the atom prior to photoemission. It plays a major role in the determination of the magnitude of the chemical shift. As general rule, more the emitting atom forms bonds with electronegative species; greater is the positive XPS chemical shift. A schematic representation of a XPS spectrometer is shown in Figure I.16. This is an accurate ultra-high vacuum characterization technique, in which photoelectrons are first generated by bombarding a material with X-rays, and then, energy analyzed to yield information about elemental composition and in some cases local chemical bonding.

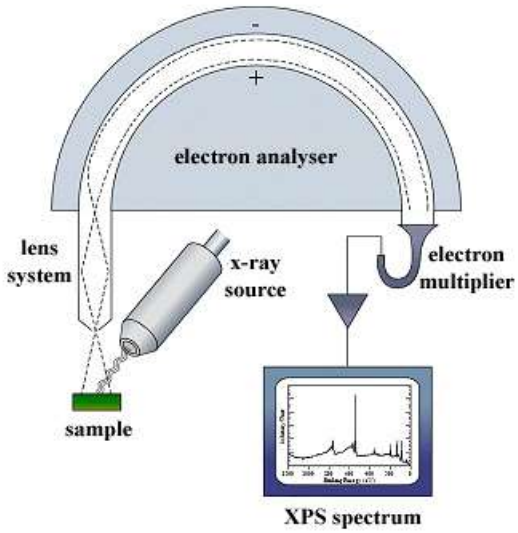

Figure I.16. Illustration of typical electron spectrometer showing the necessary components.

The photoelectrons generated in XPS that arrive at the electron detector are predominantly emitted from atoms residing within the top ~2.5 nm of a material. The X-ray source is usually an Al- or Mg-coated anode, struck by electrons from high voltage Alk_{α} or Mgk_{α} radiation lines, produced at energies of 1486.6 eV and 1256.6 eV, with line widths of about 1 eV. The X-rays flood a large area (~1 cm^2) and the beam's spot size can be improved to about 100 µm in diameter, by focusing the electron beam onto the anode and passing the X-rays through an X-ray monochromator [41,43,44].

The critical point of the surface analysis is to prevent any changes to the surface before or during the experiment. Due to that, most methods do not allow one to carry out the technique *in situ*, as ultra-high vacuum (UHV) is needed for several reasons: (i) to have

sufficient mean free path of the probe and detected particles (electron, ions, atoms) and (ii) to eliminate the signal from the interaction of the probe particle with the molecules in gas phase. It is worth pointing out that UHV is required also to preserve a reproducibly clean surface during all measurements; this means that for maintenance of a clean surface pressures lower than 10^{-9} are needed. Another problem is connected with sputtering and heating the surface. Surfaces in UHV are initially covered normally with a several layers of oxide and adsorbed hydrocarbons, due to prior exposure to the atmosphere, that need to be cleaned away by argon bombardment to permit analysis of the sample by a surface sensitive technique. This process of sputter cleaning can change the surface composition and/or structure and is not always successful at removing all contamination [43].

I.3. Atomic layer deposition (ALD), thermal chemical vapor deposition (TCVD) and physical vapor deposition (PVD) tools

The carbon nanotubes/metal oxides heterostructures presented in this thesis have been achieved through the use of different vapor phase deposition techniques. The catalyst-supported CVD approach is realized in a TCVD reactor and the catalyst preparation was carried out in a PVD reactor (magnetron sputtering). Two different ALD reactors were used in order to develop metal oxides depositions on the carbon nanotubes. One of those is a cross flow home-made ALD reactor working in continuous mode. This set-up was rebuilt with the purpose of depositing zinc oxide. The other, operating in exposure mode, was used for the manganese oxide deposition, as explain as follows.

The ALD process can be distinguished into two main types: (i) exposure mode reactor and (ii) continuous flow reactor. In the first type, the precursors are transported through stainless steel tubing into the reaction chamber by an inert gas (N_2 or Ar), where a saturated precursor layer is deposited on the surface and excess chemicals are purged away into the vacuum pump. On the vacuum line, there is at least one additional valve (stop valve) to isolate the reaction chamber from the vacuum pump. This stop valve is used for an alternate mode of ALD referred to as “exposure mode”. In this working mode, the stop valve is closed before pulsing the precursors, effectively isolating the vacuum chamber. Then the precursor is pulsed into the reaction chamber, and allowed to remain several seconds to ensure saturation of the entire surface before opening the stop valve and subsequently purging the reaction chamber.

On the other hand, the continuous flow reactor type consist in a continuous flow of inert carrier gas (N_2 or Ar) which is used for precursor transportation and purging through the reaction chamber to the vacuum pump. In this way, the reaction chamber is never isolated from the vacuum pump i.e. the stop valve between the reaction chamber and vacuum pump is removed.

The main components of the ALD system include the reaction chamber (stainless steel), vacuum pump (dry scroll pump or two stages oil sealed rotary vane pump equipped with a trap), pressure gauge, stainless steel tubing and hoses for gas transport, and a range of manual and pneumatic valves for control of gas flow in and out of the chamber. The ALD precursors, normally, are contained in stainless steel cylinders (canisters) that are enclosed by a manual valve for transfer of reactive chemicals in air. An optical image of the cross flow home-made ALD reactor used in this presented thesis is shown in Figure I.17.

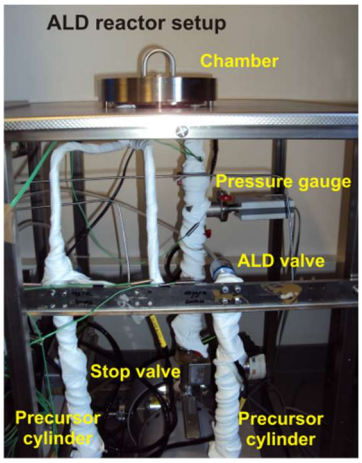

Figure I.17. Optical image of the cross flow home-made ALD reactor. All the gas lines and valves are wrapped with heaping tape to prevent precursor condensation. The heaping tapes are isolated with white teflon tape.

The manganese oxide deposition development was realized at the Institut für Chemie, Humboldt-Universität zu Berlin in a commercial ALD reactor, an ARRADIANCE GEMStar-6 (Benchtop Thermal ALD system) operated in exposure mode, equipped with BMT803N ozone delivery system.

The carbon nanotubes arrays growth was carried out in a thermal CVD reactor. The reactor consists of a 5 cm inner diameter quartz tube housed inside a furnace, equipped with mass flows for the reaction gases, electro and manual valves, two stages oil sealed rotary vane pump, as revealed in Figure I.18. For automatic operation, the TCVD reactor is also equipped with a PC control station.

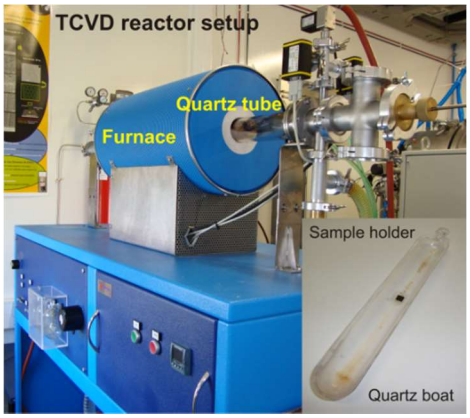

Figure I.18. Optical image of the home-made TCVD reactor setup. The inset shows the sample holder i.e., quartz boat where the substrates were placed.

The multilayer catalyst preparation (Al_2O_3 buffer layer/Fe catalyst film) was undertaken in a PVD (magnetron sputtering) reactor. Figure I.19 shows the PVD reactor setup, equipped with a RF and a DC power supply allowing the deposition of ceramics and metal films, respectively. A brief description is given as below. In the basic sputtering process, a target (or cathode) plate is bombarded by energetic ions generated in a glow discharge plasma, situated in front of the target. The bombardment process causes the removal, i.e., "sputtering", of target atoms, which may then condense on a substrate as a thin film.

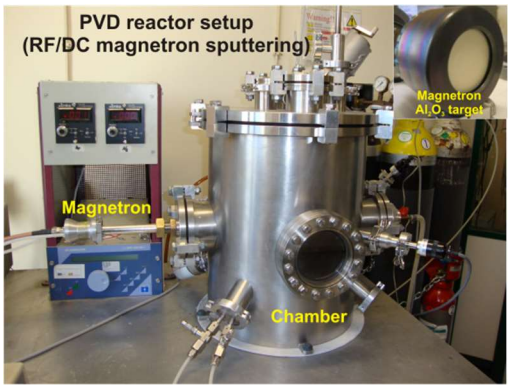

Figure I.19. Optical image of the PVD reactor setup (magnetron sputtering). The inset shows the magnetron with an Al_2O_3 target.

References

[1] J.R. Miller, P. Simon, *Science* **2008**, *321*, 651.

[2] P. Simon, Y. Gogotsi, *Nat. Mater.* **2008**, *7*, 845.

[3] B.E. Conway, *J. Electrochem. Soc*. **1991**, *138*, 1539.

[4] E. Frackowiak, F. Bélguin, *Carbon* **2001**, *39*, 937.

[5] D.D. Zhao, S.J. Bao, W.J. Zhou, H.L. Li, *Electrochem. Commun.* **2007**, *9*, 869.

[6] G. Wang, L. Zhang, J. Zhang, *Chem. Soc. Rev.* **2012**, *41*, 797.

[7] F. Fusalba, N.E. Mehdi, L. Breau, D. Bélanger, *Chem. Mater.* **2002**, *12*, 2581.

[8] K. R. Prasad, K. Koga, N. Miura, *Chem. Mater.* **2004**, *16*, 1845.

[9] A.K. Shukla, A. Banerjee, M.K. Ravikumar, A. Jalajakshi, *Electrochim. Acta* **2012**, *84*, 165.

[10] S. Bose, T. Kuila, A.K. Mishra, R. Rajasekar, N.H. Kim, J.H. Lee, *J. Mater. Chem.* **2012**, *22*, 767.

[11] D.N. Futaba, K. Hata, T. Yamada, T. Hiraoka, Y. Hayamizu, Y. Kakudate, O. Tanaike, H. Hatori, M. Yumura, S. Iijima, *Nat. Mater.* **2006**, *5*, 987.

[12] M. Inagaki, H. Konno, O. Tanaike, *J. Power Sources* **2010**, *195*, 7880.

[13] S. Talapatra, S. Kar, S.K. Pal, R. Vajtai, L. Ci, P. Victor, M.M. Shaijumon, S. Kaur, O. Nalamasu, P.M. Ajayan, *Nat. Nanotechnol.*, **2006**, *1*, 112.

[14] H. Zhang, G. Cao, Y. Yang, *Energy Environ. Sci.*, **2009**, **2**, 932-943.

[15] M. Ritala, M. Leskela, *in Handbook of Thin Film Materials (Ed. H.S. Nalwa),*

Vol. 1, Academic Press, San Diego, CA, **2002***,* 103.

[16] M. Knez, K. Nielsch, L. Niinistö, *Adv. Mater.* **2007**, *19*, 3425.

[17] R.L. Puurunen, *J. Appl. Phys.* **2005**, *97*, 121301.

[18] H. Kim, H.B.R. Lee, W. J. Maeng, *Thin Solid Films* **2009**, *517*, 2563.

[19] C.S. Hwang, in *Atomic Layer Deposition of Nanostructured Materials*, (eds: N. Pinna, M. Knez), Wiley-VCH, **2011**, 161.

[19] X. Wang, G. Yushin, *Energy Environ. Sci.* **2015**, *8*, 1889.

[21] G.D. Nessim, *Nanoscale* **2010**, *2*, 1306-1323.

[22] C. Mattevi, C.T. Wirth, S. Hofmann, R. Blume, M. Cantoro, C. Ducati, C. Cepek, A. Knop-Gericke, S. Milne, C. Castellarin-Cudia, S. Dolafi, A. Goldoni, R. Schloegl, J. Robertson, J. *J. Phys. Chem. C* **2008**, *112*, 12207.

[23] B. Zhao, D.N. Futaba, S. Yasuda, M. Akoshima, T. Yamada, K. Hata, *ACS Nano* **2008**, *3*, 108.

[24] A. Gohier, C.P. Ewels, T.M. Minea, M.A. Djouadi, *Carbon* **2008**, *46*, 1331.

[25] W. Yi, Q. Yang, *Diam. Relat. Mater.*, 2010, **19**, 870-874.

[26] H. Zhang, G. Cao, Z. Wang, Y. Yang, Z. Shi, Z. Gu, *Nano Lett.* **2008**, *8*, 2664.

[27] M. Toupin, T. Brousse, D. Bélanger, *Chem. Mater.* **2004**, *16*, 3184.

[28] X. Meng, M. Ionescu, M. Banis, Y. Zhong, H. Liu, Y. Zhang, S. Sun, R. Li, X. Sun, *J. Nanopart. Res.* **2011**, *13*, 1207.

[29] B. Lee, G. Mordi, M.J. Kim, Y.J. Chabal, E.M. Vogel, R.M. Wallace, K.J. Cho, L. Colombo, J. Kim, *Appl. Phys. Lett.* **2010**, *97*, 043107.

[30] A.A. Dameron, S. Pylypenko, J.B. Bult, K.C. Neyerlin, C. Engtrakul, C. Bochert, G.J. Leong, S.L. Frisco, L. Simpson, H.N. Dinh, B. Pibovar, *Appl. Surf. Sci.* **2012**, *258*, 5212.

[31] D.B. Farmer, R.G. Gordon, *Nano Lett.* **2006**, *6*, 699.

[32] X. Meng, Y. Zhong, Y. Sun, M.N. Banis, R. Li, X. Sun, *Carbon*, **2011**, *49*, 1133.

[33] J.P. Paraknowitsch, A. Thomas, *Energy Environ. Sci.* **2013**, *6*, 2839.

[34] M. Terrones, P. Ajayan, *Appl. Phys. A* **2002**, *74*, 355.

[35] E.J. Biddinger, D. von Deak, U.S. Ozkan, *Top. Catal.* **2009**, *52*, 1566.

[36] C. Marichy, M. Bechelany, N. Pinna, *Adv. Mater.* **2012**, *24*, 1017.

[37] B.E. Conway, *Electrochemical Supercapacitors: Scientific Fundamentals and Technological Applications*, *Plenum*, New York, **1999**.

[38] E. Frackwiak, *Pys Chem Chem Phys* **2007**, *9*, 1774-1785.

[39] S. T. Senthilkumar, R. K. Selvan, N. Ponpandian, J. S. Melo, *RCS Adv.* **2012**, *2*, 8937-8940.

[40] S. Zhang, N. Pan, *Ad. Energy Mater.* **2014**, 1401401, 1-19.

[41] C.R. Brundle, C.A. Evans, Jr., S. Wilson, in *Encyclopedia of materials characterization: surfaces, interfaces, thin films*, Butterworth-Heinemann, a division of Reed Publishing, **1992**.

[42] D.B. Williams, C.B. Carter, in *Transmission Electron Microscopy: A Textbook for Materials Science*, Springer, **2009**.

[43] G.C. Smith, *Mater. Charact.* **1990**, *25*, 37-71.

[44] G. Guaglitz, T. Vo-Dinh, in *Handbook of Spectroscopy*, WILEY-VCH GmbH, **2003.**

Chapter II

Chapter preface

The main contents of this chapter were already published as a paper in Applied Surface Science journal. The purpose of this work was the modification of vertically aligned carbon nanotubes by *in situ* functionalization through nitrogen (N) incorporation during the carbon nanotubes (CNTs) growth process (i.e. thermal chemical vapor deposition) in order to further improve their manipulation. For example, the surface functionalization of the nanotubes through the N moieties which can act as chemically active sites and thereby induce atomic layer deposition film growth as further demonstrated in this thesis.

"Vertically aligned N-doped CNTs growth using Taguchi experimental design"

R.M. Silva, A.J.S. Fernandes, M.C. Ferro, N. Pinna, R.F. Silva, *Appl. Surf. Sci.* **2015**, *344*, 57-64.

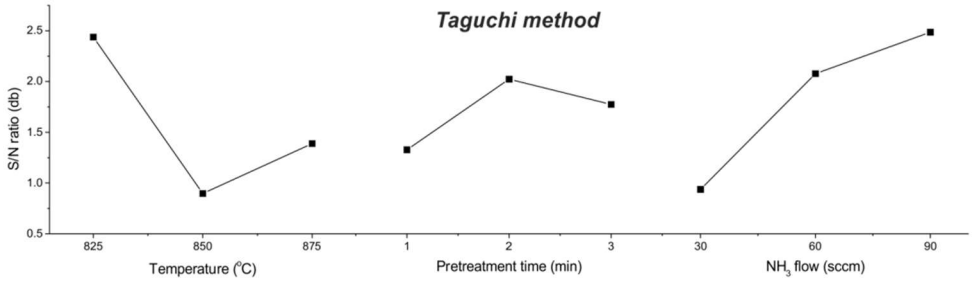

This manuscript received the contributions from M.C. Ferro and A.J.S. Fernandes, in terms of electron microscopy and Raman spectroscopy measurements and interpretation, respectively.

Vertically aligned N-doped CNTs growth using Taguchi experimental design

Abstract

The Taguchi method with a parameter design L_9 orthogonal array was implemented for optimizing the nitrogen incorporation in the structure of vertically aligned N-doped CNTs grown by thermal chemical deposition (TCVD). The maximization of the I_D/I_G ratio of the Raman spectra was selected as the target value. As a result, the optimal deposition configuration was NH_3=90 sccm, growth temperature=825ºC and catalyst pretreatment time of 2 min, the first parameter having the main effect on nitrogen incorporation. A confirmation experiment with these values was performed, ratifying the predicted I_D/I_G ratio of 1.42. Scanning electron microscopy (SEM) characterization revealed a uniform completely vertically aligned array of multiwalled CNTs which individually exhibit a bamboo-like structure, consisting of periodically curved graphitic layers, as depicted by high resolution transmission electron microscopy (HRTEM). The X-ray photoelectron spectroscopy (XPS) results indicated a 2.00 at.% of N incorporation in the CNTs in pyridine-like and graphite-like, as the predominant species.

II.1. Introduction

Energy storage systems represented by rechargeable batteries and supercapacitors are receiving increasing attention, as their applications are successively expanding from small-scale mobile electronics to large-scale transportations and utility grids [1-3]. Due to their unique combination of properties, carbon nanotubes (CNTs) are recognized materials in this field. As a matter of fact, the study of properties and applications of pristine CNTs has progressed enormously in the recent years and a great interest has been lately observed towards improving and controlling their properties through different functionalization methods. A modification of the crystalline nanotube properties by controllably placing defects or foreign atoms (heteroatoms) brings along tremendous technological applications [4]. Actually, the tuning of the CNT synthesis conditions can lead to significant variations in nanotube structure. One of the important possibilities of CNT modification is doping with nitrogen. Doping can dramatically change the electrical properties of the CNTs and the versatile thermal chemical vapor deposition (TCVD) technique has emerged as the most promising approach for mass production of CNTs. Namely, it has the ability to directly grow dense aligned CNTs, ranging within the μm/cm scale length, not only of pure carbon structures but also of hetero-atoms doped structures, like nitrogen doped (N-doped) CNTs (N-CNTs) [5].

Nitrogen is considered one of the best dopants for carbon materials because the atomic radius of nitrogen is close to that of carbon. Nitrogen doping of CNTs creates an electron donor in the conduction band (n-type dopant), resulting in significant changes in internal structure, electrical conductivity and chemical reactivity. It is generally accepted that, the incorporation of nitrogen into a graphitic network can take place in one of two main ways: (i) graphitic-like and (ii) pyridine-like nitrogen. In graphitic-like incorporation, nitrogen bonds in same way as carbon, that is, with three bonds to other carbons. In the case of pyridine-like inclusion the nitrogen is bound to two carbon atoms [4]. When electrochemical surface reactions are present, like the oxygen reduction reaction (ORR) in fuel cells and supercapacitors, the different types of N species incorporated the carbon network are of noteworthy importance as much as the total nitrogen content [6-8]. The content of nitrogen in N-CNTs mainly depends on the solubility of the nitrogen in the catalyst nanoparticle at the temperature maintained during the synthesis and the concentration of the nitrogen-containing compound in the reaction mixture. These dissolved N atoms would precipitate with the C atoms during the growth of CNTs and this type of CNTs exhibit a bamboo-like structure in which the tube inside is separated into a series of compartments [9,10].

Different kinds of nitrogen sources have used to dope CNTs, namely the using of non-gaseous N precursor such as the injection of liquid organic chemical compounds rich in N have shown advantages in the growth of N-CNTs, especially by tailoring of number of walls of the N-CNTs ranging from single to multi walls [11-13]. In addition, Elías *et al.* demonstrated that the changes on the electrical properties of the grown single-walled N-CNTs are related to the various concentrations of N liquid source in the feedstock [14]. Another way of adding nitrogen to the reaction environment is the incorporation of ammonia in gaseous form at room temperature, which can be simply added to the TCVD set up. The use of NH_3 as N dopant produces mainly multi-walled N-CNTs. Doping levels achieved by this approach vary in the 0.4-9 at.% range of N, depending on the carbon gas source, catalyst precursor and deposition temperature [13]. Other nitrogen sources (e.g., melamine, pyridine, N_2) can be used to grow N-CNTs, as also as more elaborated techniques (e.g., arc discharge, plasma or bias-assisted CVD), these leading to improved N incorporation levels (up to 30 at.%) [13]. In short, it is possible to tune the N content and the number of walls of the N doped CNTs through the selection of the proper growth method and doping source.

Another important consequence of nitrogen incorporation in CNTs is the net increasing of defects on the CNT walls, changing the chemical behavior of a CNT. This procedure provides an alternative, less destructive, method to the classical oxidation methodology that typically uses nitric acid to functionalize the CNT surface. It is generally accepted that the N-modified CNTs will have more opportunities for practical applications [15]. Hence the N-CNTs are ideally suitable as support for a second material that can be deposited onto their surface, either as individual particles or as a film making them an ideal building block in heterostructured materials [4,16].

The purpose of this work is to investigate the effects of the N doped CNTs growth parameters in a systematic manner through the Taguchi experimental design. Thermal CVD is a growth technique which involves a large number of tunable parameters, such as the carbon precursor and nitrogen doping source and catalyst, the type of carrier gas and its flow rate, and deposition temperature. The Taguchi methodology involves identification of controllable and uncontrollable parameters and the establishment of a series of experiments to determine their optimal combination, which has the greatest influence on the performance and least variation from the target design [17-22]. Specifically, in the present study the variables considered for the determination of the optimum level for each factor are: growth temperature, pretreatment time and ammonia flow rate. An L_9 orthogonal array (9 experiments, 3 control factors and 3 levels) was created in the statistical design of experiments with the goal of maximization of the N incorporation in the structure. In this context, the I_D/I_G ratio as determined by Raman studies was selected as output response of the deposition process. The ratio of the integrated areas of the D and G bands (I_D/I_G) is often used to evaluate the degree of crystallinity in the CNTs. In this context, a lower value of the ratio indicates a less amount of defects in graphene-based structure of CNT materials [23]. Actually, the D band originates from the defects and would provide information on the level of disorder as a result of nitrogen doping. On the other hand, the G band results from the presence of defect-free crystalline graphitic carbon.

The morphology of the vertically aligned N-doped CNTs and the internal structure of the N-CNTs were investigated using scanning electron microscopy (SEM) and transmission electron microscopy (TEM). The content and type of nitrogen incorporation in the N-CNTs was estimated from X-ray photoelectron spectroscopy (XPS) measurements. The statistical software MINITAB 16 was used for the design of experiments (DoE) based on the Taguchi method.

II.2. Experimental details

II.2.1. Catalyst preparation

Polished Si (100) wafers with 200 nm thermally grown SiO_2 were used as substrates. A preliminary set of experiments involving the use of different thickness of Fe films were carried out. The substrates were initially coated with a buffer layer of 10 nm thick Al_2O_3 and a catalyst film of 1, 2, 3 and 10 nm thick Fe by physical vapor deposition (PVD-RF and DC magnetron sputtering, respectively), followed by TCVD growth (Figure II.1). More details of the Al_2O_3 and Fe film deposition were described in previous work [24]. This preliminary work enabled us to understand the catalyst thickness effect on the growth of the N-CNTs by evaluating the correlation between the catalyst thickness and the length of the grown N-CNTs assessed by SEM. We observed that the N-CNTs preferentially grow on 10 nm thick Fe film with vertically alignment and uniformity. Therefore, the catalyst thickness of 10 nm was kept constant for experiments of the Taguchi experimental design.

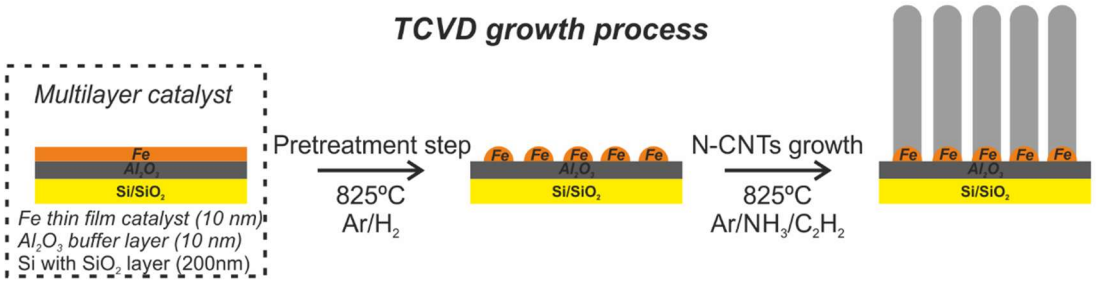

Figure II.1 Schematic illustration of the N-CNTs growth process (drawing not to scale).

II.2.2. Synthesis of N-doped CNTs

Nitrogen doped carbon nanotubes (N-CNTs) were grown by thermal CVD in a furnace reactor. The TCVD set-up consists of a horizontal mounted quartz tube (diameter ~ 5cm) coupled to a thermal heating, equipped with various gas lines and standard mass flow controllers to control the flow of carbon source (C_2H_2), reducing gas (H_2), doping gas (NH_3) and inert carrier gas (Ar) into the furnace and a PC station for automatic operation. The substrates coated with the catalytic layer were cut into 5x5 mm and placed into the quartz tube of the furnace. The reactor was evacuated to 3.0 x 10^{-3} mbar with a rotary pump. The quartz tube was subsequently filled with Ar up to atmospheric pressure. The substrate was pulled to the center of the reactor. Then, a two-step annealing process was initialized. The time of the first annealing step, in an Ar flow (750 sccm), was 5 min. The time of the second annealing step, in a reductive flow of Ar (200 sccm) and H_2 (500 sccm), was varied from 1 to 3 min. The N-CNTs growth was undertaken with a total gas flow of 510 sccm where the C_2H_2 flow was fixed at 10 sccm. The doping gas (NH_3) flow rate

varied in the range of 30-90 sccm. The gas mixture was introduced for 15 min in the quartz tube where the temperature of the hot zone was set in the range of 825-875ºC. All these parameters were selected accordingly to preliminary set of experiments and literature data review [5,9,10,23], that pointed out these conditions as suitable for the N-CNTs synthesis.

II.2.3. Sample characterization

Scanning electron microscopy (SEM) was performed with a Hitachi SU-70 microscope operated in secondary electron mode at 15 kV. Transmission electron microscopy (TEM) measurements were carried out on a JEOL JEM-2200FS microscope operated at 200 kV. The sample for TEM measurements was prepared by dry adhesion of the N-CNTs to a holey carbon grid from an N-CNTs forest. Raman spectroscopy (Jobin Yvon T64000) was carried out at a 532 nm excitation wavelength on the as-grown N-CNTs. The Raman spectra were taken at room temperature and two different locations are sampled. The values of I_D/I_G ratio were estimated from integrated area intensities of the D and G band peaks. Atomic force microscopy (AFM) measurements were performed with an Ntegra Prima setup (NT-MDT) in tapping mode. A silicon cantilever (Nanosensor PPP-NCHR) with the spring constant of $k \approx 42$ N m^{-1} and tip radius less than 10 nm was used. X-ray photoelectron spectroscopy (XPS) was conducted with a Kratos AXIS Ultra HAS. The analysis was carried out with a monochromatic Al Kα X-ray source (1486.7 eV), operating at 90 W, in FAT mode (Fixed Analyser Transmission), with a pass energy of 80 eV for survey spectra and 40 eV for high resolution energy spectra. The high resolution energy spectrum was used to determine the chemical environment and quantification of the elements present in the sample. Therefore, the N 1s spectrum was fitted to Gaussian functions. The N content, defined as atomic percentage of N with respect to the sum of C and N peaks, is estimated by the peak area ratio between N and N+C.

II.2.4. Taguchi design of growth experiments

In the N-CNTs synthesis process, three control factors (growth parameters) with three levels were experimented, leading to nine CVD experiments organized in a L_9 Taguchi array design. The three growth parameters that were investigated were: i) growth temperature (values of 825, 850 and 875 ºC); ii) second annealing step hereinafter referred as pretreatment time (1, 2 and 3 min); and iii) doping gas (NH_3) flow rate (30, 60 and 90 sccm). Subsequently, the I_D/I_G ratio was selected as the physical quantity of interest to be the output response of the deposition process. The Taguchi method employs a generic signal-to-noise (S/N) ratio as quantitative measure for determining the optimum deposition conditions. There are primarily three categories of S/N ratios, namely, the “smaller-is-better” type, the “larger-is-better” type, and the “nominal-is-best” type to choose from. The selection principles of S/N ratio depend on the goal of the design. Hence, the maximization

of the N incorporation in the nanotubes structure is the goal of this design, the "larger-is-better" approach was adopted, in which the S/N ratio is calculated from Equation 1:

$$S/N_{larger-is-better} = -10\log_{10}\left[\frac{1}{n}\sum_{i=1}^{n}\frac{1}{Y_i^2}\right] \qquad \text{Equation (1)}$$

where S/N indicates the signal to noise ratio statistic used in the Taguchi parameter analysis, n is the number of experiments, and Y_i the *i*th value of the output response used for the evaluation of the experiment [16,17]. Hence the variation analysis of S/N ratios can be used to study the most significant factors affecting the N-CNTs growth via TCVD. The parameter design for N-CNTs growth process and the system response are exhibited in Table II.1. The samples obtained under Taguchi array design are labeled as R_n with *n* a number running from 1 to 9.

Table II.1. Parameter design and results of the growth experiments.

***L*₉**	***Factor A***	***Factor B***	***Factor C***	***Response***
Run	Temperature (ºC)	Pretreatment time (min)	NH_3 flow (sccm)	I_D/I_G ratio
R1	825	1	30	1.13
R2	825	2	60	1.39
R3	825	3	90	1.48
R4	850	1	60	1.11
R5	850	2	90	1.34
R6	850	3	30	0.93
R7	875	1	90	1.24
R8	875	2	30	1.02
R9	875	3	60	1.29

II.3. Results and Discussion

II.3.1. Results of Taguchi-designed experiments

In all experiments the N-CNTs have grown uniformly and normal to the substrate, normally assigned as vertically aligned N-CNTs or N-CNT forests, as shown in Figure II.2a. The rightmost column of Table II.1 reports the N-CNTs I_D/I_G ratio as estimated from Raman studies. The results are illustrated in Figure II.2b, which shows the Raman spectrum for each experiment of the Taguchi array. The main features in the Raman of CNTs are the so-called D and G bands, which lie at around 1340 cm^{-1} and 1580 cm^{-1} respectively.

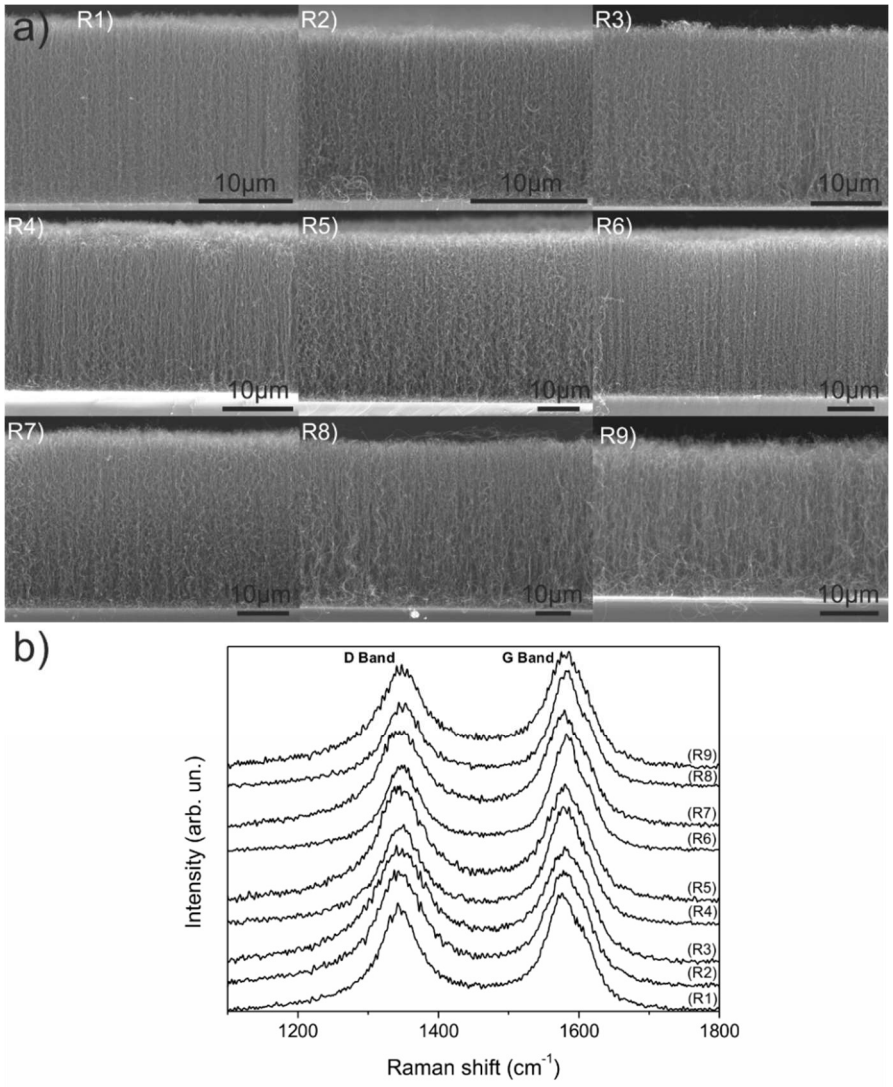

Figure II.2. SEM cross-section images (a) and Raman spectra (b) of N-CNT forests grown from runs 1-9 of the Taguchi array in Table 1: R1, R2, R3, R4, R5, R6, R7, R8 and R9. The Raman spectra were normalized to the intensity of the G band. Note that the D band is slightly shifted to the left.

The conditions used for experiment 3 (Figure II.2b R3) appear to be the most promising in order to growth N-CNTs forests, with an I_D/I_G ratio of 1.48 (Table II.1). In fact, varying the growth temperature, pretreatment time and NH_3 flow produces changes in the I_D/I_G ratio ranging from 0.93 to 1.48. At lower NH_3 flow rate (i.e. 30 sccm) the I_D/I_G ratio attains the lowest ratio of 0.93. On the other hand, at higher NH_3 flow rate (i.e. 90 sccm), the value of the I_D/I_G ratio is observed to be 1.48. These results confirm the influence of the N content on the integrated area intensity ratio of D band to G band (I_D/I_G). As a matter of fact, the N-doping of CNTs is known to degrade the crystallinity of graphitic layers [25].

II.3.2. Response and variance analysis

In order to assess in which extent each of the selected control factors is influential on the I_D/I_G ratio and based on the results presented in Figure II.2, the corresponding S/N response table and S/N response graph were determined, according to Taguchi method, as shown in Table II.2 and Figure II.3, respectively.

Table II.2. Response table of S/N ratios: larger-is-better.

Level	Temperature (ºC)	Pretreatment time (min)	NH_3 flow (sccm)
1	2.4372	1.2361	0.1813
2	0.8965	1.8544	1.9533
3	1.3892	1.6324	2.5883
Delta	1.5407	0.6184	2.4070
Rank	2	3	1

The response table (Table II.2) shows the average of each response characteristic (S/N ratios) for each level of each factor. The tables include ranks based on the Delta statistic value, defined as the difference between the high and the low effect of each factor. The higher rank is assigned to the highest Delta value, which gives the highest contribution to the I_D/I_G ratio intensity. In this context, the factor with the largest impact on the S/N ratio is the NH_3 flow rate and that with lowest impact is the pretreatment time, which is in agreement with the less pronounced variation of the S/N ratio values.

In the response graphs of S/N ratios in Figure II.3, the I_D/I_G ratio intensity increased by increasing the NH_3 flow rate concomitantly with the concentration of the nitrogen-containing compound inthe reaction mixture. Although the less pronounced variation of the S/N ratio for larger-is-better analysis is due to the pretreatment time, this parameter plays an important role in the N-CNTs growth process. This is because during this step the catalyst film is subjected to a thermal treatment in a reducing gas environment (H_2) in order to remove surface oxides and it needs to be broken into nanosized islands (Figure II.4) for the nanotubes to grown on it. In fact, when N-CNTs growth starts, a vertical orientation emerges if there is enough density of the growing nanotubes to cause “crowding effect”.

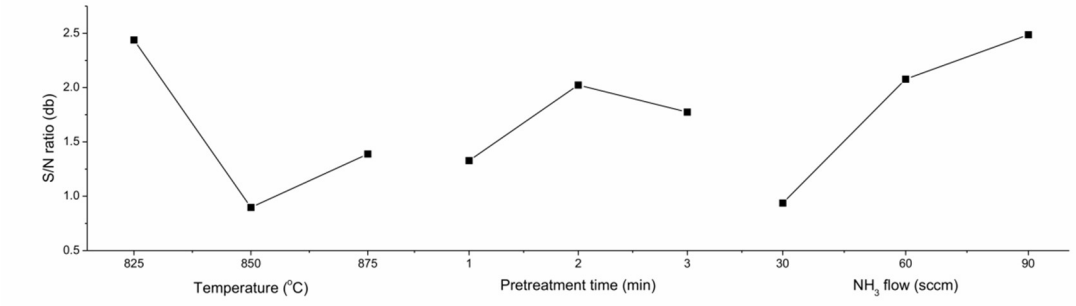

Figure II.3. Response graphs of S/N ratio for larger-is-better analysis of N-CNTs I_D/I_G ratio evaluation.

Figure II.4a shows the SEM image of the morphology and distribution of the catalyst nanosized islands prior to the N-CNTs growth and they appear as granular film. This finding is also in good agreement with AFM investigation on the same sample. The surface topography obtained by AFM with a root mean square (RMS) roughness of 12.89 nm, as presented in Figure II.4b.

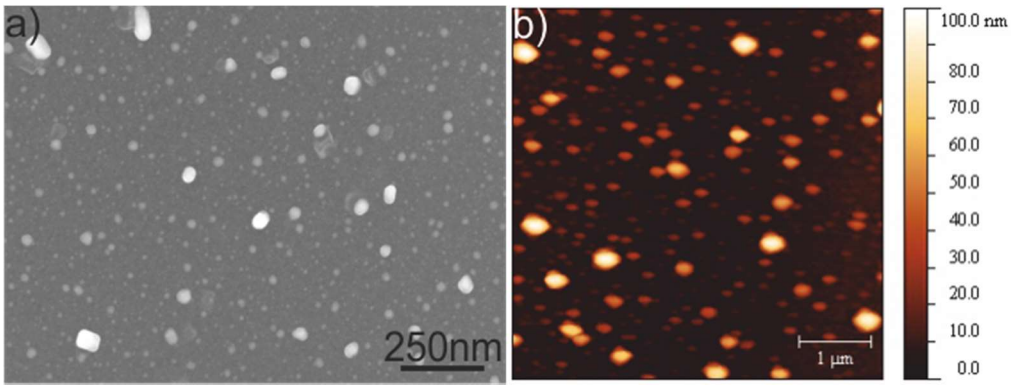

Figure II.4. SEM and AFM image (a,b) of the catalyst film after the pretreatment in 200/500 sccm Ar/H_2 for 2 min at 825ºC (size of AFM image is 5 µm x 5 µm). It is worth to note that to minimize the morphology alteration during the cooling process, the catalyst was quenched rapidly to room temperature.

In addition to this, in order to understand the impact of various control factors on the response of experimental data, it is desirable to develop the ANOVA variance analysis and to find the significant factors in the Taguchi array. The ANOVA approach is applied to determine percentage contribution for each controlling factor, as shown in Table II.3. In this table, the percentage of contribution of each factor on the response is given by $\% = SS / SS_{total} \times 100$ and the *SS* is known as sum of squares. Furthermore, the F-value can also be used to determine which factor has a significant effect on the physical quantity of interest. Specially, when the F-value is large, it means that the change of a determined

factor has a significant effect on the considered output. If the observed p-value is less than the significance level (0.05) this indicates that the design parameters are statistically significant. It is observed from this table that the NH_3 flow rate plays the most major contribution to the I_D/I_G ratio, reaching as high as 63.31%. Next, the growth temperature also gives a fairly large contribution of 26.72%. On the other hand, the pretreatment time contribution of 5.61% seems to play a minor role on the I_D/I_G ratio intensity. From a statistic table the critical $F_{(3,11)}$ value can be determined as 3.98 for a level of significance equal to 0.05. This critical F value is lower compared to F-value obtained for each factor which means that all factors are significant for this purpose.

Table II.3. Analysis of variance (ANOVA computed using Minitab software)

Source	*Degree of freedom (DF)*	*Sum of squares (SS)*	*Adjusted mean square (Adj SS)*	*F-value*	*p-value*	*Percentage of contribution (%)*
[a]T (ºC)	2	0.1434	0.0717	33.74	0.000	26.72
[b]PT (min)	2	0.0301	0.0150	7.08	0.011	5.61
NH_3 flow (sccm)	2	0.3397	0.1699	79.91	0.000	63.31
Error	11	0.0234	0.0021			4.36
Total	17	0.5366				100

[a]Temperature (ºC); [b]Pretreatment time (min).

II.3.3. Prediction and confirmation experiment

The Taguchi method also allows the prediction of the output values that can be achieved by setting control-factors at the corresponding optimal configuration [21,26]. Based on the previous discussion, it is expected that the N-CNTs forest with highest I_D/I_G ratio intensity is obtained at a temperature of 825ºC, 2 min of pretreatment time and 90 sccm flow rate of NH_3. Therefore, the final step is to predict and verify the improvement of the quality characteristic using the optimal configuration of the design parameters. The expected value of I_D/I_G ratio can be estimated by firstly calculating the predicted S/N ratio. Its calculation was accomplished by using Minitab software, the resulting value being presented in Table II.4.

Table II.4. Optimal configuration and predicted S/N ratio value.

Temperature (ºC)	Pretreatment time (min)	NH_3 flow (sccm)	S/N ratio
825	2	90	3.02829

By using the predicted S/N value for I_D/I_G ratio the corresponding estimated I_D/I_G ratio can be calculated by written the Equation 1 as $3.02829 = 10\log_{10} Y^2$. Finally, the predicted Y (I_D/I_G ratio) value is 1.417. In order to test this prediction one additional experiment is

carried out. Figure II.5a shows the Raman spectrum of the N-CNTs forest obtained from the optimal configuration. The observed I_D/I_G ratio of 1.425 is in very good agreement with the predicted value. Consequently, the model provides valid predictions otherwise the above steps must be iterated.

Detailed surface morphological and structural investigations have been also carried out on the sample used in confirmation experiment. The inset of Figure II.5b shows the SEM image of the vertically well-aligned N-CNTs forest homogeneously grown on a large area of the substrate. The close up cross section image (Figure II.5b) emphasizes the alignment of the N-CNTs that is an inherent feature of the growth process of forest depicting a relatively dense material. At this optimal configuration, the grown N-CNTs exhibit a length of 16 µm.

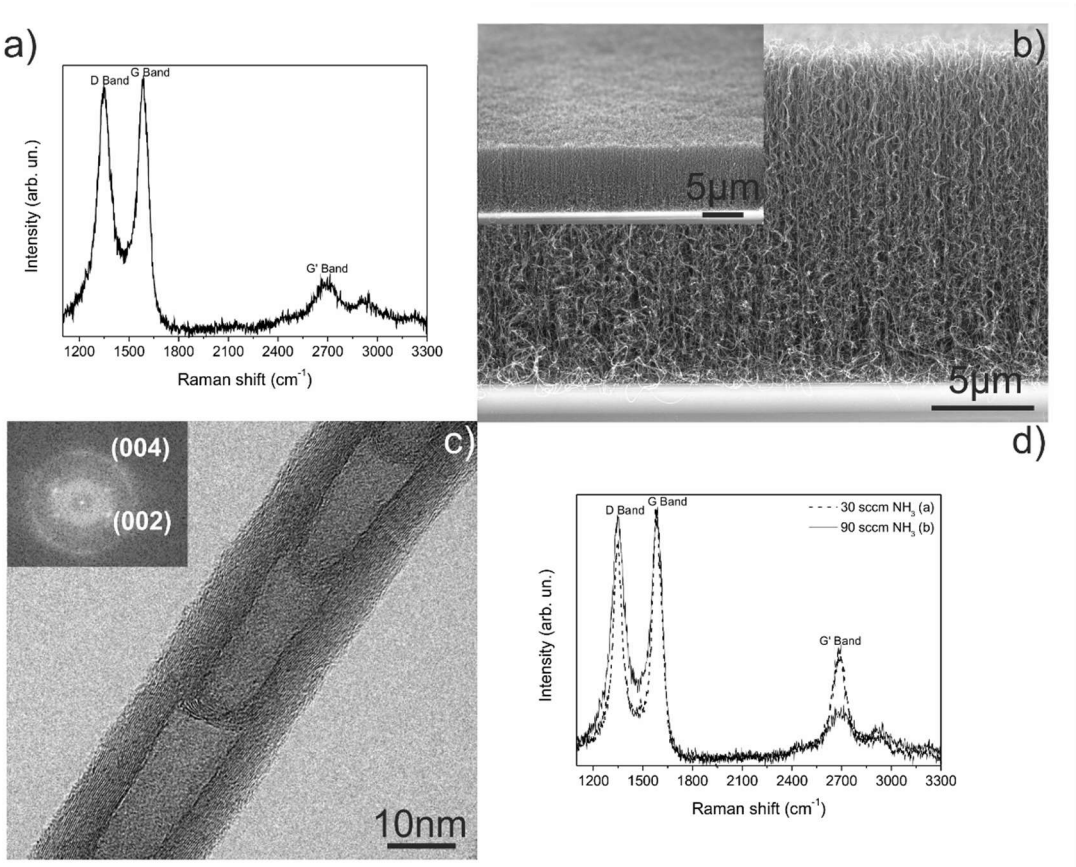

Figure II.5. Raman spectrum (a), SEM (b) and HRTEM (c) images of the N-CNTs forest from the confirmation experiment. First and second-order Raman spectra (d) of N-doped multiwalled CNTs grown with (a) 30 and (b) 90 sccm of NH_3.

High resolution TEM images present more detailed information about the internal structure of N-CNTs. In Figure II.5c it is seen that the N-CNTs exhibit the typical bamboo-like structure which consists of periodically curved graphitic layers. The crystallinity of the N-

CNTs was examined by HRTEM together with Fast Fourier Transform (FFT). The ring-like pattern in FFT (inset) displayed in Figure II.5c indicates the (002) and (004) planes of the graphite and the graphite walls still exhibit a good degree of crystallinity. The multi-walled nature of as-grown N-CNTs illustrated by the TEM studies is in good agreement with the Raman measurements.

II.3.4. Detailed analysis of the variation of the NH_3 flow parameter

Among the analyzed growth parameters, we have found that the NH_3 flow rate is the most important control factor in the N doping process, supported by the larger-is-better analysis of the I_D/I_G ratio. In order to emphasize the importance of this parameter, the Raman spectra of N-CNTs synthesized with 90 and 30 sccm of NH_3 under the same growth temperature of 825ºC and pretreatment time of 2 min, are compared in Figure II.4d. Besides the strong G and D band characteristic of the first order Raman spectra of all graphitic materials, including multiwalled CNTs, there is another feature, the so-called 2D band located at 2700 cm^{-1}, the most prominent second-order Raman peak whose frequency is approximately twice of the D band frequency. The origin of the 2D band is independent of the structural defects [25,27,28]. Comparing the Raman spectra in this plot, when the NH_3 flow was reduced from 90 to 30 sccm, it was found that the 2D band increased its intensity and became narrower. So, if on one hand the 2D band is not related to the structural defects, on the other hand the 2D band is sensible to the N incorporation, which could be due to a modification in the electronic structure of nanotubes as a result of N doping [25,27].

This modification in the electronic structure of the N-CNTs may be directly related with the content and type of the incorporated N. Therefore, the precise composition of the grown N-CNTs requires X-ray photoelectron spectroscopy (XPS) analysis which is a very powerful technique to study the nitrogen incorporation in the nanotube structure and its chemical environment. The XPS survey full scan spectrum of the obtained N-CNTs from the confirmation experiment is shown in Figure II.6a. The XPS measurements reveal the elemental composition of the sample where the main peaks are assigned to C 1s, N 1s edges of the N-doped CNTs and O 1s edge to corresponding to 285, 400 and 532 eV, respectively. The oxygen may arise from the oxygenated species created at the surface of the nanotubes once removed from the CVD chamber or in adsorbed form. A detail of the N 1s XPS spectrum of the N-CNTs is shown in Figure II.6b. This spectrum presents at least three peaks corresponding to the different N chemical environment and these peaks can be assigned to the pyridine-like N where the N atom is bonded with two C atoms (398.92 eV), graphite-like N where the N atom replaces a graphitic C atom (401.72 eV) and to nitrogen oxide species (404.98 eV). According to the literature [28,29] regarding N1s XPS spectrum, the same peaks were found when using NH_3 as doping source. The total N content is determined to be 2.00 at.%.

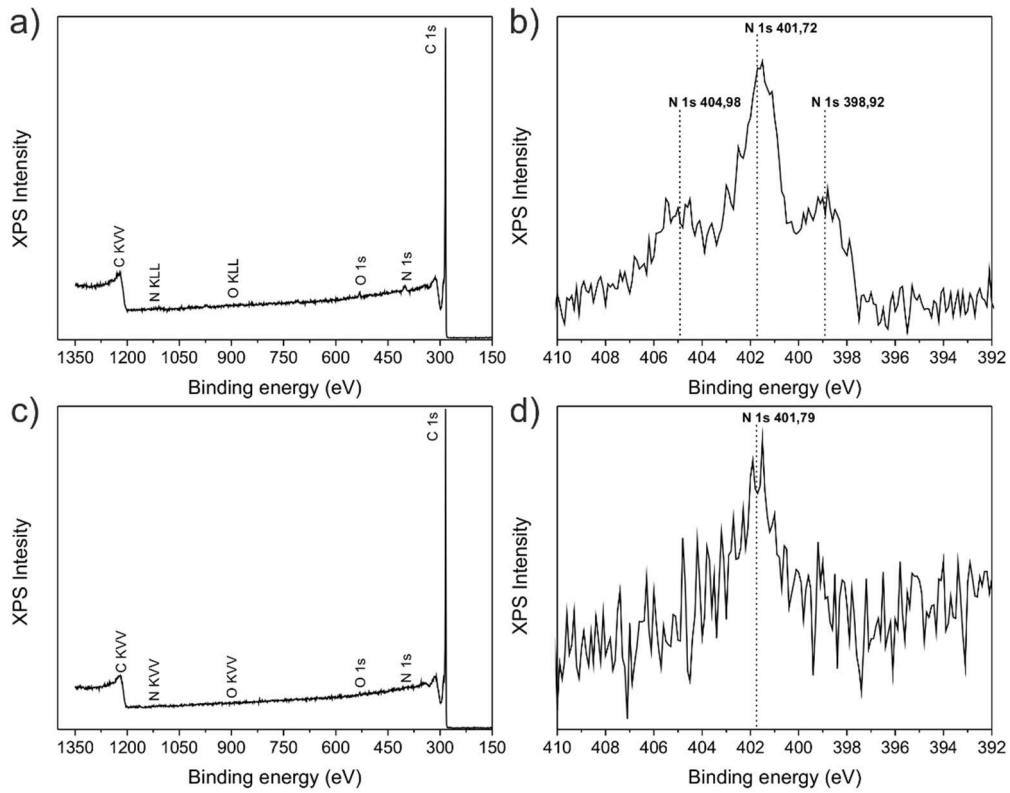

Figure II.6. XPS spectra of N-CNTs grown with 90 and 30 sccm of NH_3. (a,c) full scan; (b,d) N 1s spectrum, respectively.

In order to emphasize the importance of the NH_3 flow rate control factor, XPS analysis was conducted on N-CNTs grown under the same conditions with a lower content of NH_3 *e*.g. 30 sccm of NH_3 and its XPS survey full scan and N 1s spectrum is shown in Figure II.6c and d, respectively. The N 1s XPS spectrum consists in one peak located at 401.79 eV corresponding to the graphitic-like N. At a flow rate of 30 sccm, the N content in the nanotubes was reduced to 0.25 at.%.

According to the XPS results, the N in the nanotubes is chemically bonded with the C atoms of the graphitic network of the N-CNTs at a growth temperature of 825ºC. It can be seen that the graphitic-like N form is present in both samples. Furthermore, the N content decreased with decreasing the NH_3 flow rate from 90 to 30 sccm. This trend of changing the N content with respect to the variation of the N source concentration in the reaction environment was also observed by Maldonado *et al.* where a linear relationship between the increase in the N content with increasing fraction of NH_3 gas in the feedstock [30]. In addition, the I_D/I_G ratio intensity also decreased from 1.42 to 1.00 (Figure II.5d). Furthermore, the Raman spectroscopy was successfully used to follow the N incorporation into the graphitic network throughout the I_D/I_G ratio.

These results suggest that the content and type of the incorporated N induce the degradation of the crystallinity of graphitic layers which is consistent with the response graphs of S/N ratio. Moreover, the SEM investigations revealed that the vertically alignment of the N-CNTs forests was achieved for the set of Taguchi designed CVD experiments. As such, the vertically aligned N-CNTs may find potential applications in developing various nanodevices, taking advantage of their large surface area and highly ordered geometry, especially in energy related fields of applications such as fuel cells and supercapacitors where the N content and species play a crucial role in their electrochemical performance.

II.4. Conclusions

The Taguchi method was successfully used for optimizing the growth conditions of vertically aligned N-doped CNTs forests and to find the most suitable experimental conditions for the maximization of the N incorporation in the nanotube structure. Three design factors, namely the growth temperature, pretreatment time and NH_3 flow rate, were selected as the variables at three levels each and an L_9 orthogonal array was utilized for the design experiments. Moreover, the Taguchi methodology allowed us to identify the most important factor on the N-CNTs growth, which affects the selected response. In this context, the ratio of D and G band integrated area ratio (I_D/I_G) determined by Raman spectroscopy was selected as output response of the deposition process. The larger-is-better analysis of the I_D/I_G ratio revealed that NH_3 flow rate is the most important parameter and the ANOVA analysis provided the percentage contribution of each factor for results of the experiment in the following order: NH_3 flow rate > temperature > pretreatment time. By optimal configuration of this method, N-CNTs were prepared and these results were in agreement with predicted data analyzed by the Taguchi method. Moreover, it is reasonable to propose that the described method can be adopted to rapidly adapt a literature-based TCVD process to the local laboratory reactor. Transmission electron microscopy and Raman spectroscopy analysis of as-prepared N-CNTs depicted multi walled nanotubes with the typical bamboo-like structure. The XPS analysis revealed that the atomic percentage of N-doped in CNTs can be controlled by varying the NH_3 flow rate, attaining 2.00 at.% N for 90 sccm. Also, it showed that nitrogen is chemically bonded with the C atoms of the graphitic network.

References

[1] W.H. Shin, H.M. Jeong, B.G. Kim, J.K. Kang, J.W. Choi, *Nano Lett.* **2012**, *12*, 2283.

[2] H. Zhang, G. Cao, Y. Yang, *Energy Environ. Sci.* **2009**, *2*, 932.

[3] C. Du, J. Yeh, N. Pang, *Nanotechnology* **2005**, *16*, 350.

[4] P. Ayala, R. Arenal, M. Rümmeli, A. Rubio, T. Pichler, *Carbon* **2010**, *48*, 575.

[5] Y.T. Lee, J. Park, Y.S. Choi, H. Ryu, H. J. Lee, *J. Phys. Chem. B* **2002**,*106*, 7614.

[6] K.P. Gong, F. Du, Z. Xia, M. Durstock, L. Dai, *Science* **2009**, *323*, 760.

[7] D.S. Su, R. Schlögl, *ChemSusChem* **2010**, *3*, 136.

[8] J.P. Paraknowitsch, A. Thomas, *Energy Environ. Sci.* **2013**, *6*, 2839.

[9] Y.T. Lee, N.S. Kim, S.Y. Bae, J. Park, S.C. Yu, H. Ryu, H. J. Lee, *J. Phys. Chem. B* **2003**, *107*, 12958.

[10] J.B. Kim, C.D. Kim, S.J. Kong, J.H. Kim, B.K. Min, W.S. Jung, H.R. Lee, *AIP Conf. Proc.* **2011**, *1399*, 243.

[11] P. Ayala, A. Grüneis, T. Gemming, B. Büchner, M.H. Rümmeli, D. Grimm, J. Schumann, R. Kaltofen, F.L. Freire Jr., H.D. Fonseca Filho, T. Pichler, *Chem. Mater.* **2007**, *19*, 6131.

[12] P. Ayala, A. Grüneis, C. Kramberger, M.H. Rümmeli, I.G. Solórzano, F.L. Freire Jr., T. Pichler, *J. Chem. Phys.* **2007**, *127*, 1847091.

[13] S. Boncel, S.W. Pattinson, V. Geiser, M.S.P. Shaffer, K.K.K. Koziol, *Beilsten J. Nanotechnol.* **2014**, *5*, 219.

[14] A.L. Elías, P. Ayala, A. Zamudio, M. Grobosch, E. Cruz-Silva, J.M. Romo-Herrera, J. Campos-Delgado, H. Terrones, T. Pichler, M. Terrones, *J. Nanosci. Nanotechnol.* **2010**, *10*, 3959.

[15] D.H. Lee, W.J. Lee, S.O. Kim, *Nano Lett.* **2009**, *4*, 1427.

[16] D. Eder, *Chem. Rev.* 2010, 110, 1348.

[17] P.J. Ross, in *Taguchi Techniques for Quality Engineering*, 2nd edition, McGraw-Hill, **1996**.

[18] A.C. Tamhane, in *Statistical Analysis of Designed Experiments, Theory and Applications*; Wiley, **2009**.

[19] J.H. Ting, C.C. Chang, S.L. Chen, D.S. Lu, C.Y. Kung, F.Y. Huang, *Thin Solid Films* **2006**, *496*, 299.

[20] S. Porro, S. Musso, M. Giorcelli, A. Chiodoni, A. Tagliaferro, *Physica E* **2007**, *37*, 16.

[21] S. Ebrahimiasl, W.Md.Z. Yunus, A. Kassim, Z. Zainal, *Solid State Sciences* **2010**, *12*, 1323.

[22] S. Santagelo, M. Lanza, E. Piperopoulos, S. Galvagno, C. Milone, *Materials Research Bulletin* **2012**, *47*, 595.

[23] T. Sharifi, F. Nitze, H.R. Barzegar, C.W. Tai, M. Mazurkiewicz, A. Malolepszy, L. Stobinski, T. Wagberg, *Carbon* **2012**, *50*, 3535.

[24] D. Mata, R.M. Silva, A.J.S. Fernandes, F.J. Oliveira, P.M.F.J. Costa, R.F. Silva, *Carbon* **2012**, *50*, 3585.

[25] L.G. Bulusheva, A.V. Okotrub, I.A. Kinloch, I.P. Asanov, A.G. Kurenya, A.G. Kudashov, X. Chen, H. Song, *phys. stat. sol.* 2008, 245, 1971.

[26] S.M. Kim, K.S. Park, K.D. Kim, S.D. Park, H.T. Kim, J. Ind. Eng. Chem. **2009**, *15*, 894.

[27] M.S. Dresselhaus, A. Jorio, M. Hofmann, G. Dresselhaus, R. Satio, *Nano Lett.* **2010**, *10*, 751.

[28] J.C. Charlier, Defects in Carbon Nanotubes, *Acc. Chem. Res.* **2002**, *35*, 1063.

[29] J.W. Jang, C.E. Lee, S.C. Lyu, T.J. Lee, S.C. Lyu, T.J. Lee, *Appl. Phys. Lett.* **2004**, *84*, 2877.

[30] S. Maldonado, S. Morin, K.J. Stevenson, *Carbon* **2006**, *44*, 1429.

Chapter III

Chapter preface

The aim of this study was using the atomic layer deposition (ALD) technique as an indirect probing tool of the surface defects generated by *in situ* functionalization of the nanotubes through nitrogen (N) incorporation. Therefore, the resulting publication was concentrated on more fundamental aspects, such as the surface/interface between the two materials (N-doped CNTs/ZnO) and the growth mechanism. The focus on the ALD of ZnO is justified by the fact that it is a well-established and yet simple ALD process from a chemical and practical point of view. In this context, the reaction between the metal precursor and surface species (i.e. N moieties), which played a critical role to promote the film nucleation, was investigated. However, the as-prepared heterostructures are definitely appealing for a variety of applications.

"Nucleation, growth mechanism and controlled coating of ZnO ALD onto vertically aligned N-doped CNTs"

R.M. Silva, M.C. Ferro, J.R. Araujo, C.A. Achete, G. Clavel, R.F. Silva, N. Pinna, *Langmuir* **2016**, *32*, 7038-7044.

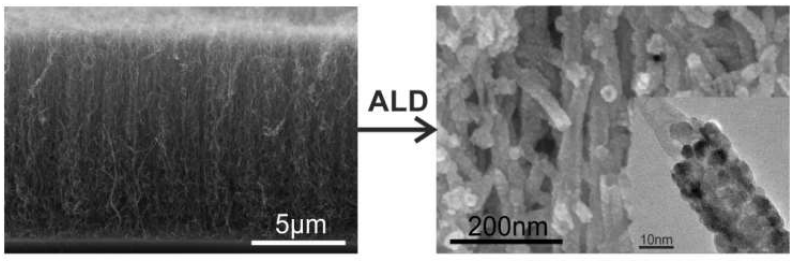

This manuscript received the contributions from M.C. Ferro, J.R. Araujo and C.A. Achete in terms of electron microscopy and X-ray photoelectron spectroscopy measurements and interpretation, respectively.

Nucleation, growth mechanism and controlled coating of ZnO ALD onto vertically aligned N-doped CNTs

Abstract

Zinc oxide thin films were deposited on vertically aligned nitrogen-doped carbon nanotubes (N-CNTs) by atomic layer deposition (ALD) from diethylzinc and water. The study demonstrates that doping CNTs with nitrogen is an effective approach for the "activation" of the CNTs surface for the ALD of metal oxides. Conformal ZnO coatings are already obtained after 50 ALD cycles, whereas at lower ALD cycles an island growth mode is observed. Moreover, the process allows for a uniform growth from the top to the bottom of the vertically aligned N-CNT arrays. X-ray photoelectron spectroscopy demonstrates that ZnO nucleation takes place at the N-containing species on the surface of the CNTs by the formation of the Zn-N bonds at the interface between the CNTs and the ZnO film.

III.1. Introduction

Atomic layer deposition (ALD) has emerged as a powerful technique for thin film deposition on high aspect ratio substrates. ALD is a self-limiting deposition technique based on surface chemical reactions of alternate surface-saturating precursor doses that keep the reactants separated, avoiding the occurrence of gas phase reactions [1,2]. The conformal growth provided by ALD is a direct consequence of the process and ensures precise film thickness control and excellent step coverage, even on 3D structures with large aspect ratios [3,4]. In this context, ALD is quite suitable for the elaboration of complex nanostructured materials, including CNT-inorganic materials heterostructures [5-7] where the CNTs act as the template for depositing inorganic materials. In this way, the final functional material combines the properties of the carbon substrate such as good electrical conductivity, and mechanical and chemical resistance, with the ones of the coating material. Indeed, CNTs have been already combined with a variety of inorganic compounds for applications in energy materials, catalysis, sensing, etc. [6,7].

The nucleation of a metal oxide thin film by ALD onto CNTs requires the chemisorption of a metal precursor on reactive functional groups (e.g. oxygen containing species) at the surface of the CNTs. The density of the reactive functional groups determines the growth mode. For example, it has been demonstrated that island and 2D growth modes could be simply controlled by the degree of surface functionalization of the CNTs, similarly to the critical thickness which set the transition from island to 2D growth mode [8]. However, the surface of pristine CNTs is generally free of oxygenated groups and thus relatively inert to

nucleation in ALD, so a chemical functionalization is needed. This can be achieved *ex situ* by the treatment with a strong acid or *in situ* by the reaction with ozone [5,9]. Unfortunately, chemical covalent functionalization deteriorates the intrinsic electrical, mechanical and structural properties of the pristine nanotubes and needs to be avoided in some applications. Moreover, in the case of supported CNTs the substrate can also be damaged during the process. In fact, most of post-growth chemical treatments are based on strong oxidizing agents and harsh reaction conditions, which generally lead to structural damages on the CNTs, including fracture and formation of oxygenated functional groups [10,11].

A possibility to circumvent such a drawback consists in using N-CNTs as substrate. The doping process of the nanotube with foreign atoms, which is able to create surface defects and break out the chemically inertness of the highly graphitized CNT surface, represents a feasible path to alter their reactivity towards a number of applications [12-14]. Nitrogen-doped carbon nanotubes (N-CNTs) have attracted attention due to the fact that nitrogen doping changes the chemical reactivity and physical properties of the pure CNTs. Furthermore, the nucleation of the ALD film onto the CNTs surface can take place on surface nitrogen species. As a matter of fact, recently, N-CNTs have been coated with metal oxides via ALD of tin oxide and zirconium oxide [15,16]. However, several open questions remain on the nucleation of metal oxides and the chemisorption of the metal oxide precursors onto N-containing surface species.

The possibility to use doped-carbon for ALD is particularly advantageous in the case of vertically aligned CNTs (i.e. CNTs forests). Vertical aligned CNTs (VACNTs) are interesting for numerous applications, especially in CNT-based nanoelectronics, which benefits from the vertical alignment as it provides an electrical path through the nanotube support [17,18]. In this regard, VACNTs have been synthesized by various chemical vapor deposition techniques. Thermal chemical vapor deposition (TCVD) is considered to be the most promising and reliable method for the growth of VACNTs, not only for pure carbon structures [19] but also for heteroatom-doped structures, such as vertically aligned N-CNTs [20,21]. Vertically aligned N-CNTs already presented remarkable properties in electrocatalysis, for example they have shown to be suitable catalysts to reduce or even replace the Pt-based electrodes in their various applications, such as oxygen reduction reaction [22]. Furthermore, the functionalization of VACNTs through the insertion of heteroatoms into the carbon network is undertaken during the TCVD growth, where the desirable alignment is preserved. In this way, the need of additional post-growth chemical treatments, which would greatly affect the CNTs forest and/or the substrate, is avoided. Indeed, a chemical wet treatment could lead to a collapse of the vertical array or their detachment from the substrate [23].

Herein, we report the study of the nucleation and the coating by ALD of vertically aligned N-CNTs grown by TCVD. We focus on the ALD of ZnO because it is a well-established and yet simple chemical process based on hydrolysis-condensation reactions without other side reactions that can further complicate the study of the nucleation and growth onto N-CNTs [15,24-25]. It will be demonstrated that the applied approach allow to

homogeneously coat from the top to the bottom VACNTs without the need of an additional functionalization step. This work open to the possibility to modify CNTs arrays with different metal oxides for applications in the field of energy storage and catalysis while conserving the 3D structure.

III.2. Experimental

III.2.1. Synthesis of N-doped CNTs

Nitrogen-doped CNTs (N-CNTs) were grown by thermal CVD (TCVD) in a quartz-tube furnace reactor. The substrates used for the synthesis of N-CNTs were polished Si (100) wafers coated with 200 nm of thermally grown SiO_2 which had been sequentially coated by 10 nm Al_2O_3 and 10 nm Fe films by physical vapor deposition (RF and DC magnetron sputtering, respectively). Here, the combined oxide layers act as diffusion barriers, avoiding the formation of catalytic inactive iron silicides. In a typical process, N-CNTs were grown by the thermal decomposition of acetylene-ammonia (C_2H_2 (10 sccm)/NH_3 (90 sccm)) mixture as the carbon/nitrogen precursor at 825 °C using argon (Ar (410 sccm)) as a carrier gas. These conditions lead to a content of nitrogen in the CNTs of around 4 at% (see XPS results). More details can be found in our previous work [20]. In order to study the N-doping effect, an undoped CNT sample was also grown under the same conditions but without NH_3 being feed into the chamber during the growth process.

III.2.2. ZnO-N-doped CNTs preparation by ALD

Zinc oxide (ZnO) was deposited on Si wafers (used as reference) and, on as-prepared undoped and N-doped CNT forests using a cross flow home-made ALD reactor working in continuous mode at 100 °C, from diethylzinc (Sigma Aldrich, 95% purity) as metal precursor and deionized water. The precursors were introduced subsequently by ALD pneumatic valves from their reservoirs, which were kept at room temperature. Precursor pulse times of 0.08 s and 0.24 s for diethylzinc (DEZ) and water were used, respectively. 30 s separate the reactants pulses. The delivery lines of the circuit were heated to 100 °C to prevent the precursors from condensation throughout the deposition. Pure N_2, supplied via mass flow controller, was used as a carrier gas at a constant flow of 100 sccm. The typical operating pressures varied from 1.6 to 1.8 Torr during the precursor pulses. The growth per cycle under these conditions determined from the XRR measurement on Si substrates was ~ 0.165 nm. Several samples, with different ZnO thicknesses, were prepared.

III.2.3. Sample characterization

The thicknesses of the as-deposited zinc oxide films on the Si wafer substrates were measured by X-ray reflectivity (XRR) using a Philips X'Pert MRD X-ray diffractometer, with a copper radiation and a graphite monochromator, for the selection of pure Kα radiation. The X-ray tube was operated at 40 kV and 50 mA.

Structural and morphological properties of ZnO/CNT and ZnO/N-CNT heterostructures were characterized by scanning electron microscopy (SEM, Hitachi SU70 microscope), grazing incident X-ray diffraction (GIXRD) technique, using a Rigaku Geigerflex D Max-C Series Diffractometer. The radiation used was Cu Kα (λ=1.5418 Å), with a scan time of 100 s and step size (2θ) of 0.02°. Raman spectroscopy (Jobin Yvon T64000) was carried out at a 532 nm and at a 325 nm excitation wavelength. The samples were also investigated by transmission electron microscopy (TEM) and scanning transmission electron microscopy (STEM) using a Philips CM200 LaB_6 and JEOL JEM-2200FS microscopes, respectively, operated at 200 kV. The samples for TEM and STEM measurements were prepared by dry adhesion of the CNTs to a holey carbon film supported on a copper grid.
To determine the chemical environment and ZnO growth behavior onto N- CNTs, X-ray photoelectron spectroscopy (XPS) was performed in an ultra-high vacuum equipment (Omicron NanoScience) using a non-monochromatic Al Kα (hν= 1486.6 eV) X-ray source, operated at 12.5 kV and 16 mA. The C 1s and N 1s high-resolution spectra were obtained with analyzer pass energy of 20 eV and 40 eV, respectively, and 0.05 eV energy steps. The peak fitting was performed using CasaXPS software. Before the peak fitting, the background was subtracted using a Shirley function. Prior to the measurements, the surface was cleaned by a soft Ar^+ sputter-etching procedure to remove any surface contamination, with a beam energy of 800 eV and sample current of 0.4 μA.

III.3. Results and discussion

The as-prepared N-CNT forests, employed as substrates for the ALD deposition of the ZnO thin films, are densely packed and well aligned with a vertical orientation and an average length of 16 µm (Figure III.1) [20].

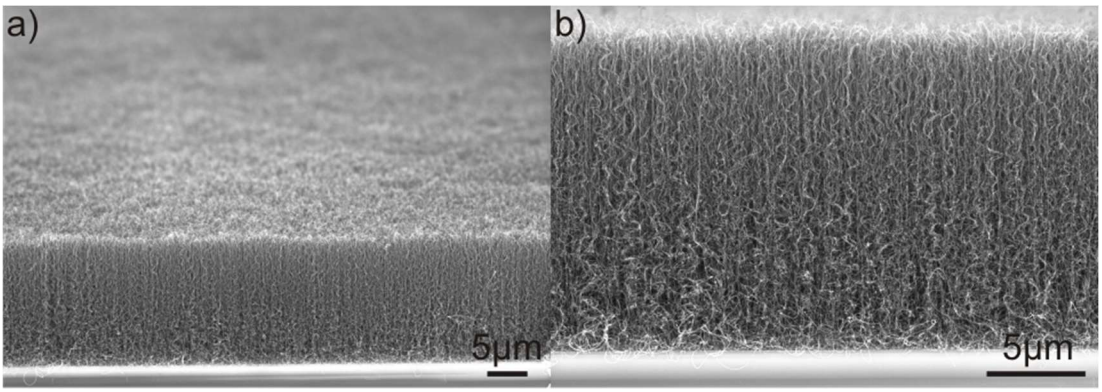

Figure III.1. SEM images of the well-aligned vertically N-CNTs, homogeneously grown on a large area of the silicon substrate. The close-up cross-section image (b) highlights the alignment of the N-CNTs that is an inherent feature of the growth process of forest (from Silva et al. Surf. Appl. Sci. 2015, 344, 57).

According to TEM images of the forests (Figure III.2), all of the nanotubes are multi-walled with a bamboo-like internal structure and present a good degree of crystallinity, as proven by the non-corrugated walls.

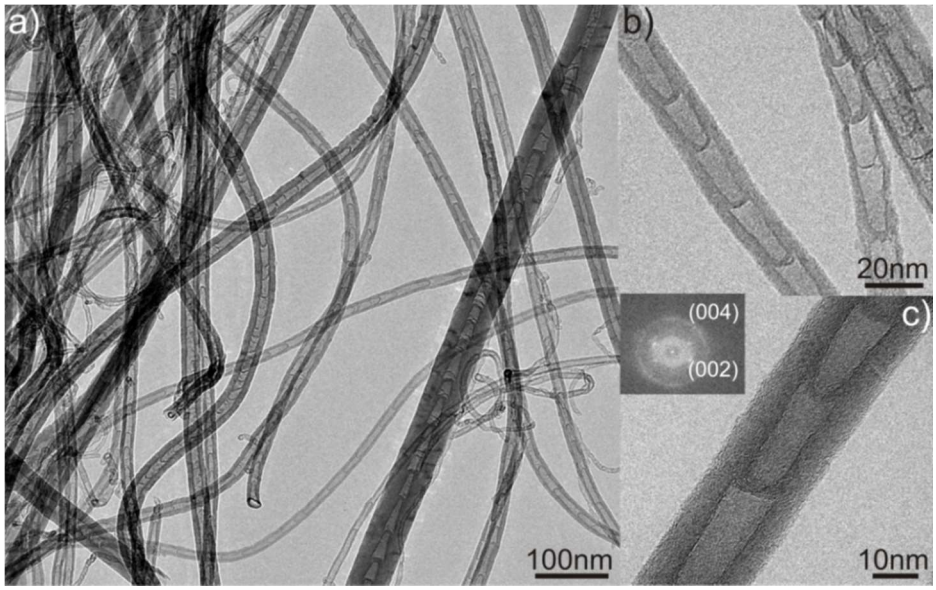

Figure III.2. TEM overview images of the N-CNTs showing their multi-wall nature: (a) taken at low magnification; (b,c) high magnification images showing the bamboo-like internal structure. The ring-like pattern in FFT mode (inset in c) corresponds to the (002) and (004) planes of graphite (from Silva et al. Surf. Appl. Sci. 2015, 344, 57).

Raman spectroscopy was used for comparing the graphitic quality of pristine N-CNTs and undoped CNTs (Figure III.3). Raman spectra of the N-CNTs are very similar to that of the undoped CNTs, indicating that the graphitized structure of CNTs is kept also when in-situ N-doping process is applied. The ratio of the integrated areas of the D and G bands (I_D/I_G) of N-CNTs and undoped CNTs were estimated to be 1.42 and 0.91, respectively, pointing to a higher degree of disorder or defects in the former as result of the N-doping [20].

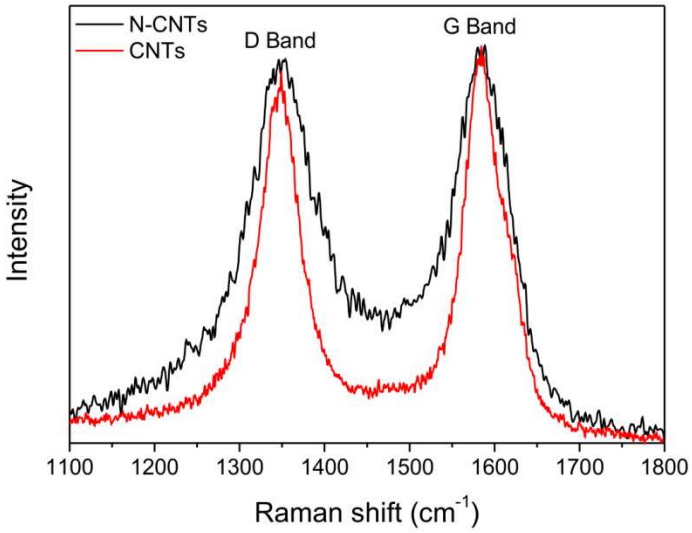

Figure III.3. Raman spectra of N-doped and undoped CNTs acquired with 532 nm excitation wavelength.

A series of ZnO depositions on N-CNT forests were performed using different number of ALD cycles (25, 50, 100 and 200). It is important to note that the vertically aligned CNTs have a higher surface area compared to that expected for CNTs randomly oriented when deposited on a substrate [26]. However, one feature of the vertical alignment is the additional free space between the nanotubes which can facilitate the infiltration of the precursors and the purge of non-reacted precursors and the reaction products. Consequently, this type of architecture can allow an almost CVD-free ALD process.
SEM studies (Figure III.4) revealed a very high degree of ZnO coverage on the N-CNTs after only 50 ALD cycles. The contrast-rich, brighter regions on the surface of the nanotubes correspond to the ZnO deposited either as round particles (*i.e.* after 25 ALD cycles) or as a continuous coating (*i.e.* with 50 ALD cycles or more). Compared to the N-CNTs, the undoped CNTs were only decorated with isolated spherical ZnO particles after 50 cycles (Figure III.4a) instead of a conformal continuous coating as on the N-CNTs (Figure III.4c). This finding can be explained by the low defect density of the undoped CNTs; its almost chemically inert surface has a low amount of active sites for ALD nucleation. Contrarily, N-CNTs, with a higher density of reactive surface species are more favorable to obtain a high nucleation density. Hence, it is most likely that the ZnO particles were selectively nucleated on defective sites or impurities on the nanotube wall.

As a matter of fact, ALD has been already used as an indirect measure of surface defect density and distribution on CNTs and graphene [8,27].

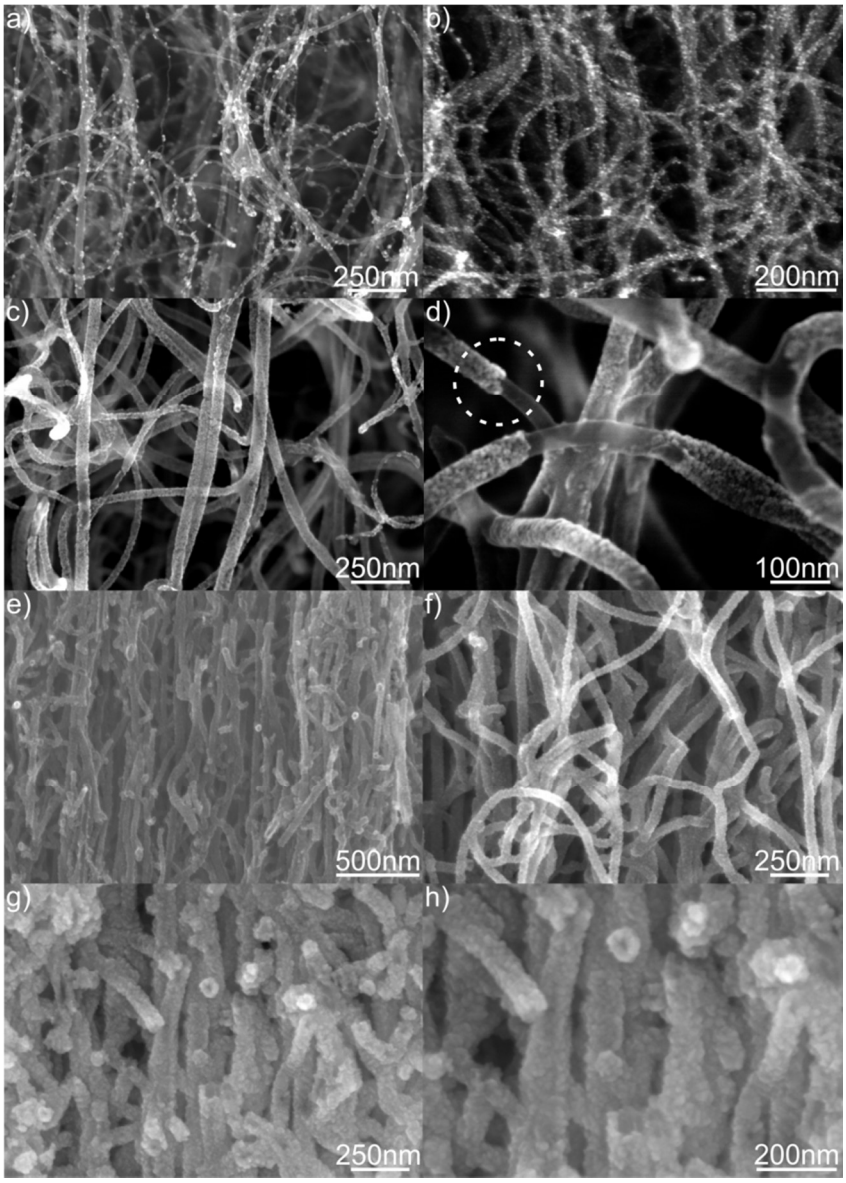

Figure III.4. SEM images of the undoped CNTs after 50 ALD cycles (a) and of vertically aligned N-CNTs coated with ZnO after 25 (b), 50 (c,d), 100 (e,f) and 200 (g,h) ALD cycles. In order to highlight the deposition film, defective regions in the coating are indicated by a dash circle in (d).

The homogeneity of the coating along the whole forest was ascertained by EDS line scan profile taken from the top to the base of the N-CNT array (Figure III.5) revealing almost constant Zn and C signals across the entire length of the N-CNT, supporting that the ZnO coating is indeed uniform along the whole N-CNT forest.

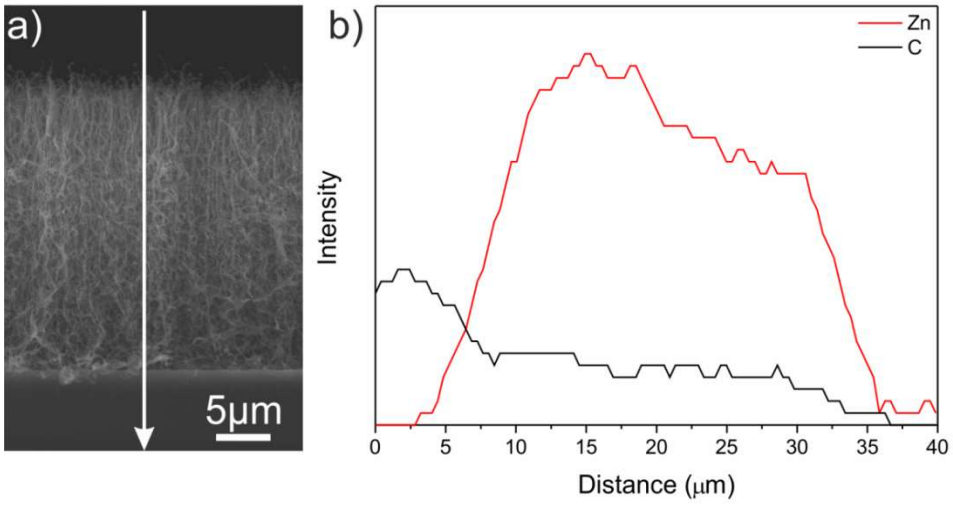

Figure III.5. SEM cross section image of N-CNT forest coated with 50 ZnO ALD cycles (a) and corresponding EDS line scan profile across coated N-CNT forest (b); the white arrow shows the EDS scan region. Qualitatively, the strong signal intensity indicates a high element concentration at the corresponding location. The almost constant Zn and C signals along the whole distance demonstrate that the ZnO coating is uniform across the entire length of the N-CNT forest.

TEM images of coated N-CNTs give further visual evidence of the growth mode evolution as a function of the number of deposition cycles (Figure III.6). Comparing Figure III.6b with c, it can be seen that the surface of N-CNTs is decorated with isolated spherical ZnO particles of a mean diameter of 4 nm after 25 cycles and, with the increase of the ALD cycles these particles begin to coalesce, leading to homogenization of the coating thickness after solely 50 cycles. As a result a conformal coating is achieved with a granular and particulate aspect that can be seen as the dark contrast in the BF-TEM image (Figure III.6c). This morphology is also visible as the bright contrast in the high angle annular DF-STEM image (Figure III.6d). The observed bright contrast regions arise from the heavier (Z-contrast) zinc atoms in ZnO. In this context, the contrast was chosen such that the carbon support remains nearly invisible (as indicated by the white arrows) while the granular coating can be clearly seen. The assignment is in agreement with chemical analysis by EDS elemental mapping (Figure III.7). This sample can be compared to undoped CNTs coated with the same number (50) of ALD cycles in which only spherical and isolated ZnO particles are grown onto the surface of the nanotubes (Figures III.6a). Taking into account that the particles size ranges from 4 nm to 7 nm an average GPC can be roughly estimated to 0.14 nm for the largest particles, which is lower than 0.16 nm obtained from the TEM measurements on the coated N-CNTs. This deviation may originate from the different growth induction time experienced on defects sites of the undoped CNTs, emphasizing the different nature, density and reactivity of defects present in both types of nanotubes. A further increase of the number of ALD cycles originates thicker coatings with its uniformity maintained as depicted in Figure III.6e and f. Additionally, it is possible to observe the transition of island to 2D growth, by controlling

the number of cycles, revealing that the critical thickness needed to obtain a conformal ZnO coating is attained after only 50 cycles, these observations are consistent with the SEM studies.

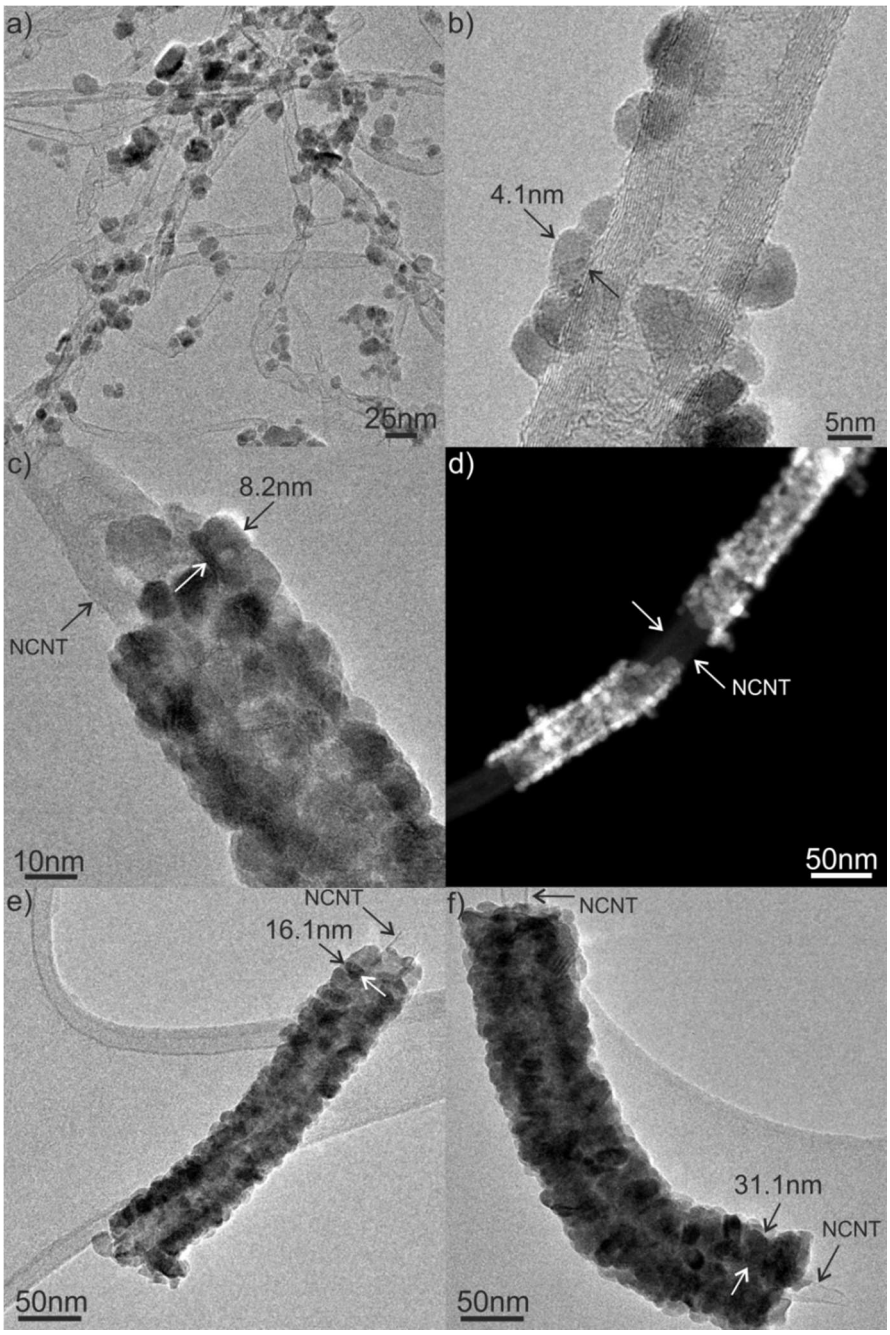

Figure III.6. TEM images of the undoped CNTs after 50 ALD cycles (a) and of N-CNTs coated with ZnO, after 25 (b), 50 (c), 100 (e) and 200 (f) ALD cycles. DF-STEM image recorded from N-CNT coated with 50 ALD cycles (d). The uncoated region (labelled with white arrows) in (d) is due to the manipulation of the sample during the TEM sample preparation.

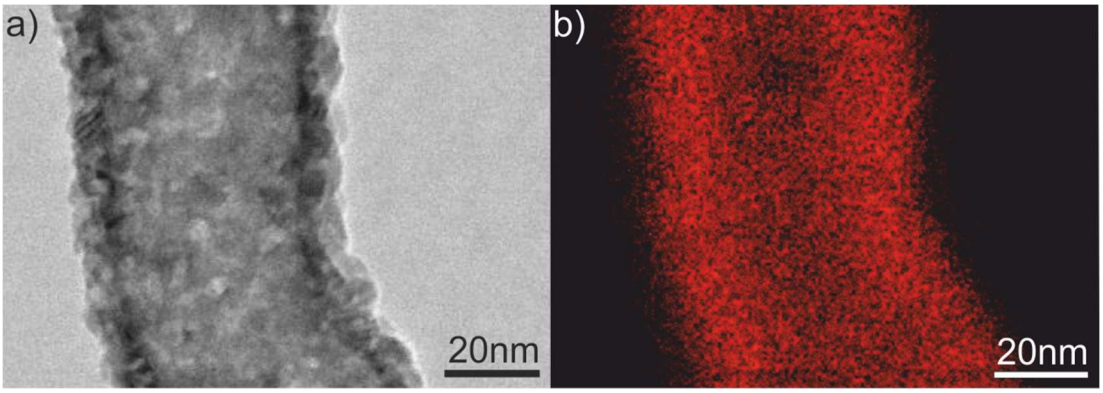

Figure III.7. STEM bright field image in (a) and corresponding elemental map in (b). The EDS map shows the distribution of Zn (color coded red) over the exposed nanotubes.

In parallel to the deposition onto N-CNTs, ZnO ALD films were also deposited onto Si wafer with native SiO_2 in order to establish a relationship between growth behavior (e.g. growth inhibition) on the N-CNTs and Si wafers. On Si wafers the film thickness, calculated from XRR measurements (Figure III.8), increases linearly with the number of ALD cycle (Table III.1).

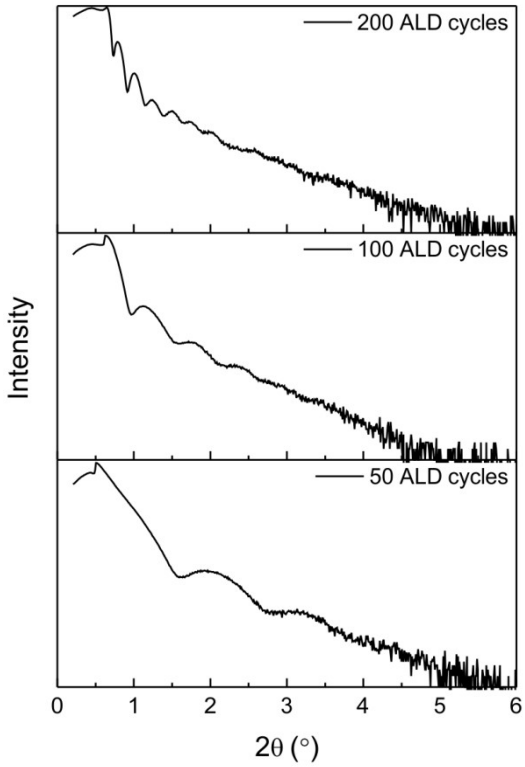

Figure III.8. XRR patterns of ZnO film on a Si wafer after 50, 100 and 200 ALD cycles.

The growth per cycle (GPC) is around ~0.165 nm, which is similar to the GPC reported by other groups [28,29]. Since the ZnO deposition is undertaken simultaneously on an N-CNTs forest and on a Si wafer (used as reference), it enables the comparison of the film

thickness. For example, the thickness of the ZnO film after 50, 100 and 200 ALD cycles, estimated from the TEM images are in good agreement with the expected thickness by considering the number of cycles performed, showing a similar GPC and no evidence of inhibition or delay in nucleation on N-CNTs.

Table III.1. Film thickness of ZnO as a function of ALD cycle number. [a] The average particle size was taken instead of the film thickness.

	Thickness (nm)	
ALD cycle number	Si wafer (XRR measurements)	N-CNTs (TEM measurements)
25	--	4.1[a]
50	8	8.2
75	12.4	--
100	15.5	16.1
200	35.2	31.1

The crystalline structure of the deposited ZnO on the N-CNTs for 50 cycles was identified by GIXRD and Raman techniques and the results are presented in Figure 3. Figure III.9a shows the diffraction pattern of as-deposited ZnO which corresponds to hexagonal wurtzite (from the datasheet JCPDS 36-1451). The reflections are indexed as (100), (002), (101), (102), (110), (103) and (112) and the calculated lattice constants (a = b = 3.2502 Å and c = 5.2224 Å) are in good agreement with the tabulated lattice parameters (in JCPDS 36-1451: a = b = 3.2498 Å and c = 5.22066 Å). The broadening of the peaks in the GIXRD pattern is indicative of the existence of nano crystallites. The crystallite size was estimated with the Scherrer formula and the crystalline size was found to be 4.5 nm after 50 cycles. The peak at 26º present in the patterns corresponds to the (002) plane of the graphite structure of the nanotubes (JCPDS 58-1638). A representative Raman spectrum is shown in Figure III.9b. The bands originating from the uncoated N-CNTs are observed at 1422 and 1582 cm^{-1} (inset of Figure III.9b). Since the Raman spectra were taken with a 325 nm excitation the dispersive D band, usually observed at ~1340 cm^{-1} (under visible excitation) was shifted to higher wavenumbers [30]. The G band centered at 1580 cm^{-1} corresponds to the stretching mode of the C-C bond in the C sp^2 hexagonal plane of graphite. The ZnO A1(LO) first vibration mode is observed at 571 cm^{-1}, with overtones at 1151 and 1719 cm^{-1}.

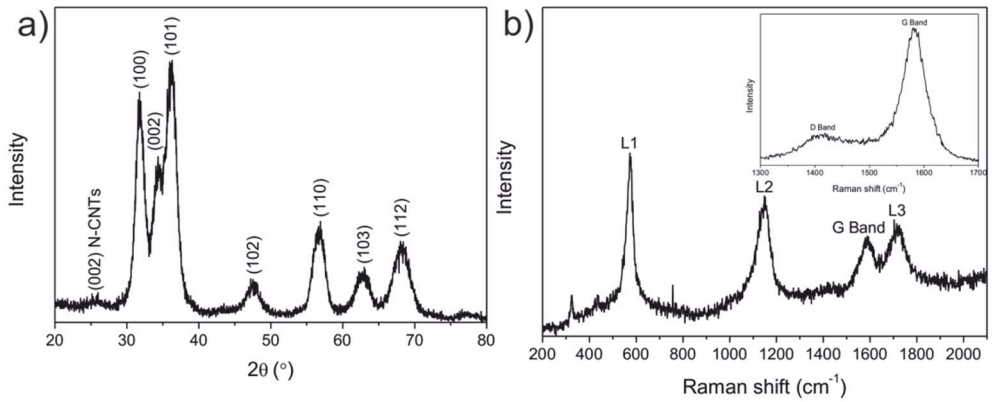

Figure III.9. GIXRD pattern (a) and Raman spectrum (b) of the ZnO deposited on the N-CNTs after 50 ALD cycles. The inset shows the Raman spectrum of the uncoated N-CNTs. The peak observed at 320 cm^{-1} corresponds to an artifact of the system.

To further understand the role of the N-related defects, resulting from the N-doping of the CNTs, on the nucleation and growth of ZnO on the N-CNTs, detailed XPS analysis was performed. The objective was to evaluate if chemical changes were induced on the N-CNTs after ZnO ALD and the nature of the nucleation sites. In comparison to undoped CNTs, the difference of N-CNTs lies in nitrogen doping, resulting in a pristine surface functionalization allowing for the adsorption of the diethyl zinc (DEZ). In N-CNTs three nitrogen bonding configurations can be found: pyridine-like N, pyrrole-like N, and quaternary-like N [31]. The XPS survey spectra obtained for the uncoated N-CNTs and ZnO/N-CNTs nanocomposite are shown in Figure III.10.

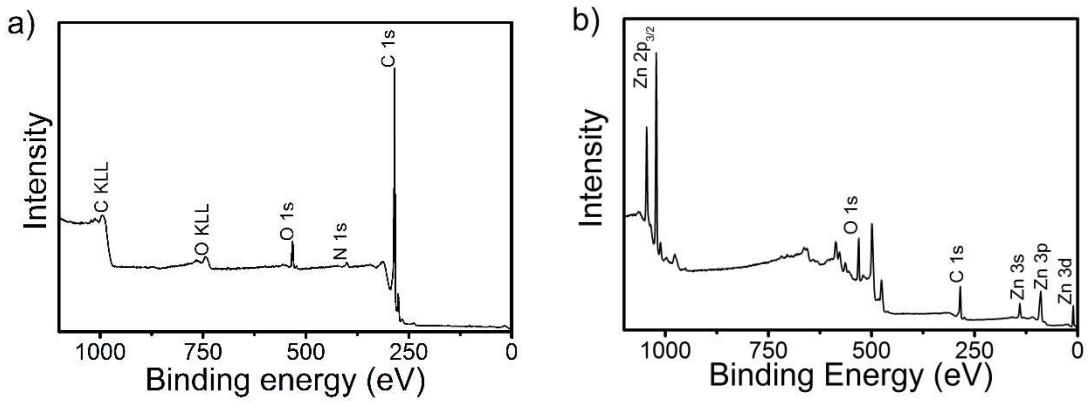

Figure III.10. XPS survey spectrum of the (a) uncoated N-CNTs and (b) N-CNTs/ZnO nanocomposite, after 50 ALD cycles.

Survey XPS spectrum for uncoated N-CNTs shows C (94 at.%), O (2 at.%) and N (4 at.%) elements while the survey XPS spectrum of ZnO/N-CNTs nanocomposite is dominated by strong signals from C, O and Zn photoelectron peaks. Due to the thick ZnO coating the low resolution survey spectrum does not show the N peak. It is worthy to mention that the

samples were cleaned by argon ions sputtering for 2 min, in order to avoid the effects of surface contamination.

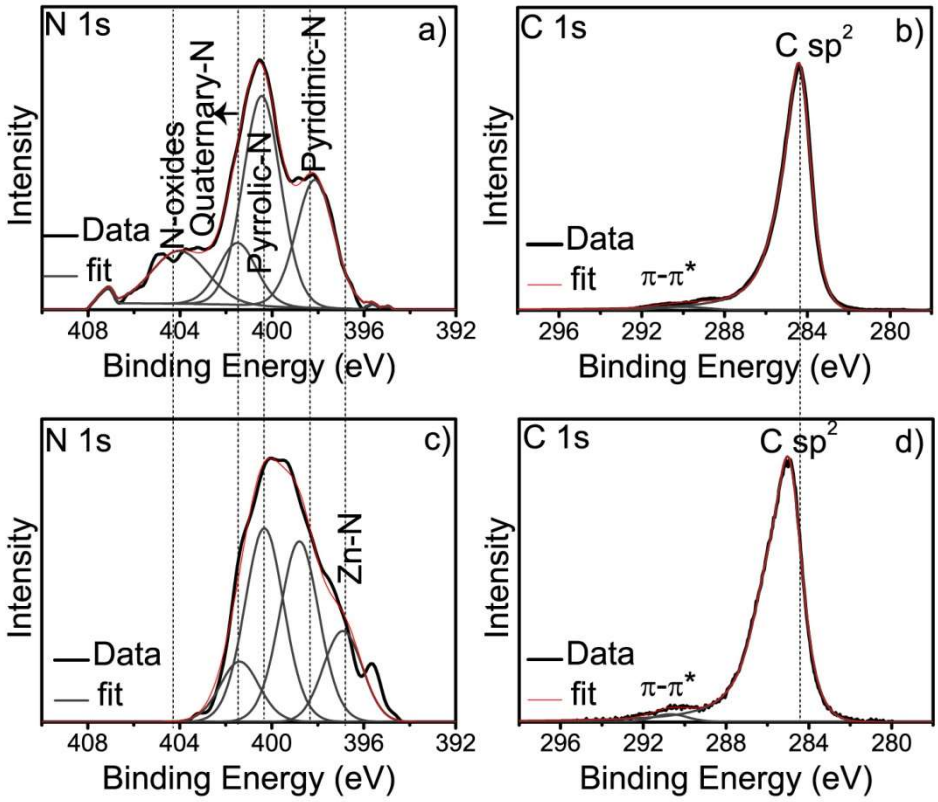

Figure III.11. High-resolution XPS spectra of the uncoated N-CNTs and ZnO coated N-CNTs nanocomposite after 50 ALD cycles: (a) N1s spectrum of uncoated N-CNTs and deconvolution into pyridinic-N (398.2 eV), pyrrolic-N (400.4 eV), quaternary-N (401.5 eV) and adsorbed nitrogen species (404.0 eV), (b) C 1s spectrum of uncoated N-CNTs showing the main peak centered in 284.4 eV, typical of C sp^2 in CNTs with an asymmetrical line shape, and the π-π* shake-up transition, centered in ~291 eV, typical of electrons in delocalized aromatic Csp^2 structures; (c) N1s spectrum of ZnO/N-CNTs nanocomposite and deconvolutions into N-Zn (396.9 eV), pyridinic-N (398.8 eV), pyrrolic-N (400.3 eV), and quaternary-N (401.4 eV); and (d) C1s spectrum of ZnO/ N-CNTs showing the main peak slightly upshifted to 285.0 eV and the π-π* shake-up transition component as uncoated N-CNTs sample.

The C 1s spectrum can be employed to monitor the chemical changes when CNTs are doped with nitrogen. Figure III.11b shows XPS C 1s spectrum for uncoated N-CNTs where the peak has maximum intensity at 284.4 eV, very close (0.1 eV upshift) to the reported value (284.3 eV) for C sp^2 bonding in pristine highly oriented pyrolytic graphite (HOPG), indicating that carbon atoms are almost exclusively C sp^2 hybridized in uncoated N-CNTs sample [32]. The BE is also consistent with previously reported values for P- and N-doped CNTs samples and is in agreement with a small increase of structural disorder from the incorporation of nitrogen within the hexagonal Csp^2 lattice [14,32]. The XPS C 1s spectrum of the N-CNTs/ZnO nanocomposite depicted in Figure III.11d is upshifted and

its maximum appears at 285.0 eV. In order to verify if this shift can be attributed to charging effect caused by ZnO coating, we measured at the same conditions, a ZnO coated undoped-CNT sample. The C1s binding energy recovered was 284.8 eV, proving a charging effect related to the ZnO coating (comparing ZnO/undoped-CNT and ZnO/N-CNTs with N-CNTs sample). Another feature of the line shape of C 1s XPS peaks from CNTs is the presence of a broad feature due to the interaction of the positive core hole with the conduction electrons [14]. This transition is known as π-π* satellite, centered at ~291 eV, and represents the degree of delocalization of electrons in π orbitals [33]. In CNTs, the π-π* shake-up satellite peak is a measure of crystallinity, since defective carbon networks decrease the ability to delocalize electrons [34]. The presence of shake-up satellite peak in both, uncoated N-CNTs and ZnO/N-CNTs nanocomposite, is an indicative that N-doping and ZnO coating preserves the crystallinity of CNTs.

Before ZnO deposition, the N1s XPS spectrum (Figure III.11a) shows a broad signal that can be deconvoluted into four peaks that can be ascribed to the contribution of pyridine-like N (398.2 eV), pyrrolic-N (400.4 eV), quaternary-like N (substitutional) (401.5 eV), and the component in 404.0 eV can be assigned as the nitrogen oxide species or absorbed N_2 [32]. Figure III.11c presents the N1s XPS spectrum of the N-CNTs/ZnO nanocomposite. It shows a broad signal that can be deconvoluted into four components located at 396.9 eV, 398.8 eV, 400.3 eV and 401.4 eV. The component at ~397 eV is assigned to the formation of the Zn-N chemical bond, which indicates that the surface N acts as anchoring site for the nucleation of ZnO. This binding energy can be compared to the assignment given in the literature [35-38]. The disappearance of the 404.5 eV contribution after coating support the assignment of this band to absorbed species [32].
The O 1s XPS spectrum of the N-CNTs/ZnO nanocomposite is reported in Figure III.12a. This spectrum presents an asymmetric shape, indicating that the oxygen exists in two chemical states and it can be deconvoluted into two components with binding energy of 530.0 eV and 531.9 eV, assigned to O-Zn and O-H species. It suggests that, at the low deposition temperature applied (100 °C), the ZnO is not fully condensed and contains a large concentration of hydroxyl groups. This conclusion is supported by a similar line shape of the O1s spectrum of the ZnO deposited on N-CNTs and Si wafers, as shown in Figure III.12b.

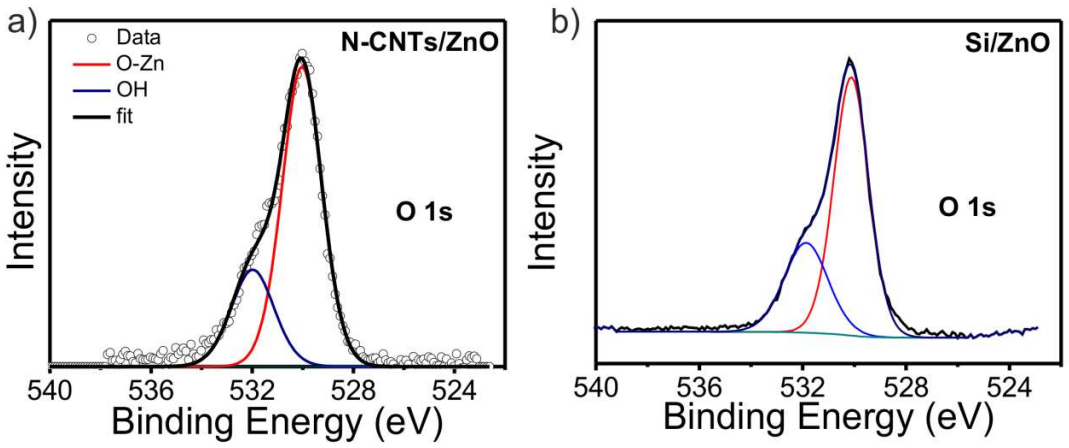

Figure III.12. XPS O 1s spectrum of (a) N-CNTs/ZnO nanocomposite and (b) Si/ZnO thin film. The XPS O 1s spectrum of Si/ZnO was also inserted for comparison purpose.

From the XPS results, it can be concluded that the surface of the N-CNTs provides the proper N-containing nucleation sites for the chemisorption of DEZ allowing to achieve a conformal ZnO coating along the vertically aligned nanotubes.

III.4. Conclusions

The present work reports a strategy to directly coat vertically aligned carbon nanotubes with ZnO by ALD without pretreatment for the conformal coating of graphitized carbon nanostructures. A uniform growth was achieved along the entire length of the vertically aligned N-CNTs from the top to the bottom of the forest. The same ALD process on planar Si substrates gave similar thicknesses independently on the number of ALD cycles, suggesting no significant nucleation barrier for the ALD process on the N-CNT surfaces. The required anchoring sites for the nucleation of ZnO are provided by nitrogen species introduced during the growth of the CNTs. A critical thickness of 8 nm (reached after 50 ALD cycles) is needed in order to obtain continuous and conformal ZnO coatings. On the other hand, when undoped CNTs were employed, due to the low defect density and chemically inert nature they exhibit only very few sites for ALD nucleation, which results in an inhomogeneous decoration with isolated spherical ZnO particles. The pristine surface functionalization promotes chemisorption of the precursors and allow for the ZnO nucleation. Indeed, DEZ chemisorbs on N-containing surface species and lead to the formation of Zn-N bonds. These observations highlight the importance of the N surface species towards ZnO ALD. In order to achieve a similar quality of coating on undoped CNTs a chemical functionalization with strong acids would have been needed which could destroy the morphology of the CNTs forest and perturbed the electronic properties and crystalline structure of the pristine CNTs.

All in all, the ability to uniformly coat N-CNTs with ZnO by ALD can be extended to other metal oxides, and it will allow obtaining vertically aligned 1D nanostructures having new functionalities, while maintaining their original electronic properties and crystalline structure of the support.

References

[1] R.L. Puurunen, *J. Appl. Phys.* **2005**, *97*, 121301.

[2] M. George, *Chem. Rev.* **2010**, *110*, 111.

[3] M. Knez, K. Nielsch, L. Niinistö, *Adv. Mater.* **2007**, *19*, 3425.

[4] C. Marichy, M. Bechelany, N. Pinna, *Adv. Mater.* **2012**, *24*, 1017.

[5] C. Marichy, N. Pinna, *Coord. Chem. Rev.* **2013**, *257*, 3232.

[6] D. Eder, *Chem. Rev.* **2010**, *110*, 111.

[7] M. Melchionna, S. Marchesan, M. Prato, P. Fornasiero, *Catal. Sci. Technol*. **2015**, 5, 3859.

[8] C. Marichy, J.P. Tessonnier, M.C. Ferro, K.H. Lee, R. Schlögl, N. Pinna, M.G. Willinger, *J. Mater. Chem.* **2012**, 22, 7323.

[9] X. Tong, X. Guo, O. Moutanabbir, X. Ao, E. Pippel, L. Zhang, M. Knez, *Small* **2012**, *8*, 3390.

[10] M.W. Marshall, S. Popa-Nita, J.G. Shapter, *Carbon* **2006**, *44*, 1137.

[11] E. Shulga, K. Pohako, A. Treshchalov, U. Joost, V. Kisand, I. Kink, *Micro Nano Lett.* **2011**, *6*, 704.

[12] E.L. Hooijdonk, C. Bittencourt, R. Snyders, J.F. Colomer, *Beilstein J. Nanotechnol.* **2013**, *4*, 129.

[13] J. Li, G.P. Pandey, *Annu. Rev. Phys. Chem.* **2015**, *66*, 331.

[14] J.R. Araujo, A.M. Silva, C.P. Gouvêa, E.S. Lopes, R.A.A. Santos, L. A. Terrazos, R.B. Capaz, C.A. Achete, *Carbon* **2016**, *99*, 1.

[15] X. Meng, Y. Zhong, Y. Sun, M. N. Banis, R. Li, X. Sun, *Carbon* **2011**, *49*, 1133.

[16] J. Liu, X. Meng, M.N. Banis, M. Cai, R. Li, X. Sun, *J. Phys. Chem. C* **2012**, *116*, 14656.

[17] W.B. Choi, E. Bae, D. Kang, S. Chae, B. Cheong, J. Ko, E. Lee, W. Park, *Nanotechnology* **2004**, *15*, 512.

[18] Y. Che, H. Chen, H. Gui, J. Liu, C. Zhou, *Semicond. Sci. Technol.* **2014**, *29*, 073001.

[19] D. Mata, R.M. Silva, A.J.S. Fernandes, F.J. Oliveira, P.M.F.J. Costa, R.F. Silva, *Carbon* **2012**, *50*, 3585.

[20] R.M. Silva, A.J.S. Fernandes, M.C. Ferro, N. Pinna, R.F. Silva, *Appl. Surf. Sci.* **2015**, *344*, 57.

[21] T. Thurakitseree, C. Kramberger, P. Zhao, S. Aikawa, S. Harish, S. Chiashi, E. Einarsson, S. Maruyama, *Carbon* **2012**, *50*, 2635.

[22] K. Gong, F. Du, Z. Xia, M. Durstock, L. Dai, *Science* **2009**, *323*, 760.

[23] K.L. Stano, M. Carroll, R. Padbury, M. McCord, J.S. Jur, P.D. Bradford, *ACS Appl. Mater. Interfaces* **2014**, *6*, 19135.

[24] G. Clavel, C. Marichy, N. Pinna, in *Atomic Layer Deposition of Nanostructured Materials* (eds. N. Pinna and M. Knez), Wiley-VCH, **2011**, 61.

[25] G. Clavel, E. Rauwel, M.G. Willinger, N. Pinna, *J. Mater. Chem.* **2009**, *19*, 454.

[26] N. Yazdani, V. Chawla, E. Edwards, V. Wood, H.G. Park, I. Utke, *Beilstein J. Nanotechnol.* **2014**, *5*, 234.

[27] K. Kim, H.B.R. Lee, R.W. Johnson, J.T. Tanskanen, N. Liu, M.G. Kim, C. Pang, C. Ahn, S.F. Bent, Z. Bao, *Nat. Commun.* **2014**, *5*, 4781.

[28] X.L. Li, C. Li, Y. Zhang, D.P. Chu, W.I. Milne, H.J. Fan, *Nanoscale Res. Lett.* **2010**, *5*, 1836.

[29] T. Tynell, M. Karppinen, *Semicond. Sci. Technol.* **2014**, *29*, 043001.

[30] H.B. Zhang, G.D. Lin, Z.H. Zhou, X. Dong, T. Cheng, *Carbon* **2002**, *40*, 2429.

[31] P. Ayala, R. Arenal, M. Rümmeli, A. Rubio, T. Pichler, *Carbon* **2010**, *48*, 575.

[32] S. Maldonado, S. Morin, K.J. Stevenson, *Carbon* **2006**, *44*, 1429.

[33] D.Q. Yang, E. Sacher, *Surf. Sci.* **2002**, *504*, 125-137.

[34] H.E. Szwarckopf, *Carbon* **2004**, *42*, 1713.

[35] K. Toyoura, H. Tsujimura, T. Goto, K. Hachiya, R. Hagiwara, Y. Ito, *Thin Solid Films* **2005**, *49*, 288.

[36] M. Petravic, P.N.K. Deenapanray, V.A. Coleman, C. Jagadish, K.J. Kim, K. Koike, S. Sasa, M. Inoue, M. Yano, *Surf. Sci*. **2006**, *600*, 81.

[37] A. Ievtushenco, O. Khyzhun, I. Shtepliuk, V. Tkach, V. Lazorenko, G. Lashkarev, *Acta Phys. Pol. A* **2013**, *124*, 858-861.

[38] C.L. Perkins, S.H. Lee, X. Li, S.E. Asher, T.J. Coutts, *J. Appl. Phys.* **2005**, *97*, 034907.

Chapter IV

Chapter preface

This chapter describes an engineering process to homogeneously growth vertically aligned carbon nanotubes (VACNTs) arrays directly on a metallic substrate (Inconel®600), where the metallic substrate plays two key features: (i) Inconel®600 itself provide catalytic active sites for the nanotubes growth process and (ii) acts as a current collector. This approach leads to a breakthrough towards the preparation of binder-free carbon-based electrodes. The present contents were published as:

"Catalyst-free growth of carbon nanotube arrays directly on Inconel® substrates for electrochemical carbon-based electrodes"

R.M. Silva, A.C. Bastos, F.J. Oliveira, D.E. Conte, Y. Fan, N. Pinna, R.F. Silva, *J. Mater. Chem. A* **2015**, *3*, 17804-17810.

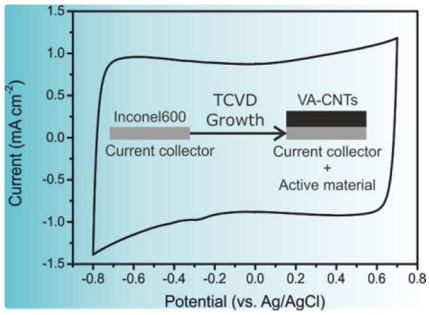

This manuscript received the contributions from F.J. Oliveira, A.C. Bastos, D.E. Conte and Y. Fan in terms of electron microscopy and electrochemical measurements and interpretation, respectively.

Catalyst-free growth of carbon nanotube arrays directly on Inconel® substrates for electrochemical carbon-based electrodes

Abstract

Vertically aligned carbon nanotubes (VACNTs) were grown directly on a pretreated Inconel®600 metallic substrate by thermal chemical vapor deposition without the need of catalyst addition. This experimental approach allows the substrate surface to act as both the catalyst and support for the CNTs growth therefore enhancing the connection between the two. It was found that uniformly dispersed and densely packed nano-sized, intrinsic catalytic particles, generated during the annealing pretreatment, allow the growth of the vertically aligned CNTs. Scanning electron microscopy, transmission electron microscopy and Raman spectroscopy were used to assess the quality and the nature of the formed CNTs. Electrochemical measurements were performed to evaluate the possibility to use the Inconel/VACNTs system as an electrode material. As a proof of concept, the capacitive behavior of the VACNTs arrays coupled to the Inconel substrate as the active electrode material and the current collector, respectively, in supercapacitors is demonstrated.

IV.1. Introduction

Direct growth of vertically-aligned carbon nanotubes (VACNTs) on metallic substrates is of great interest for applications such as high surface area electrodes for sensors, electrochemical capacitors and lithium-ion batteries [1,2]. Moreover, it is of utmost importance to have VACNTs directly grown on metallic current collectors. This strategy enables the elaboration of binder-free electrodes and the formation of robust CNT-metal contacts during the growth. In this context, one-step electrode preparation is more attractive and powerful than the transfer technique consisting in, firstly, detaching the VACNTs from the original substrate and then, depositing them onto the conductive substrates with the help of binders to fabricate VACNTs electrodes [3]. As a matter of fact, the use of binders may occlude the surface of the nanotubes which could affect their electrochemical properties, stressing out the necessity to growth VACNTs directly on the metallic current collector. Among the several metallic alloys, Inconel®600 (Inconel) has been used as a conductive substrate to growth aligned nanotubes by vapor-phase catalyst delivery method [1,4-6]. This Ni-based superalloy is a standard engineering material for applications that require resistance to corrosion and heat.

CNT growth by thermal chemical vapor deposition (TCVD) is a widely applied synthesis technique for the production of CNTs. In the available literature, the TCVD growth of VACNTs is reported for insulating and nonmetallic substrates, such as alumina and silicon oxide, coated with a thin film catalyst (e.g. Fe). This approach can be seen as a two-stage process: (i) the restructuring of the catalyst thin film into catalytically active nano-sized particles (e.g. by annealing under a reductive atmosphere) and (ii) graphitic network

formation and CNT growth from a carbon feedstock [7]. For example, this approach permitted to growth VACNTs on Al_2O_3-buffered superalloy Inconel 718 coated with a catalytic Fe film by e-beam evaporation, following the same approach used for insulating substrates [8].

The direct growth of CNTs on metallic substrates by TCVD without a prior ex-situ deposition of a catalyst (e.g. transition metals such as Fe, Ni or Co) and oxide buffer layer (e.g. Al_2O_3) or by assisting the process via vapor-phase delivering of the catalyst has proven to be very challenging [9]. The process would rely on the in-situ formation of nano-sized catalyst particles onto the Inconel surface. For example, Yi et al. [9] used plasma enhanced hot filament CVD technique to grow VACNTs on oxidized Inconel 600 plates without addition of catalyst, evidencing that the Inconel itself can provide catalytic active sites for CNTs growth and their alignment mechanism has also been proposed [10].

In this work, we demonstrate that VACNTs can be successfully grown directly on polished and heat treated Inconel substrate by the TCVD technique, without the addition of external catalyst. This simpler approach was optimized to accomplish the growth of VACNTs as a uniform and dense layer on the metallic substrate. In order to prove the good electric contact between the substrate and the carbon nanotubes and its good electrical properties, the VACNTs array coupled to the Inconel was directly used as an electrode material in supercapacitors operating in aqueous Na_2SO_4 electrolyte.

IV.2. Experimental

IV.2.1. Sample preparation

A 15 x 15 cm^2 Inconel®600 (main composition: Ni-72 wt.%, Cr-16 wt.%, Fe-8wt.%) sheet with a thickness of 0.1 mm was purchased from Goodfellow and subsequently cut into 1 x 1 cm^2 size samples. These were mechanically polished with SiC grinding paper (grit 4000), cleaned with ethanol and dried with N_2. The Inconel substrates were placed in a quartz boat and inserted into the TCVD furnace for a heat treatment of 45s at 850 ºC in air to oxidize the surface [5].

IV.2.2 Growth of VACNTs on Inconel substrates

The VACNT arrays were grown by TCVD technique in a furnace consisting of an horizontal mounted quartz tube (diameter ~ 5cm) coupled to a thermal heater, equipped with various gas lines and standard mass flow controllers to regulate the flow of carbon source (acetylene ≥ 99.6%), reducing gas (hydrogen ≥ 99.999%) and inert gas (argon ≥ 99.999%). More details of the CVD set-up are given elsewhere [7].

The reactor was evacuated to 3.0 x 10^{-3} mbar with a rotary pump and subsequently filled with Ar up to atmospheric pressure. Substrates were placed in a region of the furnace were the temperature is 650 ºC, under a flow of Ar (1000 sccm) for 5 minutes, followed by a pretreatment in a reductive flow of H_2 (500 sccm) and Ar (100 sccm) for 1 minute (i.e. annealing step). Immediately after, C_2H_2 (10 sccm), H_2 (100 sccm) and Ar (400 sccm)

were introduced for 15 minutes. The gas flows were stopped and the samples removed from the furnace and cooled down to room temperature.

IV.2.3 Sample characterization

Scanning electron microscopy (SEM) was performed with a Hitachi SU-70 microscope operated in secondary electron mode at 15 kV equipped with energy dispersive X-ray spectroscopy (EDS). A polished and heat treated Inconel substrate was cut into ~0.5 x 1 cm^2 slices for SEM cross-section observation. Since the Inconel substrates do not remain flat after cutting, samples were sandwiched between two pieces of Si wafer by means of a thermally activated two component epoxy resin. A hot-mounting press metallographic preparation was then carried out for the polishing procedure of the Inconel/Si interface by a sequence of SiC grinding papers finalized by colloidal silica. The Inconel substrate top surfaces were also characterized by grazing incident X-ray diffraction (XRD) technique using a Rigaku Geigerflex D Max-C Series Diffractometer equipped with Cu Kα radiation (λ=1.5418 Å). The scan time and step size were of 100 s and 0.02 2θ° respectively, with the sample mounted in the thin film geometry arrangement. Glow Discharge Optical Emission Spectroscopy (GDOES) technique using a Jobin Yvon HORIBA GD Profiler was employed in order to obtain the elemental depth profile from the Inconel substrate surface. A 3D surface optical profiler (Sensofar S NEOX) was used for the measurement of the VACNTs height. Cross sections of the VACNTs were also observed by SEM, with 45º tilting, after removing them from the substrate surface. Transmission electron microscopy (TEM) measurements as well the selected area electron diffraction (SAED) on the CNTs was carried out on a JEOL JEM-2200FS or on a Philips CM200 LaB_6 microscopes operated at 200 kV. Samples for TEM observations were prepared by deposition a drop of a diluted ethanol dispersion of the CNTs (previously sonicated for a few seconds) on a holey carbon grid; the solvent was allowed to dry in air. Raman spectroscopy (Jobin Yvon T64000) was carried out at a 532 nm excitation wavelength on the as-grown VACNTs in order to evaluate their quality in terms of amorphous carbon content. The electrochemical measurements were performed using a Bio-Logic VMP3 Potentiostat-Galvanostat (Science Instruments). The experiments were conducted in a three-electrode electrochemical set-up, where the CNTs/Inconel was used as the working electrode, with platinum foil as the counter electrode and a standard silver/silver chloride electrode (Ag/AgCl) as the reference electrode. The electrolyte (1M Na_2SO_4) was prepared from Na_2SO_4 (Sigma Aldrich, 99.0%) and Millipore water. The solution was degassed with Ar before and during the measurements. The electrochemical impedance spectroscopy (EIS) studies were carried out in the frequency region from 0.01 to 100,000 Hz with the test signal amplitude of 5 mV. It is worth pointing out that the area normalized capacitance (mF cm^{-2}) was applied for the assessment of the electrochemical performance because the mass of the CNTs array is small and therefore its accurate measurement is not straightforward. This was the main reason to use the footprint area of the electrode. However, for comparison purpose the height of the CNTs array is also given.

IV.3. Results and discussion

IV.3.1. Surface features of Inconel®600 substrates

The SEM images in Figure IV.1 reveal the surface features of the Inconel®600 as received (a) and polished (b), prior the heat treatment in air.

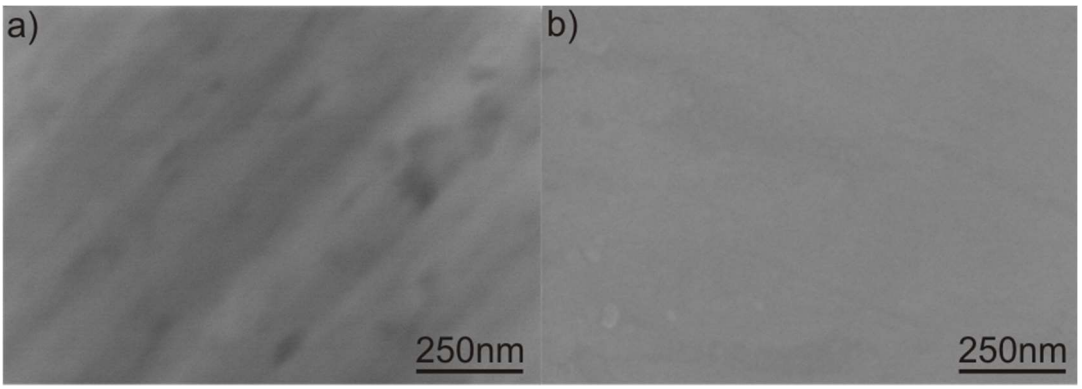

Figure IV.1. High magnification SEM Inconel®600 surface images of as received (a) and polished (b). The Inconel surface after the polishing procedure clearly appears smoother and featureless.

The XRD patterns of the as-received and the heat-treated surfaces of the Inconel substrate are shown in Figure IV.2. The XRD pattern of the as-received surface only reveals the presence of nickel, the main constituent of Inconel®600. After the heat treatment, the emergence of hematite (Fe_2O_3, JCPDS #01-088-2359) and iron-nickel alloy ($Fe_{0.916}Ni_{0.084}$, JCPDS #01-081-8233) can be observed.

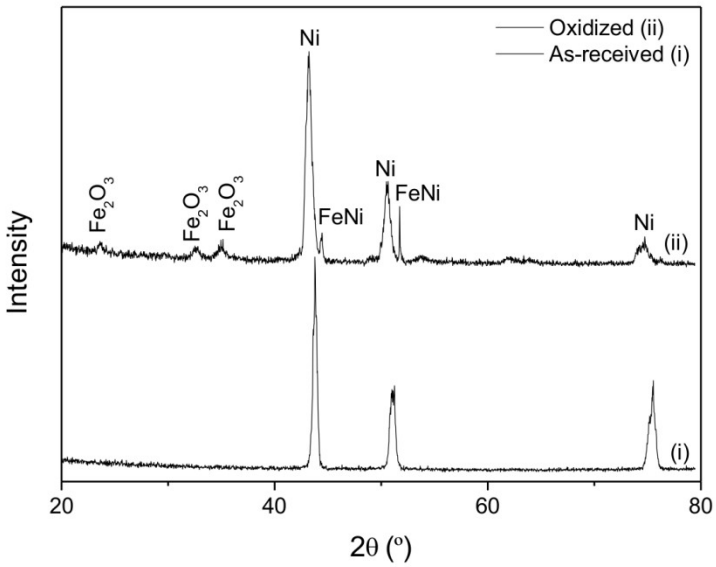

Figure IV.2. XRD patterns of the as received (i) and polished/heat-treated (ii) surfaces of the Inconel substrate.

The surface of the heat-treated Inconel substrate under an SEM is shown in Figure IV.3a revealing a granular morphology. This appearance is totally distinct from that of the Inconel substrates, prior to the heat treatment, as presented in Figure IV.1, where SEM micrographs of the bare (Figure IV.1a) and polished surfaces (Figure IV.1b) are presented. Figure IV.3b shows the SEM cross section image through the Si-resin-Inconel assembly. Three different regions are distinctly observed: I and II are clearly modified microstructures probably resulting from the oxidation treatment of the Inconel alloy whose bare microstructure is shown in region III, this finding is also supported by the Figure IV.4.

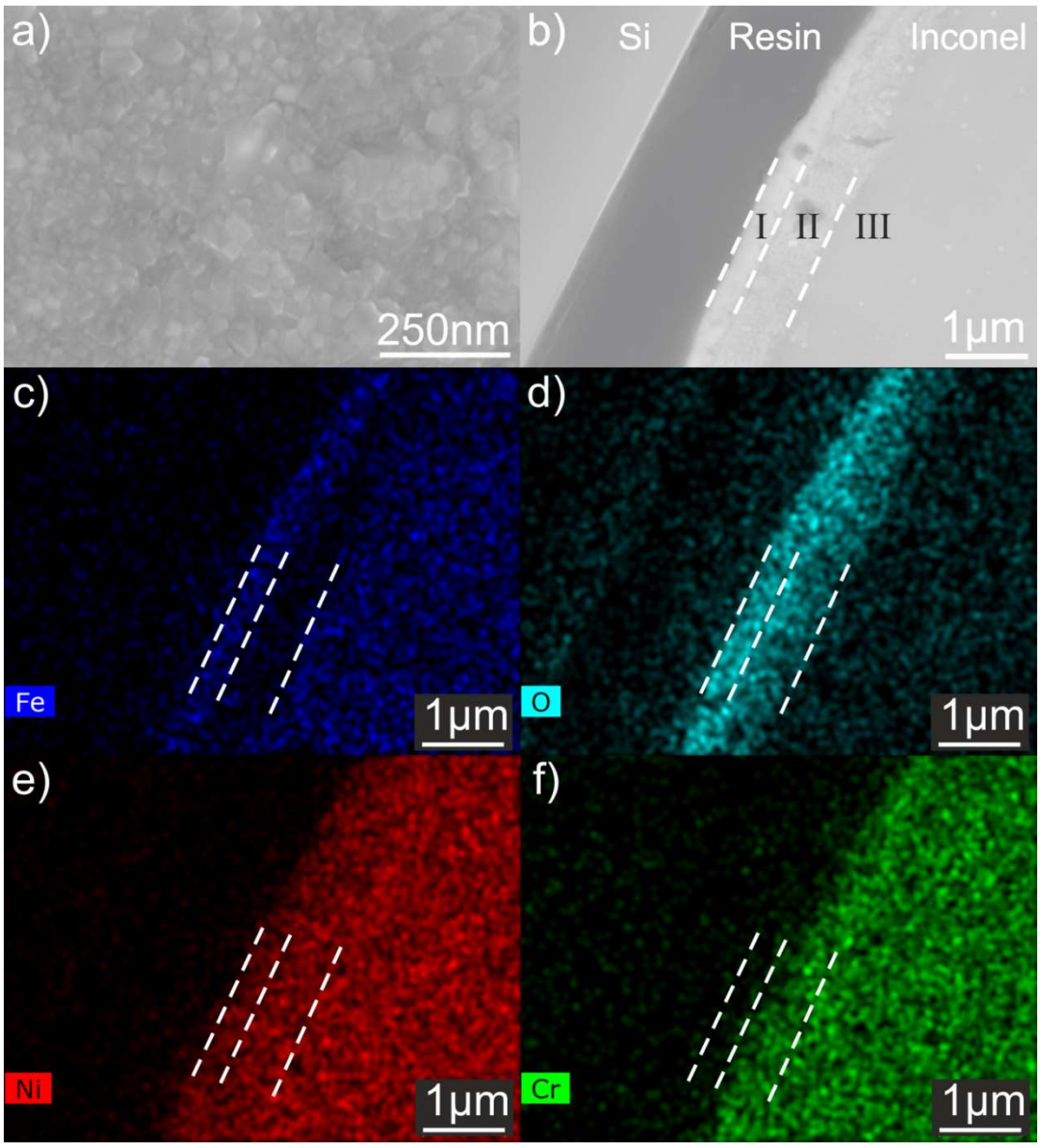

Figure IV3. SEM images of the heat treated Inconel substrate: top view (a) and cross-sectional view (b). The elemental map reveals the presence of iron (c), oxygen (d), nickel (e) and chromium (f).

In order to elucidate the nature of such regions, EDS elemental mapping of iron (Fe), oxygen (O), nickel (Ni) and chromium (Cr) was performed, (Figures IV.3c to f). The most evident elemental features are: i) the oxygen-enriched surface in agreement with the XRD data (Figure IV.2); ii) an outermost layer, region I, with a high concentration of iron and a visible chromium depletion; iii) a subsurface, region II, with exactly the opposite property, i.e. lack of iron and chromium enrichment; iv) the variation in the nickel content through regions I and II is not significant, as this metal is the major component of the Inconel® alloy.

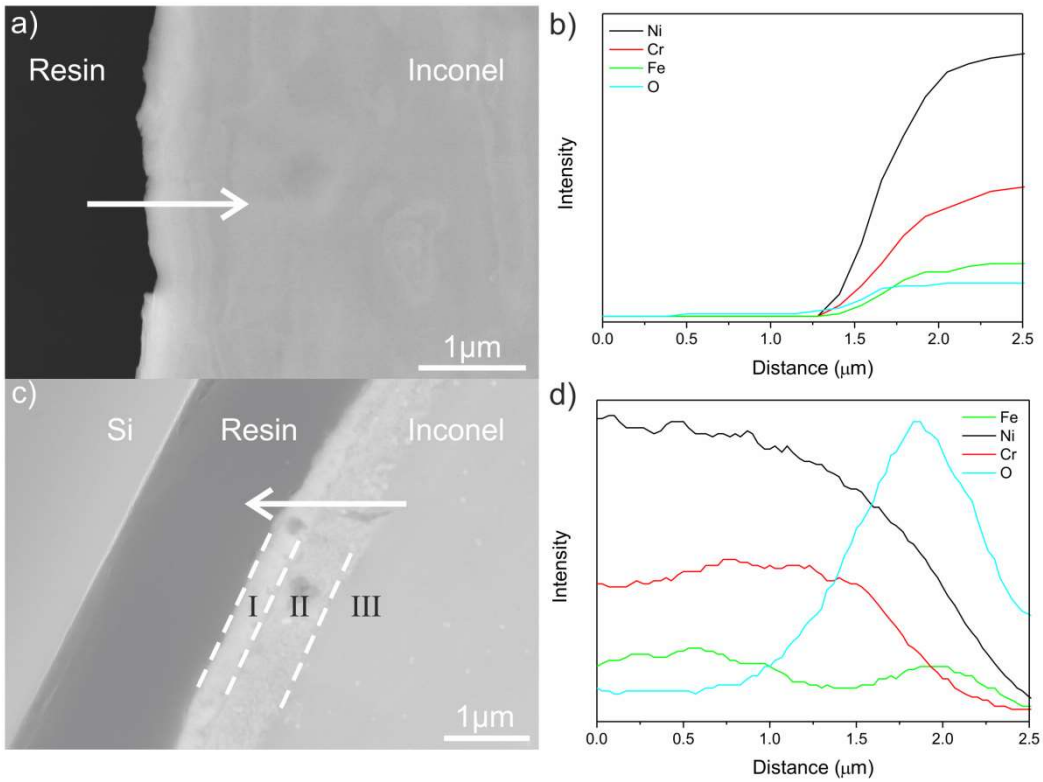

Figure IV.4. SEM cross section image (a) and corresponding EDS line scan profile (b) of the Inconel substrate before the heat treatment showing the elemental composition of the Inconel along the white scan line. The strong Ni signal and weak Fe signal support that the outermost surface is namely composed by Ni. The SEM cross image (c) and corresponding EDS line scan profile (d) of the Inconel substrate after the heat treatment were also inserted for comparison purpose.

The GDOES elemental depth profile shown in Figure IV.5 provides more information about this layered structure to support the above statements. The profile reveals that oxygen presents a decreasing gradient of concentration from the surface, with a very high GDOES intensity at the outermost layer that corresponds to region I in Figure IV.3b. Moreover, GDOES data confirm the enrichment in Fe occurring in region I but points out to a similar phenomenon also occurring to the Ni component. The subsurface corresponding to region II is almost only composed by Cr, whose intensity remains

constant for a certain depth, besides oxygen. For higher sputtering times, the metallic constituents of Inconel appear with concentrations similar to their nominal values.

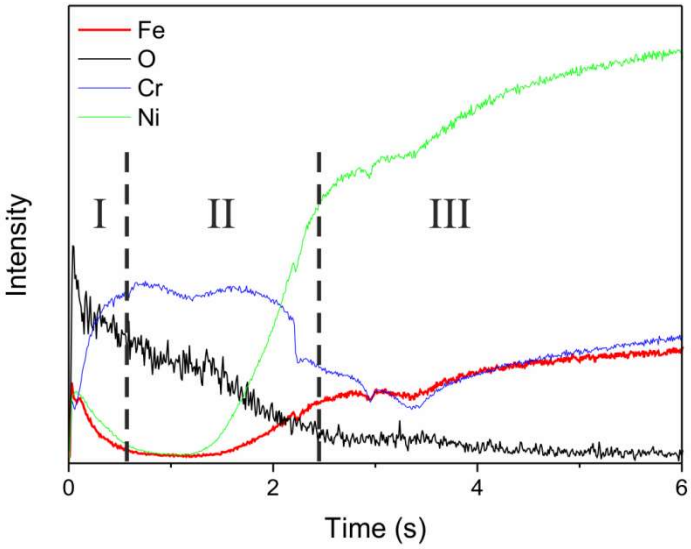

Figure IV.5. GDOES elemental depth profile for oxidized Inconel.

The combination of XRD data, EDS elemental mapping and GDOES depth profile analysis allows to conclude that during the oxidation pretreatment Fe is preferentially segregated to the outer layer (region I) forming Fe_2O_3 while Cr remains in the adjacent subsurface region II. Ni associates to Fe diffusion to the surface. Even though Inconel is an alloy where a chromium oxide (Cr_2O_3) passivation barrier is formed upon air exposure at elevated temperatures (e.g. 850 ºC) [5], the XRD pattern does not show the presence of this oxide on the outer layer. In fact, a continuous Cr_2O_3 layer is formed underneath of the other oxides, uplifting them to the outer region. These observations are in agreement with recent oxidation studies on Inconel®600 that showed that inward oxygen diffusion promoted the formation of a Cr_2O_3 inner type layer, whereas Ni ions move outward [11]. Earlier studies highlighted the importance of the relative rates of diffusion of elements from the bulk alloy to explain the formation of different oxide layers, in opposition to free-energy considerations (that would favor oxidation in the order Cr>Fe>Ni) and availability of metal (that would promote the oxidation order Ni>Cr>Fe) [12].

IV.3.2. Growth of VACNTs on Inconel®600 substrate

It is well-known that the VACNTs growth depends on the formation of nano-sized metal catalyst particles on the substrate surface [7,13], as schematically illustrated in Figure IV.6a. Hence, the granular morphology produced after heat treatment (Figure IV.3a) together with its iron oxide chemical nature (Figures IV.2, IV.3c and IV.5), appears as an ideal combination for the in-situ direct growth on Inconel provided a reduction treatment is

undertaken. This was the reason for the shorter annealing step (1 min) in a reductive mixture flow of H_2 and Ar that resulted in the surface morphology presented in Figure IV.6b, since longer annealing time leads to the agglomeration of the small nano-sized particles into larger ones. As a result, an even distribution of nano-sized particles with pseudo-spherical morphology is obtained, demonstrating that the grains were restructured to a smaller size constituting ideal catalytic active sites for the CNTs growth. In fact, they promote the adsorption and dissociation of the carbon source (i.e., C_2H_2) on their surfaces, and the dissolution and further precipitation of the carbon atoms, leading to the growth of a CNT [13].

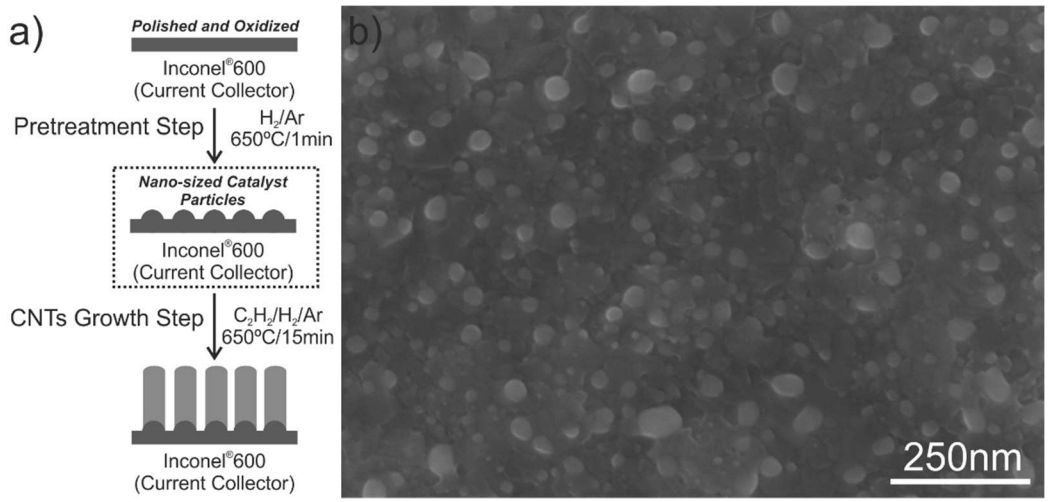

Figure IV.6. Schematic illustration of the CNTs growth process (drawing not to scale) (a).SEM image of the Inconel®600 surface before the CNTs growth step (b).

The high number of nucleation sites leads to a high density of CNTs grown over the substrate, as shown in Figures IV.7a and b. The vertical alignment with respect to the substrate is depicted from images in Figures IV.7c and d. This alignment results from the sufficient density of growing CNTs that causes surface crowding constraining a preferentially unidirectional growth. This means that, as CNTs begin to grow form the densely distributed nano-sized catalyst particles, it is generally accepted that van der Waals forces among CNT neighbors cause them to all grow vertically to the substrate [14]. The final height of the VACNTs after 15 min of growth was observed to be around 18 μm by 3D optical profilometry measurement, denoting a higher growth rate than that attained by hot filament CVD, where 10 μm in height forests were grown for 1 hour [9].

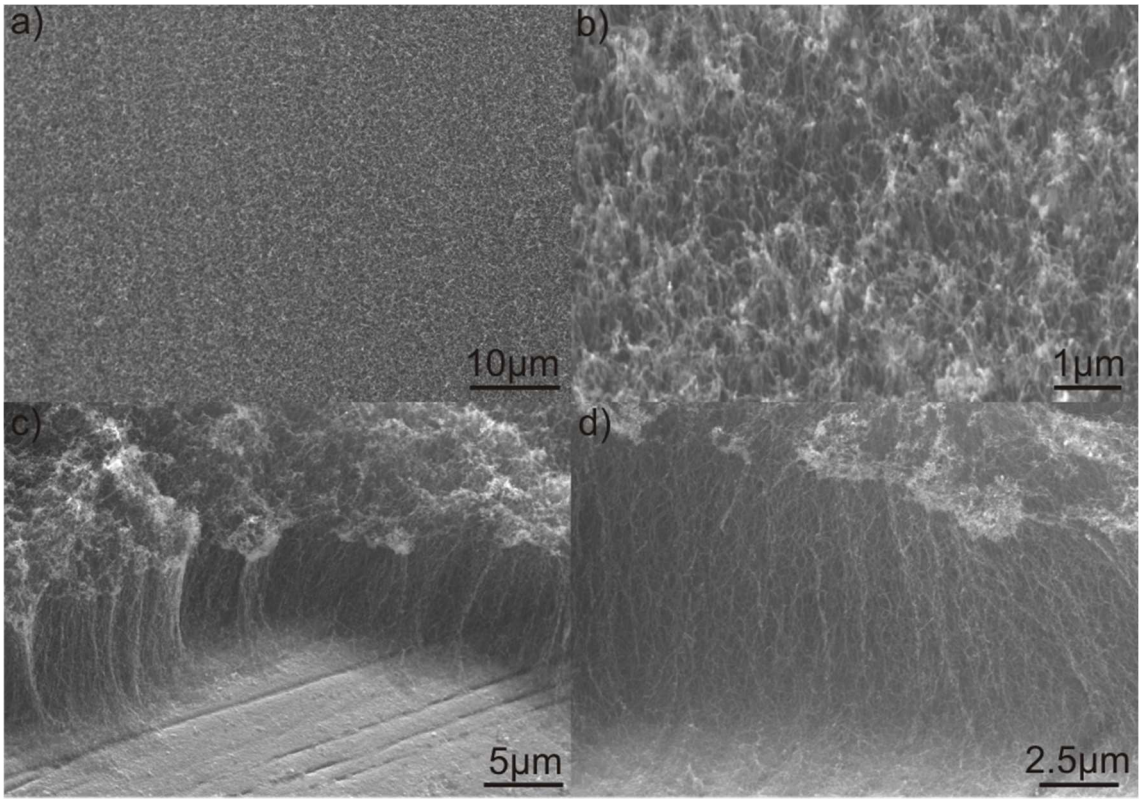

Figure IV.7. SEM images of the CNTs distribution over the substrate at different magnifications: (a) top view; (b) 45º tilted; (c and d) side views of the VACNTs.

The TEM image reported in Figure IV.8a depicts an overview of the CNTs taken at low magnification. The image reveals that the nanotubes are multiwalled CNTs with 14-18 nm in outer diameter. The crystallinity of the CNTs was examined by HRTEM together with SAED shown in Figure IV.8b and c, respectively. The characteristic 0.34 nm inter-wall spacing of the CNTs is given in Figure IV.8b and the ring-like pattern in SAED in Figure IV.8c shows the (002) and (004) rings planes of the graphitic walls.

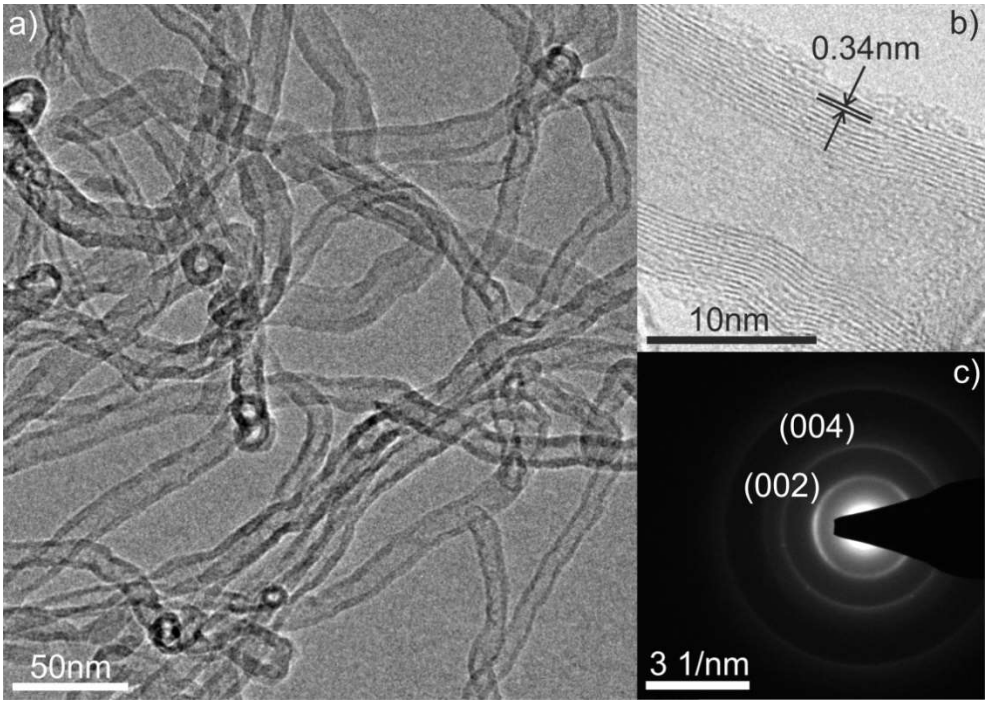

Figure IV.8. Overview TEM and HRTEM image (a,b) and SAED ring-like pattern (c) of the CNTs.

Raman spectroscopy was employed to investigate the purity and the degree of graphitization of the grown VACNTs. As shown in Figure IV.9, the Raman spectra exhibit two main bands around 1340 cm^{-1} (D band) and around 1575 cm^{-1} (G band) characteristics of multi-walled CNTs [15-18]. For comparison, the CNTs were also grown on Si buffered substrate, i.e., iron thin film was deposited onto $Al_2O_3/SiO_2/Si$ substrate by physical vapor deposition. The strong G band corresponds to the stretching mode of the C-C bond in the graphitic plane and demonstrates the presence of crystalline graphitic carbon. On the other hand, the D band is indicative of defects in CNTs, i.e., carbonaceous impurities with sp^3 bonding and broken sp^2 side walls. The intensity ratio I_D/I_G is indicative of the degree of purity of the CNT samples [17]. The lower value of this ratio indicates less defects and amorphous carbon and thus higher level of purity. The I_D/I_G ratio estimated from the Raman studies are I_D/I_G = 1.00 and 0.91 for the VACNTs grown onto Inconel substrate and Si buffered substrate, respectively. These results reveal a similar defects level of both of the VACNTs samples.

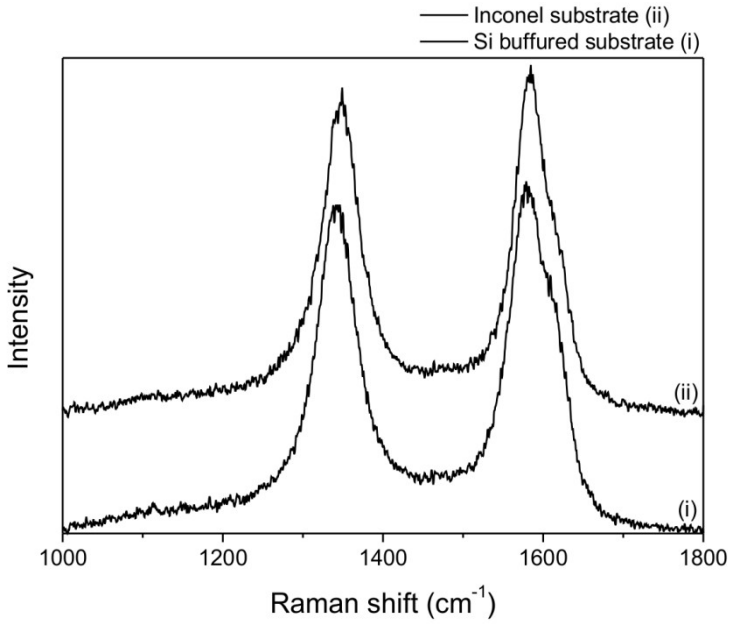

Figure IV.9. Raman spectra of CNTs grown on Si buffered substrate (i) and Inconel substrate (ii), for comparison purpose.

It is generally accepted that the CNT growth mechanism is dependent on the surface chemistry interactions between the carbon precursor and the existent metallic phases, and also on the presence of an underneath diffusion barrier [6,9]. As above reported, Fe preferably diffuses into the surface leading to the formation of Fe_2O_3 that is subsequently reduced to Fe in the annealing step. As matter of fact, Fe_2O_3 nanoparticles have been intentionally used as pre-catalyst for VACNTs growth. [19,20]. For example, we already showed that a microwave-assisted synthesis of a solution of $Fe(acac)_3$ in benzyl alcohol permitted the deposition of Fe_2O_3 nanoparticles onto a variety of substrates, which were shown to be the active catalysts, after the in-situ reduction to metallic Fe, for the VACNTs growth [21].

The Inconel surface was characterized by grazing angle XRD after the CNT growth (Figure IV.10) and the removal of the VACNTs. The pattern, on top of the reflections of Ni, shows low intensity Fe reflections and no Fe_2O_3. This demonstrates that, on the one hand Fe_2O_3 has been reduced to metallic Fe, which was the active catalyst in the CNTs growth.

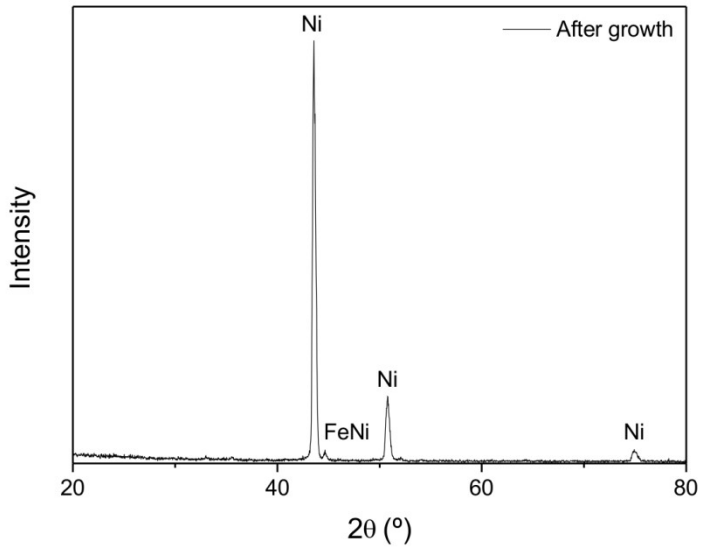

Figure IV.10. XRD pattern of the Inconel substrate after the CNT growth step (CNTs were removed by sonication process not to alter the surface).

On the other hand, the low intensity of the Fe reflections suggests that most of the surface iron catalysts particles are lifted up during the growth, as also in agreement with the TEM image reported in Figure IV.11.

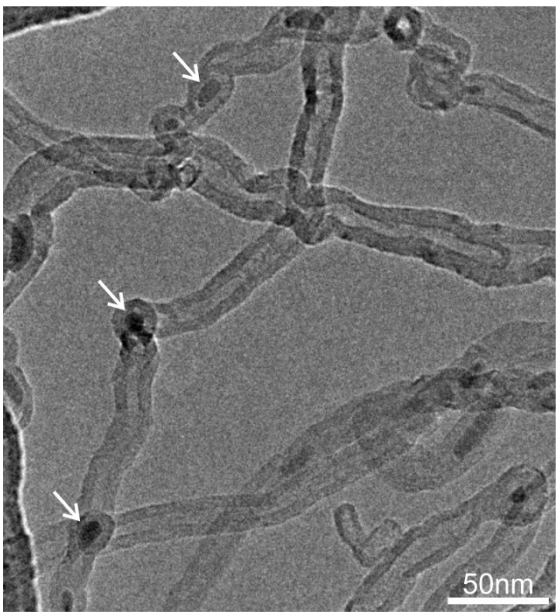

Figure IV.11. Overview TEM image illustrating the catalyst nano-sized particles (marked with a white arrow) inside of the tubes.

The presence of these particles inside of the tubes can be due to the growth process that employs the whole Inconel surface as catalyst. Chen *et al.* [22] suggested that stretching force causes the nano-sized catalytic particles that are in a liquid state at the growth temperature, to elongate and finally to break into two parts, one staying at the base, while

another being lifted up. It can be concluded that the CNTs grown on the Inconel follow the base growth mechanism. No less important is the Cr_2O_3 layer formation underneath the outer Fe_2O_3 layer (Figures IV.3 and IV.5) that acts as a diffusion barrier and supporting layer for the formation of evenly distributed nano-sized catalyst particles [9]. Indeed, a Cr_2O_3 oxide layer has been used by others for the stabilization of Fe on Inconel and subsequent CNT growth by vapor-phase catalyst delivery CVD method [1,4-6].

IV.3.3. Wettability test

Before the electrochemical characterization, the wettability test of the VACNTs/Inconel electrode was carried out in order to investigate the interaction between the liquid and the CNTs surface. From Figure IV.12, it can be observed that the VACNTs present a good degree of surface wettability supported by the water contact angle of 75º (where a contact angle of 0º means complete wetting). This specific property is useful for making intimate contact of aqueous electrolyte with the electrode surface in supercapacitors applications and the excellent surface wettability towards the aqueous electrolyte is also an essential factor for better performance.

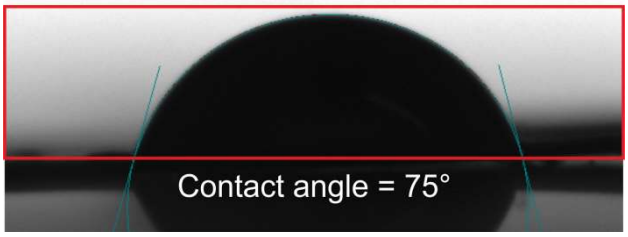

Figure IV.12. Water contact angle measurement of VACNTs electrode.

IV.3.4. Electrochemical characterization

In order to prove that the VACNTs directly grown on the metallic current collector (Inconel substrate) display good electrical properties and can be used as electrode in a variety of applications electrochemical measurements have been carried out. Figure IV.13a shows cyclic voltammograms (CV) of the CNTs/Inconel at different scan rates ranging from 5 to 100 mV s^{-1} in 1 M Na_2SO_4, where the potential limits are restricted from -0.8 to 0.7 V in a standard three electrode cell.

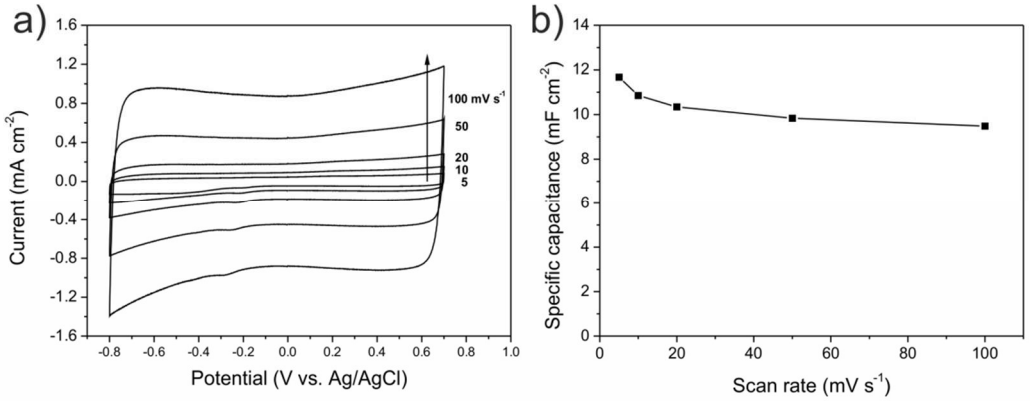

Figure IV.13. Cyclic voltammograms (a) of CNTs/Inconel electrode measured at different scan rates ranging from 5to 100 mV s^{-1} and dependence of the specific capacitance derived from the CV measurements (b).

It can be seen that all CV curves at the different scan rates are all of a rectangular-like shape. It is well known that a large-current, rectangular-type CV and symmetry in anodic and cathodic directions are the indications of ideal capacitor behavior of the electrode materials. This suggests that the VACNTs have very rapid current response on voltage reversal, small equivalent serial resistance (ESR) and low contact resistance with the substrate. The straight rectangular sides of *I-E* responses also support this feature. As a matter of fact, a large resistance will distort the response, into a narrower loop with an oblique shape, especially at a high sweep rate [20]. The capacitance was derived from the cyclic voltammogram curves using the equation (1):

$$C_{sp} = \frac{\int I(E)dE}{2v(E_2 - E_1)A} \qquad \text{Equation (1)}$$

where C_{sp} is the specific capacitance in mF cm^{-2}, $I(E)$ is the instantaneous current in A, v is the scan rate in V s^{-1} and $(E_2\text{-}E_1)$ is the potential range in V and A is the electrode area in cm^2. Therefore, the average C_{sp} was obtained by integrating positive and negative current over the CV curves [19]. The overall measured capacitance for the three-electrode system was 10.43 mF cm^{-2}. Figure IV.13b shows the influence of scan rate on C_{sp}. It can be seen a C_{sp} of 11.67 mF cm^{-2} is obtained at low scan rate of 5 mV s^{-1} and the C_{sp} only slightly decrease with the increasing potential scan rate, indeed at a high scan rate of 100 mV s^{-1}, the VACNTs still delivery a significant C_{sp} of 9.48 mF cm^{-2} with the increasing potential scan rate, indeed at a high scan rate of 100 mV s^{-1}, the VACNTs still delivery a significant C_{sp} of 9.48 mF cm^{-2}.

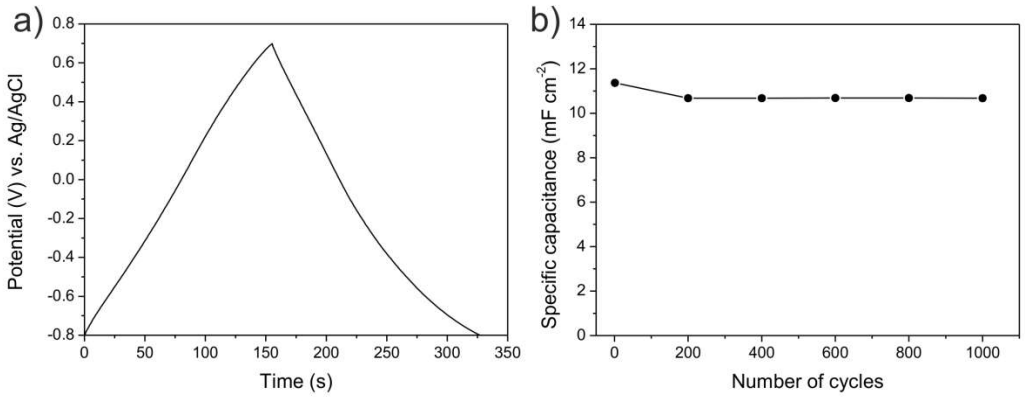

Figure IV.14. Galvanostatic charge-discharge curve (a) of the CNTs/Inconel electrode under a current density of 0.5 A g^{-1} and dependence of the specific capacitance on the cycle number (b).

Galvanostatic charge-discharge measurements were also applied to characterize the properties of the CNTs/Inconel electrode, where the carbon based electrode was charge-discharged under a current density of 0.5 A g^{-1}. Figure IV.14a shows a typical current charge-discharge (E-t) curve of the CNTs/Inconel electrode. On both curves, the E-t responses of the charge process reveal a mirror-like image of their corresponding discharge counter parts and no significant IR drop was observed. It can be concluded that the resistance is low and highly charge-discharge efficiency. The C_{sp} can be estimated according to the following equation (2):

$$C_{sp} = \frac{I\Delta t}{\Delta E m} \qquad \text{Equation (2)}$$

where the I refers to discharge current in A, Δt represents the discharge time in s and ΔE is the potential range in V and m is the electrode mass in g. The calculated C_{sp} of the CNTs/Inconel electrode was 11.37 mF cm^{-2}. In order to evaluate the stability of the CNTs/Inconel electrode during the charge-discharge cycle, the values C_{sp} with respect to charge-discharge cycle number (up to 1000 cycles) were measured (Figure IV.14b). The C_{sp} decline slowly during the first 200 cycles but remained constant thereafter. Since the length of cycle life of a supercapacitor is a crucial parameter for its application. The calculated specific capacitances from the CV and galvanostatic charge-discharge techniques corroborate each other. These findings emphasize that the grown multi-walled CNTs are active electrode materials for storage of energy in supercapacitors by the development of a double layer capacitance.

Electrochemical impedance spectroscopy results represented by Nyquist plot (Figure IV.15) consist of three frequency-dependent regions. At very high frequencies (A), the CNTs electrode behaves like a pure resistance. The equivalent series resistance (ESR) obtained from the real axis intercept of the Nyquist plot is 9.1 Ω corresponding to the sum of electrolyte resistance and contact resistance between the CNTs and the current collector (Inconel) [23]. At low frequency (region B), the imaginary part of the impedance sharply

increases and the plot tends to a vertical line characteristic of a purely capacitive behavior. This vertical line along the imaginary axle indicates good capacitance behavior and lower ion diffusion resistance of the CNTs/electrolyte.

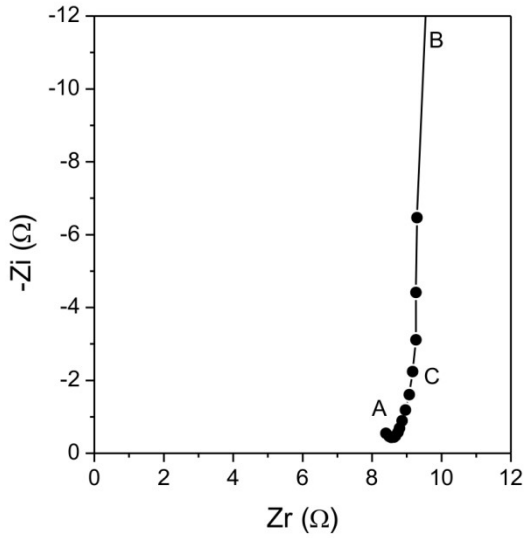

Figure IV.15. Nyquist plot of the CNTs/Inconel electrode.

The influence of the matt-like structure and thickness of the CNTs electrode on the access of the electrolyte to the entire available surface, can be observed in the medium frequency (C). It can be concluded that the as-prepared CNTs provide a large accessible area for the electrolyte diffusion and therefore the formation of the double layer capacitance. Moreover, these findings imply that the VACNTs exhibit low internal resistance and good dynamic charge-discharge response characteristics

IV.4. Conclusions

Here we have reported for the first time a simple procedure to directly grow VACNTs on an Inconel substrate by TCVD, without the addition of an external catalyst. The Inconel substrate surface acts both as catalyst and as support for the CNTs growth. The results demonstrate that the growth of VACNTs is directly related to the uniformly dispersed and densely packed nano-sized catalytic particles formed by a simple annealing of the Inconel® alloy in air. This work paves the way for the growth of CNTs directly on metallic substrates which resolves the problem of adhesion of nanotubes on metallic substrates and fulfills the requirement for electrochemical applications. Further evidence in support of this statement was obtained from the cyclic voltammetry and electrochemical impedance spectroscopy. Finally, our growth process may lead to new opportunities in electrode preparation for various applications in sensors and energy storage and conversion.

References

[1] S. Talapatra, S. Kar, S.K. Pal, R. Vajtai, L. Ci, P. Victor, M.M. Shaijumon, S. Kaur, O. Nalamasu, P.M. Ajayan, *Nat. Nanotechnol.*, **2006**, *1*, 112.

[2] L. Gao, A. Peng, Z.Y. Wang, H. Zhang, Z. Shi, Z. Gu, G. Cao, B. Ding, *Solid State Comm*, **2008**, *146*, 380.

[3] H. Zhang, G. Cao, Y. Yang, *Energy Environ. Sci.*, **2009**, *2*, 932.

[4] S. K. Pal, S. Talapatra, S. Kar, L. Ci, R. Vajtai, T. Borca-Tascicu, L.S. Schadler, P.M. Ajayan, *Nanotechnology*, **2008**, *19*, 045610.

[5] J.B. Bult, W.G. Sawyer, P.M. Ajayan, L.S. Schadler, *Nanotechnology*, **2009**, *20*, 085302.

[6] S.K. Pal, S. Kar, S .Lastella, A. Kumar, R. Vajtai, S. Talapatra, T. Borca-Tascicu, P. M. Ajayan, *Carbon*, **2010**, *48*, 844.

[7] D. Mata, R.M. Silva, A.J.S. Fernandes, F.J. Oliveira, P.M.F.J. Costa, R F. Silva, *Carbon*, **2012**, *50*, 3585.

[8] S. Sridhar, L. Ge, C.S. Tiwary, A.C. Hart, S. Ozden, K. Kalaga, S. Lei, S.V. Sridhar, R. K. Sinha, H. Harsh, K. Kordas, P.M. Ajayan, R. Vajtai, *Appl. Mater. Interfaces*, **2014**, *6*, 1986.

[9] W. Yi, Q. Yang, *Diam. Relat. Mater.*, **2010**, *19*, 870.

[10] W. Yi, Q. Yang, *Appl. Phys. A,* **2010**, *98*, 659.

[11] J. Xiao, N. Prud'homme, N. Li, V. Ji, *Appl. Surf. Sci.*, **2013**, *284*, 446.

[12] J.M. Francis, J.A. Jutson, J.H. Buddery, *J. Mat. Sci.*, **1967**, *2*, 78.

[13] H. Ma, L. Pan, Y. Nakayama, *Carbon*, **2011**, *49*, 854.

[14] Y. Lan, Y. Wang, Z.F. Ren, *Adv. Phys.*, **2011**, *60*, 553.

[15] F. Tuinstra, J.L. Koenig, *J. Chemical Phys.*, **1970**, *53*, 1126.

[16] A.M. Rao, A. Jorio, M.A. Pimenta, M.S.S. Dantas, R. Satio, G. Dresselhaus, M.S. Dresselhaus, *Phys. Rev. Lett.*, **2000**, *84*, 1820.

[17] M.S. Dresselhaus, G. Dresselhaus, R. Satio, A. Jorio, *Phys. Reports*, **2005**, *409*, 47.

[18] R.A. DiLeo, B.J. Landi, R.P. Raffaelle, *J. Appl. Phys.*, **2007**, *101*, 064307.

[19] M. Felisberto, L. Sacco, I. Mondragon, G.H. Rubiolo, R.J. Candal, S. Goynes, *Mater. Lett.* **2010**, *64*, 2188.

[20] K. Yamada, A. Kaneko, H. Kato, Y. Homma, *Mater. Express*, **2012**, *2*, 257.

[21] R.M. Silva, A. Pucci, C. Marichy, D. Mata, M.C. Ferro, R.F. Silva, N. Pinna, *Cryst. Eng. Comm.*, 2012, **14**, 48.

[22] X. Chen, R. Wang, J. Xu, D. Yu, *Micron*, 2004, **35**, 455.

[23] B.E. Conway, in *Electrochemical Supercapacitors: Scientific Fundamentals and Technological Applications*, Plenum, **1999**, New York.

Chapter V

Chapter preface

This work consist in a novel atomic layer deposition process of manganese oxide for preparing "ready to use" nanocomposite supercapacitor electrodes. These electrodes consist on 3D-array of vertically aligned carbon nanotubes, directly grown on conductive Inconel®600 substrates, coated with manganese oxide by atomic layer deposition. The direct growth of vertically aligned carbon nanotubes on the current collector forms and provides efficient electron transport pathways, it is therefore not necessary to use extra binders or conductive additives. In addition, the 3D-arrays of vertically aligned carbon nanotubes are good supporting "scaffolds" for atomic layer deposition of manganese oxide. This greatly simplifies the electrode fabrication process. The present work was already published as a paper and highlights the versatility of the atomic layer deposition for the elaboration of original nanostructures targeting energy conversion and storage devices:

"Coating of vertically aligned carbon nanotubes by a novel manganese oxide atomic layer deposition process for binder-free hybrid capacitors"

R.M. Silva, G. Clavel, Y. Fan, P. Amsalem, N. Koch, R.F. Silva and N. Pinna, *Adv. Mater. Interfaces* **2016**, *1600313* (1 of 8).

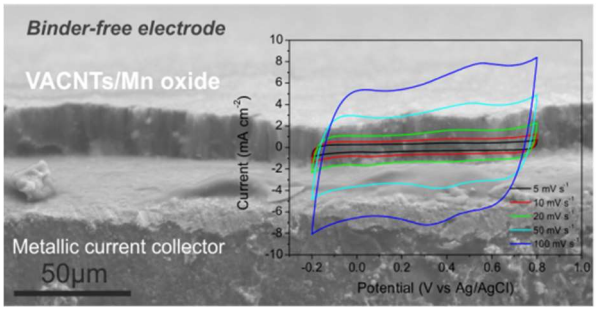

This manuscript received the contributions from G. Clavel, P. Amsalem, N. Koch and Y. Fan in terms of electron microscopy, X-ray photoelectron spectroscopy and electrochemical measurements and interpretation, respectively.

Coating of vertically aligned carbon nanotubes by a novel manganese oxide atomic layer deposition process for binder-free hybrid capacitors

Abstract

A novel atomic layer deposition process of manganese oxide from methylcyclopentadienyl manganese tricarbonyl and ozone has been developed. It is used to coat vertically aligned carbon nanotubes (VACNTs) grown on a conductive Inconel®600 substrate in order to produce a tree-dimensional array of metal oxide-carbon nanotube electrode. Electron microscopy studies showed that a conformal polycrystalline film could be deposited on the VACNTs arrays. X-ray diffraction, small area electron diffraction and X-ray photoelectron spectroscopy analysis determined the formation of hausmannite (Mn_3O_4). The electrochemical properties of the as-prepared VACNTs/Mn_3O_4 nanocomposite electrodes were studied using cyclic voltammetry, galvanostatic charge and discharge cycling in 1M Na_2SO_4 aqueous electrolyte. Capacitances as high as 78.62 mF cm^{-2} at 5 mV s^{-1} are demonstrated which is one order of magnitude higher than that of pristine VACNTs. In addition, the as-prepared VACNTs/Mn_3O_4 nanocomposite electrode showed a good reversibility and cycling stability.

V.1. Introduction

Electrochemical capacitors (ECs), also known as supercapacitors (SCs), are electrochemical energy storage systems with high power density filling the gap between batteries and conventional capacitors. They can be used in high power applications such as hybrid electric vehicles or as possible auxiliary energy storage devices in combination with rechargeable batteries. ECs can be categorized, according to the charge storage mechanism, as electrochemical double layer capacitor (EDLC) and pseudocapacitor. The origin of the capacitance in the EDLC is due to charge separation at the electrode-electrolyte interface. In contrast, the pseudocapacitance arises from fast and reversible Faradaic redox reactions taking place at or near the electrode surface [1-4]. Among various electrochemically active materials, late transition metal oxides have received a great deal of attention because of high theoretical capacity and rich redox chemistry [5,6]. In particular, the oxides of manganese are preferred owing to their outstanding structural flexibility and environmentally benign nature. However, the utilization of manganese oxide as electrode material for supercapacitors is limited by its poor electrical conductivity. This problem can be overcome by coating manganese oxide on an electrically conductive nanostructured substrate such as carbon nanotubes (CNTs) [6,7].

One elegant strategy is to combine manganese oxide (nanoparticles or thin coating) with vertically aligned CNTs (VACNTs) arrays providing parallel pathways to allow fast electron and electrolyte ion transport. If VACNTs can be directly grown on a metallic current collector, no additional preparation step is needed for the fabrication of the electrode material due to the good contact between the CNTs and the conductive substrate. Indeed, we recently reported that VACNTs arrays coupled to a conductive Inconel® substrate could be used directly as electrodes in EDLC [8]. With the addition of a manganese oxide coating, an increase in the overall capacity of the electrode material, by providing additional pseudocapacitance due to reversible redox reactions of the manganese oxide coating, is expected [7,9]. As a result, the nanocomposite electrode, consisting of a conductive nanotubular structure (VACNTs) coated by a redox active phase with pseudocapacitive properties (metal oxide), combines the advantages of both materials.

In this context, atomic layer deposition (ALD) is one of the most attractive technique for the preparation of such nanostructured materials [10-12]. ALD is based on self-limiting surface reactions, where gas-phase reactions are eliminated by sequential pulsing of the individual precursors into the reaction chamber separated by purges [13,14]. In this manner, the gas-phase precursors diffuse in high aspect ratio structures and form conformal coatings over complex substrates geometries. This feature makes ALD suitable to deposit uniform layers of electrochemical active materials on 3D nanostructures such as VACNTs arrays. As a matter of fact, electrochemical active materials (particles or coatings) deposited by ALD for supercapacitors and lithium batteries have been already reported [11,15].

Previous studies demonstrated that manganese oxide can be grown by ALD giving access to several phases depending on the manganese precursor, oxygen source and deposition temperature used. For example, MnO and MnO_2 have been prepared using Bis (ethylcyclopentadienyl)manganese ($Mn(CpEt)_2$) and water (H_2O) [16-18] and Hthds - 2,2,6,6-tetramethylheptan-3,5-dione ($Mn(tdh)_3$) and ozone (O_3) [19,20], respectively. Mn_3O_4 phase could have only been obtained by Plasma Enhanced ALD from $Mn(tdh)_3$ [21]. Post-annealing process can then be applied to oxidize the manganese oxide or to improve its crystallinity [22]. In addition to the above mentioned and most commonly used manganese precursors, methylcyclopentadienyl manganese tricarbonyl ($MeCpMn(I)(CO)_3$) has been suggested as a promising precursor for the ALD of manganese containing films. This precursor presents sufficient volatility and thermal stability needed in ALD gas-phase process [23,24]. As a matter of fact, due to its volatility it was already applied for the CVD of Mn, MnO_x and $MnSi_xO_y$ [25-29]. One important requirement for achieving manganese oxide ALD using $MeCpMn(I)(CO)_3$ precursor is to find an oxygen source with appropriate reactivity that leads to complete reaction. Ozone is a strong oxidizing agent commonly used as co-reactant of cyclopentadienyl-based precursors [30]. Moreover, ozone offers the possibility for the *in situ* functionalization of the CNTs in order to provide the active surface species required to nucleate the ALD film [31,32]. For example, Tong *et al.*

reported the growth of NiO nanoparticles onto CNTs using O_3 as oxygen source and for the *in situ* functionalization of pristine CNTs [33].

Herein, we present an unprecedented Mn_3O_4 ALD process from $MeCpMn(I)(CO)_3$ and O_3. Following this approach, Mn_3O_4 ALD thin films were deposited on various supports such as glass, commercial CNTs (c-CNTs), VACNTs growth on silicon and Inconel®. Though, the present study is focused on coating 3D VACNTs architectures on conductive Inconel® substrates to be used as electrode materials for supercapacitors. The obtained nanocomposites are "ready to use" electrodes, i.e. do not need to be mixed with binding additives nor coated onto a current collector. The electrochemical properties of the nanocomposites were studied by cyclic voltammetry (CV), galvanostatic charge-discharge (GCD) and electrochemical impedance spectroscopy (EIS). For comparison, the electrochemical behavior of pristine (i.e. uncoated) VACNTs is also reported.

V.2. Experimental Section

V.2.1. Sample preparation

Manganese oxide was deposited on commercial carbon nanotubes (c-CNTs) from Applied Science, vertically aligned CNTs (VACNTs) grown by thermal chemical vapor deposition (TCVD) onto conductive Inconel® and onto silicon, and on glass substrates. The c-CNTs from Applied Science were treated with concentrated HNO_3 at 100 °C for 2 h before deposition. The VACNT arrays were grown by TCVD technique directly on 1x1 cm^2 pretreated Inconel® metallic substrates and also on silicon buffered substrate from a mixture of acetylene and hydrogen (C_2H_2/H_2) at 650 °C using argon (Ar) as a carrier gas. Details about the TCVD CNTs growth are given elsewhere [8]. The development of the manganese oxide ALD process was carried out in an ARRADIANCE GEMStar-6 reactor with a 0.2 Torr base pressure. Methylcyclopentadienyl manganese tricarbonyl ($MeCpMn(I)(CO)_3$) was used as the manganese precursor, and was kept at 80 °C in its precursor cylinder during deposition. Ozone, used as the oxygen source, was generated from a BMT803N ozone delivery system from pure oxygen at a concentration between 100 and 250 g/Nm^3. Argon was used as both carrier gas for the manganese precursor and the purge gas. Additionally, the delivery lines of the circuit were heated to 130 °C to prevent the precursors from condensation throughout the deposition. The precursors were pulsed by ALD pneumatic valves alternative into the reactor, separated by Ar purges. In a typical process, each ALD cycle consisted of 0.5s $MeCpMn(I)(CO)_3$ pulse, 30 s of residence time, 20 s Ar purge, 1.0s O_3 pulse, 20 s of residence time and 20 s Ar purge. Several samples, with different manganese oxide thicknesses, were prepared. The growth per cycle (GPC) was obtained from the film thickness divided by the number of ALD cycles.

V.2.2. Sample characterization

Structural and morphological properties of c-CNTs/manganese oxide and VACNTs/manganese oxide nanocomposites were characterized by scanning electron microscopy (SEM) performed with a Hitachi SU-70 microscope operated in secondary electron mode at 15 kV and equipped with energy dispersive X-ray spectroscopy (EDS). Grazing incident X-ray diffraction (GIXRD) was carried out using a Rigaku Geigerflex D Max-C Series diffractometer on glass substrate coated with manganese oxide. The radiation used was Cu Kα (λ=1.5418 Å), with a scan time of 100 s and step size (2θ) of 0.02°. The diffractometer was operated with nearly parallel grazing incident angle of 1.5°.

Transmission electron microscopy (TEM) measurements and selected area electron diffraction (SAED) were carried out on a Philips CM200 microscope equipped with a LaB_6 source and operated at 200 kV. Samples for TEM observations were prepared by dry adhesion of the CNTs/manganese oxide to a carbon-coated copper grid. Raman spectroscopy (Jobin Yvon T64000) was carried out at a 532 nm excitation wavelength on the glass substrate coated with manganese oxide, pristine VACNTs and on the as-prepared VACNTs/manganese oxide nanocomposites. Atomic force microscopy (AFM) measurements were performed with an Ntegra Prima setup (NT-MDT) in tapping mode under ambient conditions. A silicon cantilever (Nanosensor PPP-NCHR) with the spring constant of k ≈ 42 N m^{-1} and tip radius less than 10 nm was used. X-ray photoelectron spectroscopy (XPS) was performed in an ultra-high vacuum chamber using a SPECS Phoibos 100 hemispherical energy analyzer and a non-monochromatic Al Kα (hν = 1486.6 eV) X-ray source (1.2 eV energy resolution). The electrochemical measurements were performed using a Bio-Logic VMP3 Potentiostat-Galvanostat (Science Instruments). The experiments were conducted in a three-electrode electrochemical set-up, where the VACNTs/Mn_3O_4 (1x1 cm^2) was used as the working electrode, with platinum foil as the counter electrode and a standard silver/silver chloride electrode (Ag/AgCl) as the reference electrode. The electrolyte (1M Na_2SO_4) was prepared from Na_2SO_4 (Sigma Aldrich, 99.0%) and Millipore water. The areal capacitance (specific capacitance) was calculated using the area of the electrode exposed to the electrolyte during the electrochemical measurements. This area was 1 cm^2. From the cyclic voltammetry (CV) measurements, the specific capacitance *(C_{sp})* of the electrodes can be evaluated using the following equation (1):

$$C_{sp} = \frac{\int I(E)dE}{2v(E_2 - E_1)A} \qquad \text{Equation (1)}$$

where C_{sp} is the specific capacitance in mF cm^{-2}, *I(E)* is the instantaneous current in A, *v* is the scan rate in V s^{-1}, *(E_2-E_1)* is the potential range in V and *A* is the electrode area in cm^2. Therefore, the average C_{sp} was obtained by integrating positive and negative current over the CV curves. The CV curves were recorded with the samples that were first stabilized by cycling 20 times at scan of 20 mV s^{-1}.

The C_{sp} was also estimated from the galvanostatic charge and discharge (GCD) cycling according to the following equation (2):

$$C_{sp} = \frac{I\Delta t}{\Delta EA} \qquad \text{Equation (2)}$$

where I refers to discharge current in A, Δt represents the discharge time in s, A is the electrode area in cm^2 and ΔE is the potential range in V. Electrochemical impedance spectroscopy (EIS) studies were carried out in the frequency region from 0.01 to 100,000 Hz with the test signal amplitude of 5 mV.

V.3. Results and discussion

V.3.1. ALD of manganese oxide

Manganese oxide was deposited by ALD from $MeCpMn(I)(CO)_3$ as manganese source and O_3 as oxygen source. The influence of the $MeCpMn(I)(CO)_3$ pulse time on the growth per cycle (GPC) of the films was evaluated at a deposition temperature of 200 °C by varying the pulse time from 0.2 to 2.5 s with a fixed purging time of 20 s. Measurements of film thickness were carried out after 100 or 300 cycles for different pulse lengths time from TEM images acquired from nitric acid treated c-CNTs (Figure V.1a,b). It should be pointed out that although the thickness estimation from TEM images on CNTs is not very accurate our approach gives the actual GPC for carbon substrates. The thin manganese oxide coating is seen as the darker contrast at the edge of the c-CNTs as indicated in the insets of Figure V.1a,b.

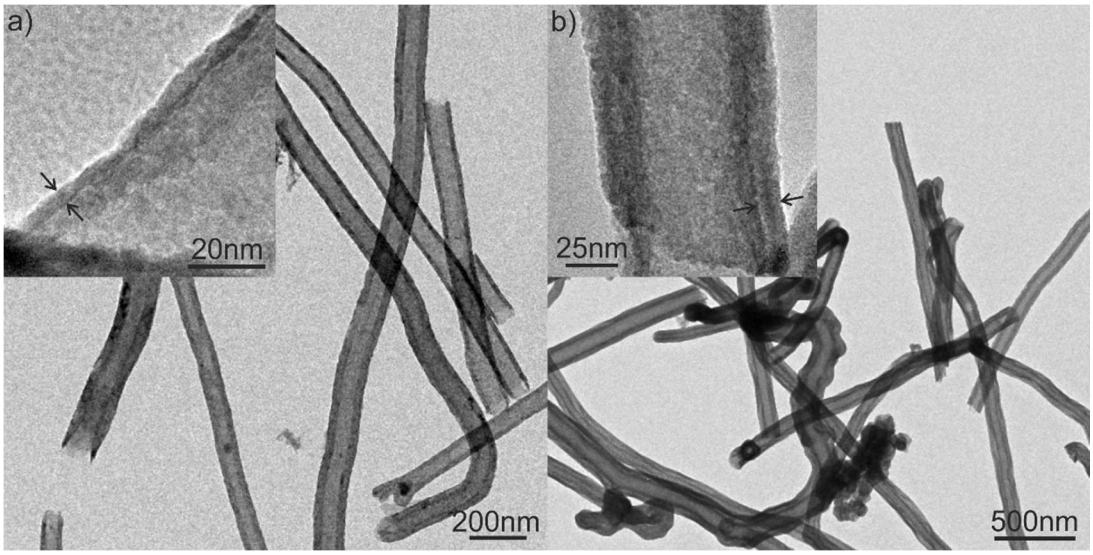

Figure V.1. Overview TEM images of coated c-CNTs with manganese oxide after (a) 100 and (b) 300 ALD cycles, respectively. The insets show high resolution images.

The GPC for different pulse lengths time showed that saturation was achieved after 0.5 s for the $MeCpMn(I)(CO)_3$ pulse (Figure V.2a). No noticeable increase of the GPC is observed for longer pulse time. Figure V.2b shows the establishment of a steady GPC after 0.2 s for the O_3 pulse time, *i.e.* no marked change in the GPC was observed by varying the O_3 pulse time from 0.2 to 1.5 s. Both curves indicate a self-limiting growth profile of the ALD process with a GPC value of around 0.45 nm at 200 °C.

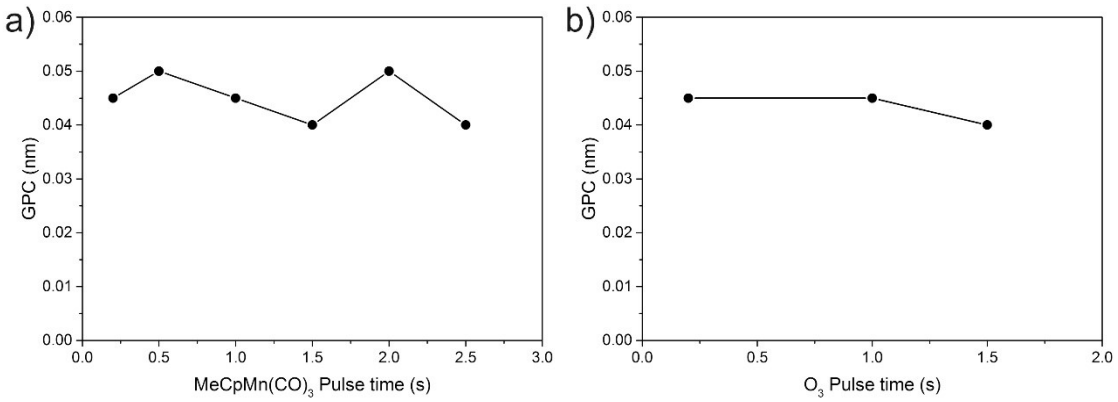

Figure V.2. ALD saturation curve for pulse lengths time of (a) $MeCpMn(I)(CO)_3$ and (b) O_3. The thickness is obtained after 100 cycles from TEM measurements. The deposition temperature was set at 200 °C.

To determine the appropriate ALD process window, the GPC was evaluated at temperatures ranging from 100-275 °C (Figure V.3a). As the substrate temperature increased from 100 to 175 °C, the GPC of Mn oxide decreased slightly from 0.053 nm to 0.034 nm. A further increase in deposition temperatures resulted in an increase of the GPC (Figure V.3a) hovewer the self limiting character of the deposition has been ascertained by changing the pulse time of the reactant. The observed GPC are comparable to GPC reported in literature for other manganese oxide processes [16-20]. A linear increase of the thickness as a function of ALD cycles is observed (Figure V.3b) further demonstrating the self-limiting character of the process.

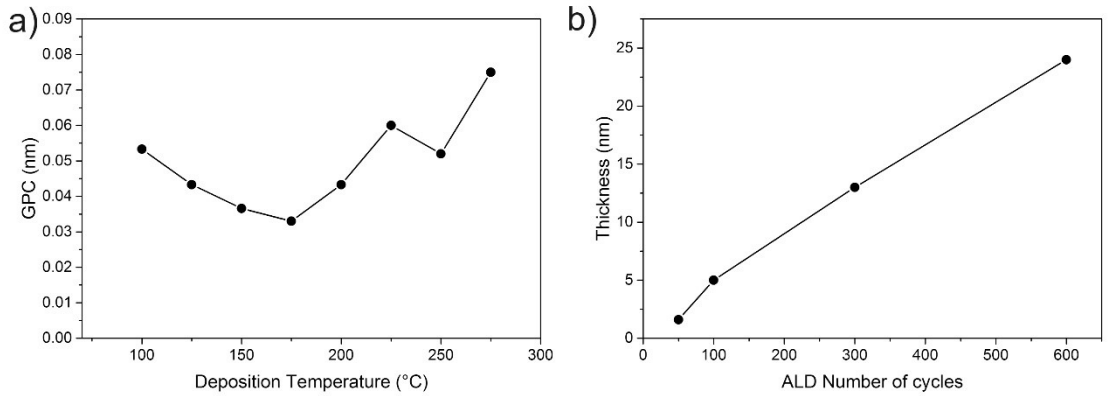

Figure V.3. (a) GPC of manganese oxide films plotted as a function of the temperature. The GPC is deduced from the film thickness measured after 300 ALD cycles onto c-CNTS from electron microscopy images. (b) Thickness as a function of the number of cycles under self-limiting conditions.

Grazing incidence X-ray diffraction (GIXRD) was used to identify the phase of the manganese oxide films deposited on glass after 800 ALD cycles. The diffraction pattern shows broad reflections on a high background due to the amorphous substrate (Figure V.4a). The reflections at 28.9˚, 32.4˚, 36.1˚, 44.5˚ and 59.9˚ correspond to the (112), (103),

(211), (220) and (224) planes of Mn_3O_4 hausmannite (JCPDS card No. 24-734). The broad and low peak intensities in the XRD pattern are indicative of the formation of nanocrystalline Mn_3O_4. Further evidence for the formation of Mn_3O_4 is revealed by Raman spectroscopy (Figure V.4b). The main peak located at 653.6 cm^{-1} is ascribed to Mn_3O_4, and is similar to those reported in literature for Mn_3O_4 [34,35]. Additionally, the Mn_3O_4 thin film prepared on glass substrate was imaged using atomic force microscopy (AFM) as shown in Figure V.4c. Surface roughness distribution of the film is shown as the inset of Figure V.4c, from which an average surface roughness of 1.13 nm has been measured. Morphological features clearly showed the homogeneous deposition of Mn_3O_4 layer over glass substrate and the AFM cross-section height profile (Figure V.4d) documents the granular structure.

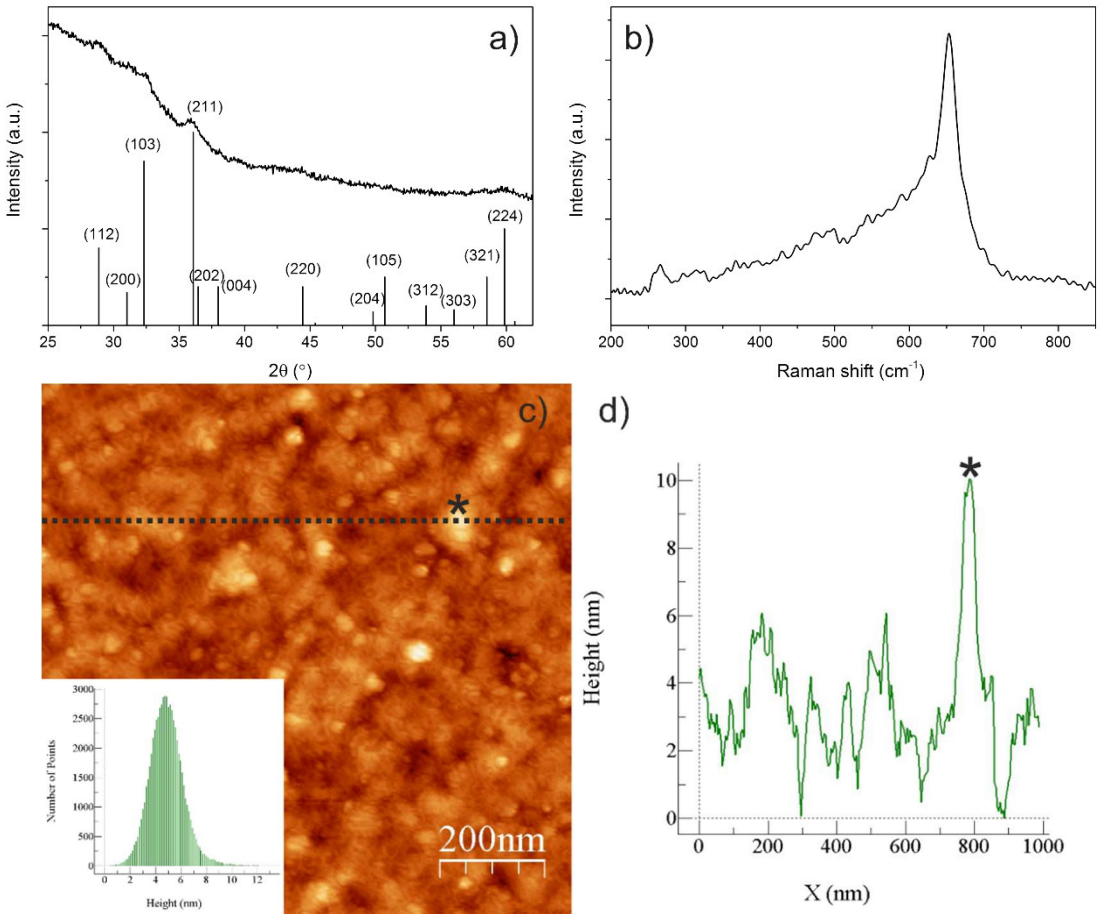

Figure V.4. Representative GIXRD diffraction pattern (a), Raman spectrum (b) and AFM image (c) of manganese oxide thin film deposited on a glass substrate after 800 ALD cycles at 200 °C. The inset in (c) shows the roughness distribution, which gives a mean value of 1.13 nm. This is the resultant roughness of the thin film and the glass substrate over a scanned area of 1 µm x 1 µm. AFM cross-section height profile (d) of the surface of Mn_3O_4 film, across the black dashed line shown in (c).

The formation of Mn_3O_4 phase is further confirmed by X-ray photoelectron spectroscopy (XPS) studies. The Mn 2p spectrum (Figure V.5a) shows two peaks corresponding to the Mn $2p_{3/2}$ and Mn $2p_{1/2}$ core levels centered at 653.6 eV and 642.0 eV binding energies, respectively. These results are in agreement with the binding energy of Mn 2p and the energy separation (ΔE = 11.6 eV) between $2p_{3/2}$ and $2p_{1/2}$ previously reported for hausmannite [36,39]. The Mn 3s spectrum (Figure V.5b) can be also employed as an indicator of Mn oxidation state. The observed Mn 3s multiplet splitting of ca. 5.4 eV is also consistent with previous reports and points to a mixed (II/III) valence of manganese as expected for Mn_3O_4 (+2.7) [36-38]. The relative concentration of Mn(II) and Mn(III) can be further determined by fitting the Mn 2p and Mn 3s spectra. This is performed here by employing the corresponding fitted parameters of the Mn 2p and Mn 3s core levels of MnO and manganite, as reported in ref. [39]. For the Mn 2p spectrum, a good fit is achieved with the ideal stoichiometry of 33.3% Mn(II) and 66.7% Mn(III) and an energy difference between the lowest binding energy components of the two oxidized states amounting to 0.65 eV in very good agreement with ref. [39]. In addition, a reasonable fit of the Mn 3s spectrum using the same method yields a concentration of 31% and 69% of Mn(II) and Mn(III), respectively. Consequently, these XPS results allow to confirm the formation of the stoichiometric hausmannite phase and the corresponding mixed oxidation states of manganese.

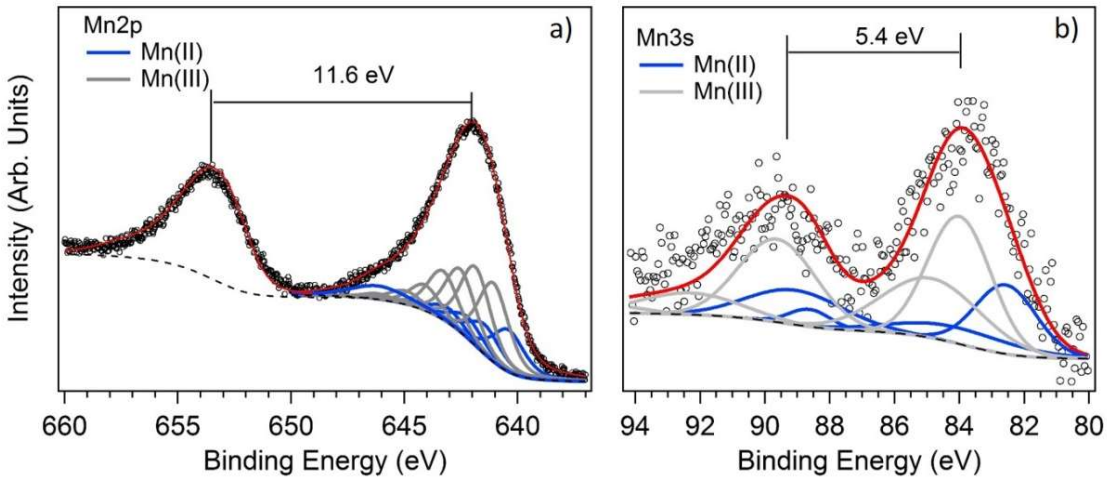

Figure V.5. Representative XPS spectra of VACNTs/Mn_3O_4 nanocomposite after 600 ALD cycles: (a) Mn 2p and (b) Mn 3s XPS spectrum.

V.3.2 VACNTs/Mn_3O_4 nanocomposite

Electron microscopy studies of VACNTs coated with 600 manganese oxide ALD cycles point to a continuous but granular coating on the surface of the CNTs grown on silicon (Figure V.6a-c) and Inconel® (Figure V.6d-f) substrate, respectively. Figure V.6b show a TEM image of an individual coated nanotube from the VACNT forest with a defective coating revealing the CNT underneath. Selected area electron diffraction (SAED) pattern

(Figure V.6c) recorded from a collection of few CNTs gives relatively sharp Debye-Scherrer diffraction rings, confirming the formation of a polycrystalline coating. The visible diffraction rings can be indexed to Mn_3O_4 (101), (112), (103), (211), (220) and (224) crystal planes. These findings are also supported by the TEM studies on c-CNTs, as reported in Figure V.6g-i. The granular coating is composed of randomly oriented nanocrystallines presenting lattice fringes with *d*-spacings of 0.50 nm, 0.28 nm and 0.25 nm that can be assigned to the (101), (103) and (211) planes of Mn_3O_4 phase, respectively. The formation of Mn_3O_4 is further confirmed by SAED showing Debye-Scherrer rings that can be assigned to the (101), (112), (103), (211), (220) and (224) reflections of Mn_3O_4 and the (002) of the graphitic walls of the c-CNTs. Hausmannite was the phase obtained at all the deposition temperature used. However, the crystallinity and crystalline size increase with the deposition temperature (Figure V.6i).

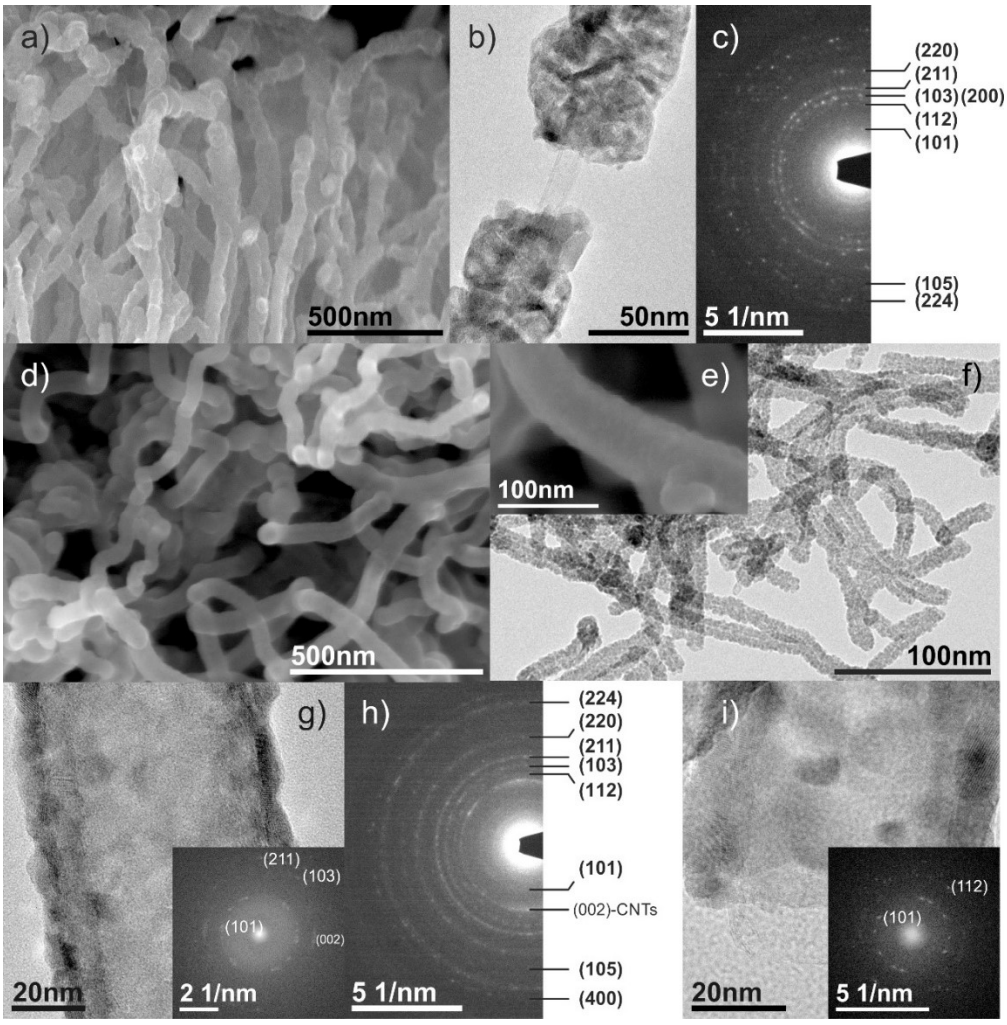

Figure V.6. Cross-section SEM image (a), TEM image (b) and SAED pattern (c) of the VACNTs supported on silicon coated with 600 cycles of Mn_3O_4. Top view high-magnified SEM image (d), SEM of an individual coated CNT (e) and overview TEM image (f) of the VACNTs/Mn_3O_4 nanocomposite supported on Inconel® after 600 cycles. HR-TEM image with corresponding Fourier transform (inset) (g) and SAED pattern (h) taken from c-CNTs coated with 100 cycles of manganese oxide. HR-TEM image with corresponding Fourier transform (i) of c-CNTs coated with 100 cycles of manganese oxide deposited at 250 °C.

The uniform distribution of the C, Mn and O species on the top surface of the VACNTs/Mn_3O_4 nanocomposite is demonstrated by energy-dispersive X-ray spectroscopy (EDS) (Figure V.7a) showing a low-magnified SEM image of the nanocomposite and the corresponding elemental maps.

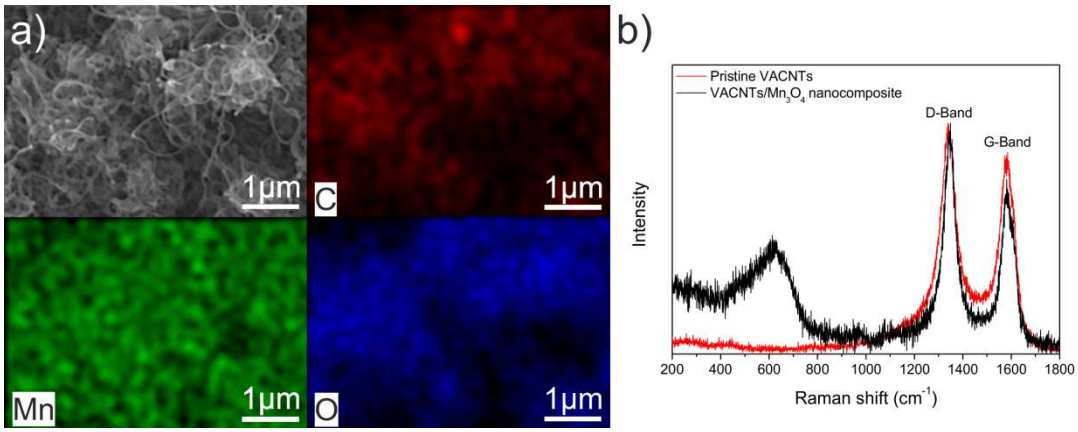

Figure V.7. Low-magnified SEM image (a) of the VACNTs supported on Inconel® coated with 600 cycles of Mn_3O_4 and the corresponding EDS mapping of carbon (red), manganese (green) and oxygen (blue). Raman spectra (b) of the pristine VACNTs (red) and VACNTs/Mn_3O_4 nanocomposite (black) supported on Inconel® after 600 ALD cycles.

An EDS line scan profile of a VACNTs/Mn_3O_4 nanocomposite on Inconel® substrate after 600 ALD cycles reveals that the Mn_3O_4 coating reach the entire length of the CNT forest but with an uneven distribution of the Mn_3O_4 (Figure V.8). A gradient of coating in such dense forest is not unusual as recently discussed by Stano *et al.*[40] Moreover, the decomposition of ozone in ALD processes [41] and especially onto MnO_x catalysts [21,42-45] can also be suggested as a cause of limited diffusion of ozone into high aspect ratio nanostructures, which would lead to an inhomogeneous growth along.

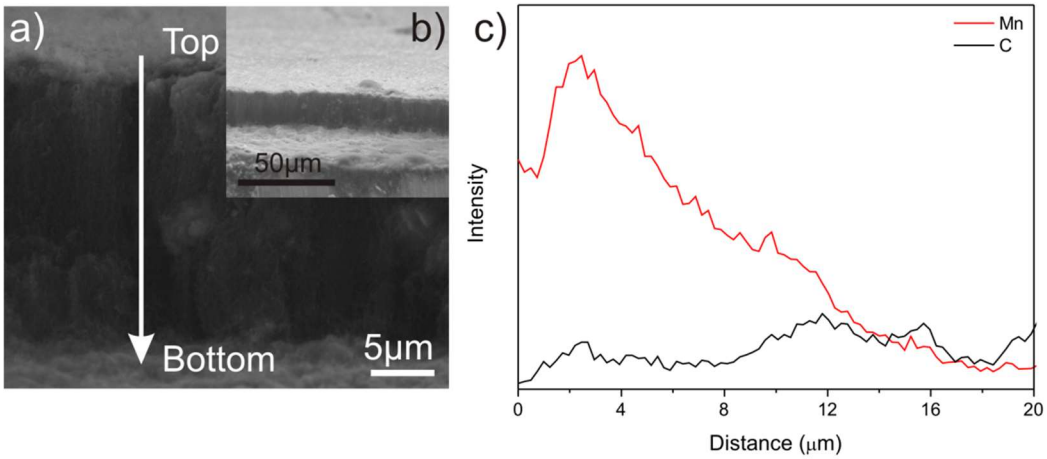

Figure V.8. SEM cross-section images (a,b) and corresponding EDS line scan profile (b) of the VACNTs/Mn_3O_4 nanocomposite after 600 ALD cycles. The inset (b) is a low magnified SEM image of (a).

Finally, to confirm that the deposition conditions and the nucleation of the Mn_3O_4 do not affect the physical properties of the VACNTs, Raman spectroscopy on the coated nanotubes has been performed (Figure V.7b). The pristine VACNTs showed the typical graphitic carbon D-band peak at 1340 cm^{-1} and G-band peak at 1580 cm^{-1}; the D-band corresponding to defects and disorder in the hexagonal plane of graphite, while the G-band represents the in-plane bond-stretching motion of C sp^2 atoms [46,47]. After deposition of manganese oxide, the peaks from the pristine VACNTs are unchanged while additional peaks due to the presence of Mn_3O_4 emerged. Since no relevant changes of the shape of the D and G bands are observed, we can conclude that the CNTs were mostly unaffected by the manganese oxide ALD and in particular by the *in situ* functionalization with ozone. The peak position from the Mn_3O_4 component is slightly shifted to a lower wavenumber value compared with value obtained for Mn_3O_4 deposited on the glass substrate (Figure IV.4b). This fact is attributed to the larger Mn_3O_4 crystallite size obtained on glass substrate due to the higher number of cycles (*i.e.* 800) [34].

V.3.3. Electrochemical Properties

In our previous work [8], we were able to grow VACNTs directly on Inconel®600 as metallic current collector allowing to directly use the VACNTs as binder-free electrode for supercapacitors applications. Figure V.9a,b shows VACNTs grown on Inconel®600 imaged by SEM and corresponding cyclic voltammetry (CV) profile (Figure V.9.c). The rectangular-like CV profile reveals the electrochemical characteristic behavior of an electric double layer capacitor. In the present work, these VACNTs were used as support for the ALD of Mn_3O_4.

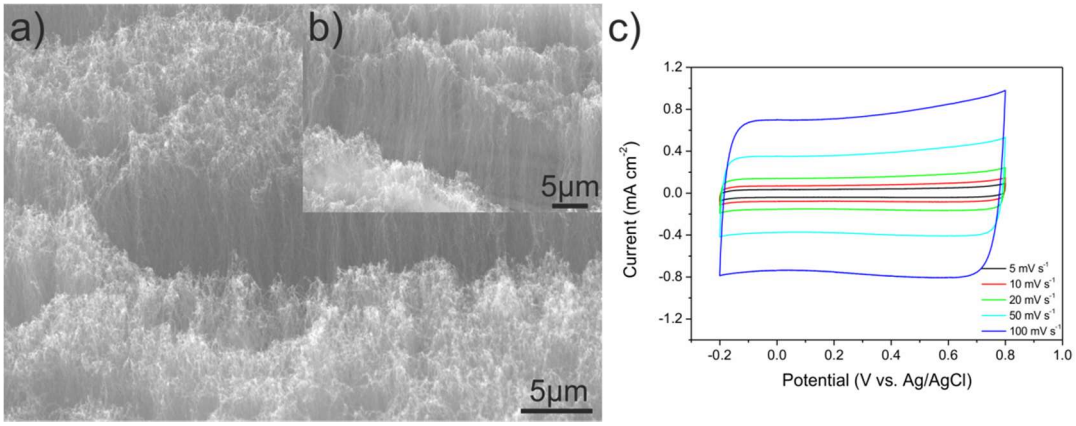

Figure V.9. SEM images (a,b) and CV curves (c) of the vertically aligned CNTs (VACNTs) grown directly on the current collector (Inconel®600).

The as-prepared VACNTs/Mn_3O_4 nanocomposite electrodes were investigated using cyclic voltammetry (CV), galvanostatic charge-discharge (GCD) and electrochemical impedance spectroscopy (EIS). Figure V.10a compares the CV curves of the pristine VACNTs and the

VACNTs/Mn_3O_4 nanocomposites electrodes after different number of Mn_3O_4 ALD cycles at a constant scan rate of 20 mV s^{-1}. The pristine VACNTs exhibited small rectangular curve corresponding to a low electrochemical double layer capacitance, while VACNTs/Mn_3O_4 nanocomposites presents a larger rectangular-like shape superimposed to redox peaks due to the combination of electrochemical double layer and redox reactions (*cf.* also Figure V.9c). The area under the CV curves increases monotonically with the increase of manganese oxide thickness; i.e. the number of ALD cycles. The capacitance increase is attributed to the Mn_3O_4 coating. Indeed, the pseudocapacitance contribution of Mn_3O_4 is supported by the redox peaks around 0.4-0.5V (Figure V.10a,b), which are attributed to the partial oxidation/reduction between Mn(III) and Mn(IV) and consistent with the Pourbaix diagrams [48].

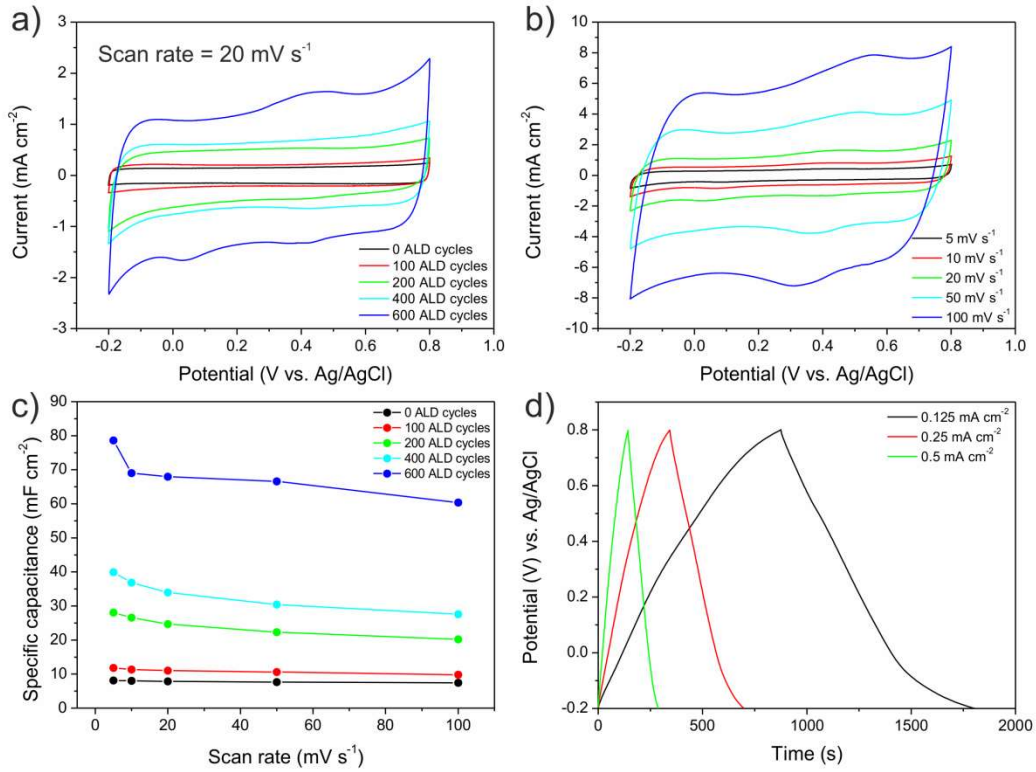

Figure V.10. CV curves (a) of the pristine VACNTs (denoted here, as 0 ALD cycles) and the VACNTs/Mn_3O_4 nanocomposites electrodes at a constant scan rate of 20 mV s^{-1}. CV curves (b) of VACNTs/Mn_3O_4 electrode after 600 ALD cycles at different scan rates. Variation of the specific capacitance (c) of the VACNTs/Mn_3O_4 electrodes after different number of ALD cycles as a function of the scan rate. Galvanostatic charge-discharge curves (d) of VACNTs/Mn_3O_4 electrode after 600 ALD cycles at different current densities, without any obvious IR drop at the beginning of the discharge curve.

The sample coated with 600 Mn_3O_4 ALD cycles was chosen for further studies because it exhibited the highest specific capacitance. The load of carbon and Mn_3O_4 for such electrode was estimated by weight difference to be around 0.35 and 0.57 mg, respectively. The pseudocapacitance contributions in CV curves recorded at various scan rates (Figure

V.10b) shift and broaden because of the increase in electrode resistance, which is characteristic of pseudocapacitive materials [49]. Additionally, the symmetric shape and the instant response upon voltage reversal indicate that surface reactions are highly reversible and very fast, as also demonstrated by the quasi-linear dependence of the capacitive current density with the scan rate (up to 100 mV s^{-1}) (Figure V.11).

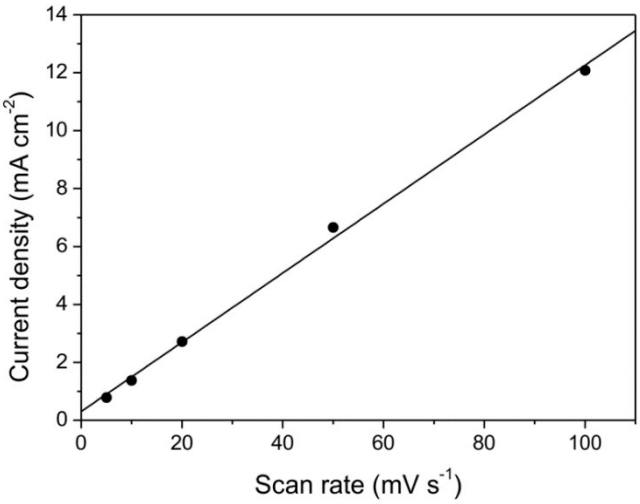

Figure V.11. Dependence of capacitive current density on the scan rate of the VACNTs/Mn_3O_4 electrode, after 600 ALD cycles.

The specific capacitances of the as-prepared electrodes at various scan rates are plotted in Figure V.10c. The highest value of 78.62 mF cm^{-2} is found at lowest scan rate of 5 mV s^{-1} for the thicker Mn_3O_4 coating. By increasing the scan rate the specific capacitance only slightly decrease, indeed the VACNTs/Mn_3O_4 still delivers a significant specific capacitance of 60.38 mF cm^{-2} at a scan rate of 100 mV s^{-1}.

Galvanostatic charge/discharge (GCD) analysis was also conducted at different current densities (Figure V.10d). The shape of the discharge curves shows features of both electrochemical double layer and pseudocapacitance. Pseudocapacitive contributions from redox active surface species can cause a deviation from linearity in charge discharge curves [50]. With increasing current density a decrease in specific capacitance of the electrode is observed, since the time available for the electrolyte ions to access the electrode material is lower. The specific capacitance obtained from GCD curves was 117.10, 89.57 and 78.13 mF cm^{-2} at current densities of 0.125, 0.25 and 0.50 mA cm^{-2}, respectively.

Cyclic charge-discharge tests were carried up to 600 cycles at 0.50 mA cm^{-2} to evaluate the electrode stability (Figure V.12a). During the first 300 cycles, the specific capacitance decrease slightly but then is maintained for the next 300 cycles. The inset shows four galvanostatic charge-discharge cycles at a current density of 0.50 mA cm^{-2} exhibiting

almost identical triangular curves. These results highlight the good cycle stability of the binder-free VACNTs/Mn_3O_4 electrodes.

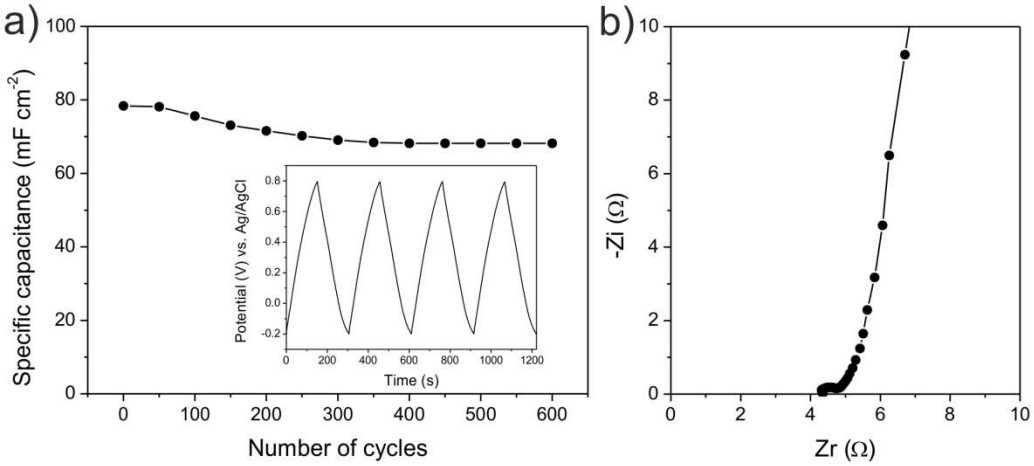

Figure V.12. Cycling stability test (a) and (b) Nyquist plot of VACNTs/Mn_3O_4 nanocomposite after 600 ALD cycles. The inset of (a) shows the repeated charge-discharge curves.

Nyquist plot exhibited a semicircle over the high frequency range due to the presence of redox reactions, followed by an almost vertical line along the imaginary axis in the low frequency region, which is associated to the capacitive behavior of the electrode (Figure V.12b). It should be mentioned that the observed small diameter of the semicircle is related to a low charge transfer resistance, which can be attributed to the good electrode-electrolyte contact [51]. The equivalent series resistance (ESR) obtained from the intersection of the Nyquist plot at x-axis is estimated to around 4.4 Ω. This relatively low value is a reflection of the vertically aligned geometry of the CNTs, and the good contact between the CNTs and the Inconel®600 substrate.

V.3.4. Influence of the VACNTs conductive network (VACNTs geometry) on the electrochemical behavior of VACNTs/Mn_3O_4 nanocomposite

To further understand the contribution of the VACNTs conductive network into the electrochemical behavior CV measurements of pristine VACNTs, VACNTs/Mn_3O_4 nanocomposite and Mn_3O_4 thin film electrodes coated with 100 ALD cycles of Mn_3O_4 respectively, all supported on 1x1 cm^2 Inconel®600 substrate, were carried out. The results reveal that the contribution of pure Mn_3O_4 thin film is much lower when compared with pristine VACNTs and VACNTs/Mn_3O_4 nanocomposite (Figure V.13). Since the specific capacitance is proportional to the area under the CV. It is clearly evident that the VACNTs/Mn_3O_4 nanocomposite electrode exhibits an increased current response as compared to the pristine VACNTs and Mn_3O_4 thin film deposited directly on the Inconel®600 electrode. This improvement on the electrochemical response may be attributed to the 3D VACNTs/Mn_3O_4 architecture electrode whose surface area is much

larger than the planar Mn_3O_4 thin film supported on the current collector. Therefore, it can be concluded that the VACNTs serves as a conductive network to facilitate the charge transport during charging and discharging process of the Mn_3O_4 coating. Furthermore, these results also suggest that, the VACNTs on Inconel®600 substrate, which can be directly used as 3D-nanostructured current collectors to support a coating of pseudocapacitive material, are superior to conventional planar metallic foils. Since each nanotube is connected directly with current collector (Inconel®600 substrate) can not only serve as the support for the pseudocapacitive material but also provide direct 1D pathway for electron transport, more favorable for the enhancement of the overall electrochemical performance.

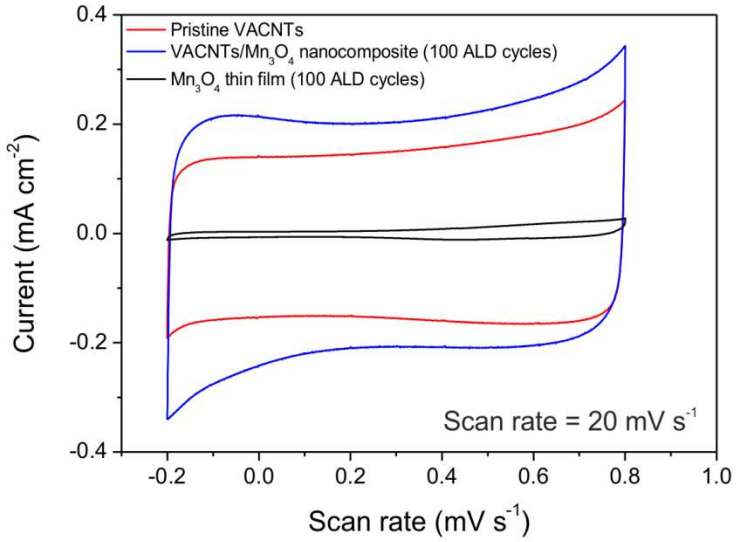

Figure V.13. CV curves of the pristine VACNTs (denoted here, as 0 ALD cycles), VACNTs/Mn_3O_4 nanocomposite (100 ALD cycles) and Mn_3O_4 thin film (100 ALD cycles) electrodes, at a constant scan rate of 20 mV s^{-1}. The CV curves at scan rate of 20 mV s^{-1} show a near symmetric rectangular shape, demonstrating the typical capacitive behavior. The specific capacitance for each electrode is 7.85 mF cm^{-2} (pristine VACNTs), 11.0 mF cm^{-2} (VACNTs/Mn_3O_4 nanocomposite) and 1.06 mF cm^{-2} (Mn_3O_4 thin film).

Based on the electrochemistry study, it can be concluded that the conformal and uniform Mn_3O_4 ALD coatings introduced pseudocapacitive charge storage properties to the VACNTs based electrodes. Moreover, the vertically aligned array facilitates an effective electrolyte penetration creating high metal oxide-electrolyte interfaces available for surface reactions. Finally, the high conductivity of the CNTs and good contact to the current collector allow for the charges to be transported easily from the top to the bottom of the electrode and transferred to the collector.

V.3.5. VACNTs/Mn_3O_4 nanocomposite after the electrochemical measurements

The surface morphology of the VACNTs/Mn_3O_4 nanocomposite electrode, coated with 600 cycles of Mn_3O_4 was characterized after the electrochemical measurements. Figure

V.14a reveals the surface morphology overview of the electrode; it seems like an arid land, which has lots of blocks. Although, the CNTs remained attached to the support this observation also suggests that the CNTs are mechanically well coupled to the support. The high magnified SEM image (Figure V.14b) shows a hierarchically structured Mn_3O_4 wrinkle nanomesh (or nanowhiskers) attached upon the sidewalls of the nanotubes, which is in good agreement with the TEM result (Figure VI.14d). To evaluate the physical properties of the coated VACNTs after electrochemistry measurements, Raman spectroscopy has been carried out and reported in Figure VI.14e. No relevant changes of the shape of the typical D band and G band are observed. Therefore, we can conclude that the CNTs were mostly unaffected by the electrochemical measurements. Although, one additional peak at 991 cm^{-1} has emerged which correspond to the S-O stretching vibration from SO_4^{2-}. It is also possible to observe the decrease of the Mn_3O_4 component intensity after cycling (green) compared with Mn_3O_4 component intensity before cycling (red). These findings are mainly related to the presence Na_2SO_4 aqueous electrolyte on the CNTs surface. Based on these results, we found that the CNTs not only provide a good conductive network but also a good supporting matrix to avoid the Mn_3O_4 material loss during the cycling test. All these features contribute to the excellent electrochemical behavior of the VACNTs/Mn_3O_4 nanocomposite electrodes.

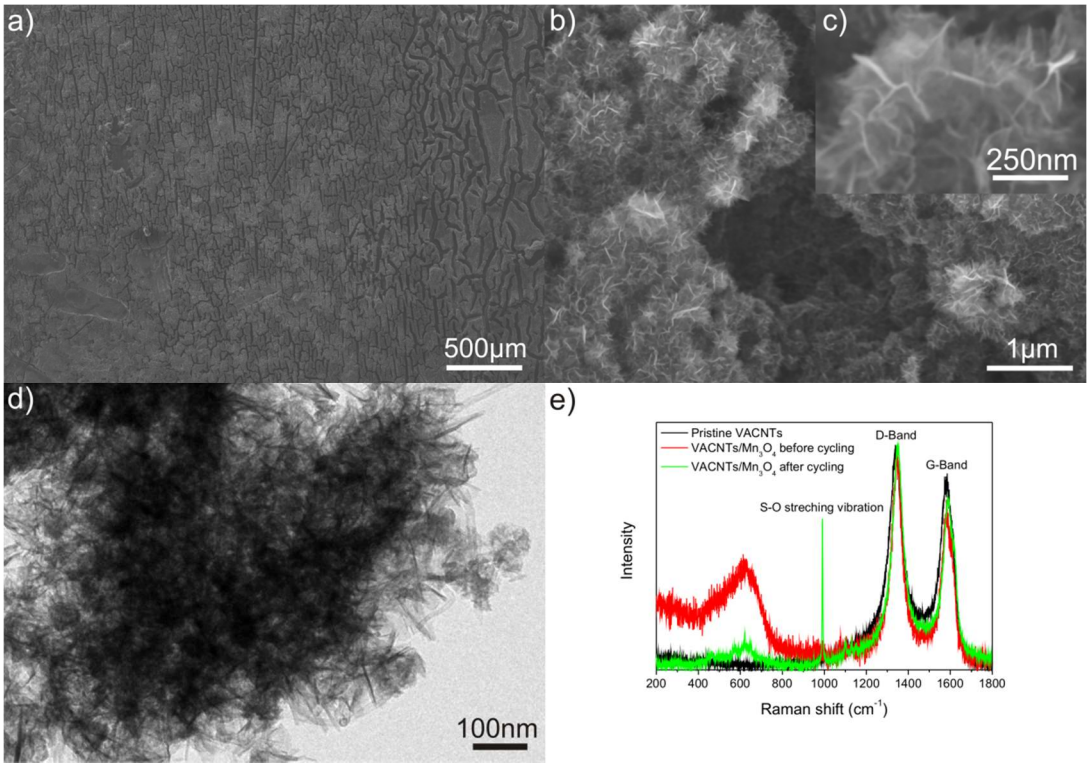

Figure V.14. Top view low and high magnified SEM image (a,b), the inset (c) is a close up view SEM image of (b) and an overview TEM image of the winkle nanomesh (d) of the VACNTs/Mn_3O_4 nanocomposite electrode after 600 ALD cycles. Raman spectra (e) of the pristine VACNTs (black), VACNTs/Mn_3O_4 nanocomposite coated with 600 cycles of Mn_3O_4 before cycling (red) and after cycling (green) i.e. after electrochemical measurements.

V.4. Conclusions

In this work, we have reported a novel self-limiting ALD process for the growth of Mn_3O_4, over a large temperature window using methylcyclopentadienyl manganese tricarbonyl ($MeCpMn(I)(CO)_3$) and ozone. This process exhibits saturation at short dose times (0.5 s for $MeCpMn(I)(CO)_3$ and 0.2 s for ozone), a nominal GPC of 0.045 nm and the possibility of conformally coating high aspect ratio 3D structures. No additional *ex situ* functionalization step was necessary to ensure the coating of the CNTs due to the *in situ* surface functionalization by ozone generating the required anchoring species for nucleating the Mn_3O_4 ALD film. When tested as binder-free supercapacitor electrode materials, the VACNTs/Mn_3O_4 nanocomposites on Inconel®600 exhibited an enhanced capacitive performance as compared to pristine VACNTs. The specific capacitance increased with the increase of the thickness of the coating (i.e. number of ALD cycles) due to a synergy between the components in the nanocomposite and an effective utilization of the active materials. All in all, the combination of the VACNTs grown on conductive Inconel®600 substrates and the ALD of metal oxides using ozone, as oxygen source and for the functionalization of the CNTs, is a very promising approach for fabricating binder-free electrodes for a variety of applications.

References

[1] P. Simon, Y. Gogotsi, *Nat. Mater.* **2008**, *7*, 845.

[2] P. Simon, Y. Gogotsi, B. Dunn, *Science* **2014**, *343*, 1210.

[3] T. Brousse, D. Belanger, J.W. Long, *J. Electrochem. Soc.* **2015**, *162*, 5185.

[4] B.E. Conway, in *Electrochemical Supercapacitors: Scientific Fundamentals and Technology Applications*, Klumer Academic/Plenum Publishers, New-York **1999**.

[5] G. Wang, L. Zhang, J. Zhang, *Chem. Soc. Rev.* **2012**, *41*, 797.

[6] O. Ghodbane, J.L. Pascal, B. Fraisse, F. Favier, *ACS Appl. Mater. Interfaces*, **2010**, *2*, 3493.

[7] S.W. Lee, J. Kim, S. Chen, P.T. Hammond, Y. Shao-Horn, *ACS Nano* **2010**, *4*, 3889.

[8] R.M. Silva, A.C. Bastos, F.J. Oliveira, D.E. Conte, Y.F. Fan, N. Pinna R.F. Silva, *J. Mater. Chem. A* **2015**, *3*, 17804.

[9] C. Guan, X. Xia, N. Meng, Z. Zeng, Z. Cao, C. Soci, H. Zhang, H.J. Fan, *Energy Environ. Sci.* **2012**, *5*, 9085.

[10] M. Knez, K. Nielsch, L. Niinistö, *Adv. Mater.* **2007**, *19*, 3425.

[11] C. Marichy, M. Bechelany, N. Pinna, *Adv. Mater.* **2012**, *24*, 1017.

[12] C. Marichy, N. Pinna, *Coord. Chem. Rev.* **2013**, *257*, 3232.

[13] R.L. Puurunen, *J. Appl. Phys.* **2005**, *97*, 121301.

[14] M. George, *Chem. Rev.* **2010**, *110*, 111.

[15] X. Wang, G. Yushin, *Energy Environ. Sci.* **2015**, *8*, 1889.

[16] B.B. Burton, F.H. Fabreguette, S.M. George, *Thin Solid Films* **2009**, *517*, 5658.

[17] K.L. Pickrahn, S.W. Park, Y. Gorlin, H.B.R. Lee, T.F. Jaramillo, S.F. Bent, *Adv. Energy Mater.* **2012**, *2*, 1269.

[18] N.C. Strandwitz, D.J. Comstock, R.L. Grimm, A.C. Nichols-Nielander, J. Elam, N. S. Lewis, *J. Phys. Chem. C* **2013**, *117*, 4931.

[19] O. Nilsen, H. Fjellvåg, A. Kjekshus, *Thin Solid Films* **2003**, *444*, 44.

[20] O. Nilsen, S. Foss, H. Fjellvåg, A. Kjekshus, *Thin Solid Films* **2004**, *468*, 65.

[21] F. Mattelaer, P.M. Vereecken, J.Dendooven, C.Detavernier, *Chem. Mater.* **2015**, *27*, 3628.

[22] Y.W. Li, Q. Qiao, J.Z. Zhang, Z.G. Hu, J.H. Chu, *Thin Solid Films* **2015**, *574*, 115.

[23] M. Bouman, X. Qin V. Doan, B.L.D. Groven, F. Zaera, *Organometallics* **2014**, *33*, 5308.

[24] F. Zeara, *J. Phys. Chem. Lett.* **2012**, *3*, 1301.

[25] M.P. Nguyen, Y. Sutou, J. Koike, *Thin Solid Films* **2015**, *580*, 56.

[26] H. Sun, F. Zeara, *J. Phys. Chem. C* **2012**, *116*, 23585.

[27] S. Wen-bin, K. Durose, A.W. Brinkman, B.K. Tanner, *Mater. Chem. Phys.* **1997**, *47*, 75.

[28] A.R. Merrit, R. Rajagopalan, J.D. Carter, *Thin Solid Films* **2014**, *556*, 28.

[29] H. Sun, X. Qin, F. Zeara, *J. Phys. Chem. Lett.* **2011**, *2*, 2525.

[30] V. Miikkulainen, M. Leskelä, M. Ritala, R.L. Puurunen, *J. Appl. Phys.* **2013**, *113*, 021301.

[31] K. Peng, L. Liu, H. Li, H. Mayer, Z. Zhang, *Carbon* **2011**, *49*, 70.

[32] A. Lushington, J. Liu, Y. Tang, R. Li, X. Sun, *J. Vac. Sci Technol. A* **2014**, *32*, 01A124.

[33] X. Tong, X. Guo, O. Moutanabbir, X. Ao, E. Pippel, L. Zhang, M. Knez, *Small* **2012**, *8*, 3390.

[34] J. Zuo, C. Xu, Y. Liu, Y. Qian, *Nanostruct. Mater.* **1998**, *10*, 1331.

[35] C. M. Julien, M. Massot, C. C. Poinsignon, *Spectrochim. Acta, Part A* **2004**, *60*, 689.

[36] G. An, Ping Yu, M. Xiao, Z. Liu, Z. Miao, K. Ding, L. Mao, *Nanotechnology* **2008**, *19*, 275709.

[37] J.W. Lee, A.S. Hall, J.D. Kim, T.E. Mallouk, *Chem. Mater.* **2012**, *24*, 1158.

[38] M. Oku, K. Hirokawa S. Ikeda, *J. Elec. Spec. and Relat. Phenom.* **1975**, *7*, *465.*

[39] E.S. Ilton, J.E. Post, P.J. Heaney, F.T. Ling, S.N. Kerisit, *App. Surf. Science* **2016**, *366*, 475.

[40] K.L. Stano, M. Carroll, R. Padbury, M. McCord, J.S. Jur, P.D. Bradford, *ACS Appl. Mater. Interfaces* **2014**, *6*, 19135.

[41] H.C.M. Knoops, J.W. Elam, J.A. Libera, W.M.M. Kessels, *Chem. Mater.* **2011**, *23*, 2381.

[42] S. T. Oyama, *Catal. Rev – Sci. Eng.* **2000**, *42*, 279.

[43] B. Dhandapani, S.T. Oyama, *Appl. Catal., B* **1997**, *11*, 129.

[44] W. Li, G.V. Gibbs, S.T. Oyama, *J. Am. Chem. Soc.* **1998**, *120*, 9041.

[45] H. Einaga, M. Harada, A.i Ogata, *Catal Lett* **2009**, *129*, 422.

[46] F. Tuinstra, *J. Chem. Phys.* **1970**, *53*, 1126.

[47] M.S. Dresselhaus, A. Jorio, M. Hofmann, G. Dresselhaus, R. Satio, *Nano Lett.* **2010**, *10*, 751.

[48] M. Pourbaix, in *Atlas of Electrochemical Equilibria in Aqueous Solutions, National Association of Corrosion Engineers,* Houston, TX, **1996**.

[49] Z. Yin. Y. Chen, Y. Zhao, C. Li, C. Zhu, X. Zhang, *J. Mater. Chem. A* **2015**, *3*, 22750.

[50] S. Bose, T. Kuila, A.K. Mishra, R. Rajasekar, N.H. Kim, J.H. Lee, *J. Mater. Chem.* **2012**, *22*, 767.

[51] S. Boukalfa, K. Evanoff, G. Yushin, *Energy Environ. Sci.* **2012**, *5*, 6872.

Chapter VI

Chapter preface

The catalyst-free growth of pure vertically aligned carbon nanotubes directly on Inconel®600 described in Chapter IV was also extended to nitrogen doped carbon nanotubes (N-CNTs). This chapter describes a comparative study about the electrochemical properties of such doped CNTs and the pure-carbon nanotubes, both coated with manganese oxide as electrode materials. The atomic layer deposition parameters of manganese oxide (Mn_3O_4) were kept the same as those used in Chapter V. A tentative title for a manuscript to be submitted for a SCI journal is:

"Electrochemical performance of nanocomposite electrodes formed by coating nitrogen doped and pure carbon nanotubes arrays with manganese oxide: a comparative study"

R.M. Silva, G. Clavel, A.V. Girão, Y. Fan, R.F. Silva, N. Pinna, **2016**, *(in preparation)*

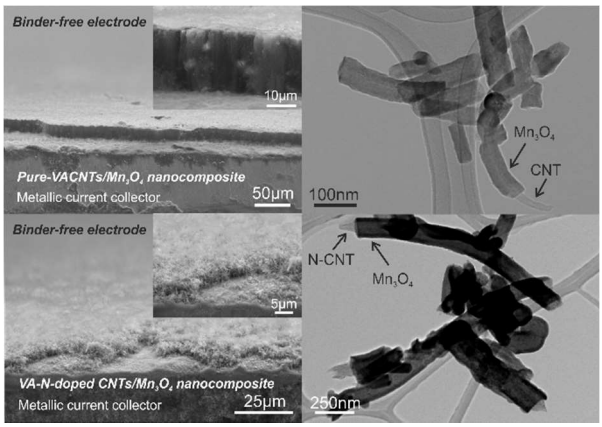

This manuscript received the contributions from G. Clavel, A.V. Girão and Y. Fan in terms of electron microscopy and electrochemical measurements and interpretation, respectively.

Electrochemical performance of nanocomposite electrodes formed by coating nitrogen doped- and pure-carbon nanotubes arrays with manganese oxide: a comparative study

Abstract

Direct growth of vertically aligned nitrogen doped carbon nanotubes arrays on metallic conductive substrate (Inconel®600) using the thermal chemical vapor deposition process is reported. The as-prepared nitrogen doped carbon nanotubes arrays were coated with manganese oxide by atomic layer deposition, in order to fabricate a tree-dimensional (3D) hybrid nanostructure array for application as binder-free electrode. Electron microscopy studies confirm that the nanotubes were conformally coated with manganese oxide (Mn_3O_4).

The electrochemical properties of the as-prepared nanocomposite electrodes were studied using cyclic voltammetry, galvanostatic charge and discharge cycling in 1M Na_2SO_4 aqueous electrolyte. A comparative study of the electrochemical properties of the Mn_3O_4 coated pure-carbon and N-doped nanotubes arrays with was carried out in order to further understand not only the effect of the nitrogen doping on the electrochemical performance of such nanocomposites but also on the cycling stability. The results demonstrate that both architectures have great potential for supercapacitors applications, especially when combined with pseudocapacitive metal oxides such is manganese oxide.

VI.1. Introduction

Pure vertically aligned carbon nanotubes (pure-VACNTs) as well as nitrogen doped vertically aligned carbon nanotubes (VA-N-doped CNTs) have been shown promising characteristics in electrochemical capacitors applications as electrode material due to their attractive properties like high surface area and highly ordered geometry [1-4]. As such, applications demand considerable effort to have nanotubes arrays grown directly on metallic conductive substrates, as a result a binder free electrode is obtained [5]. This approach simplifies the conventional electrode preparation involving several fabrication steps, and binder additives. For hypothesis, in supercapacitors, the VA-N-doped CNTs could give rise to more interesting electrochemical performance as compared to the pure-VACNTs, by the formation of C/N sites with electrochemical activity promoted by the charge profile induced in the graphitic network through the electronegativity of the nitrogen doping atoms, which might ease the interaction with the electrolyte. On the basis of the energy storage mechanism, it is possible to separate the contribution of a pure electrostatic attraction in the electrode/electrolyte interface and of the pseudocapacitance properties due to the surface functionalization of the carbon nanotubes. Pseudocapacitance contribution due to nitrogen is commonly recognized by non-rectangular shape of cyclic

voltammetry (CV) curves in aqueous electrolyte solution [6]. VA-N-doped CNTs are also an attractive electrode material for the elaboration of nanocomposites by using carbon nanotubes as a support not only increases the effective utilization of the active materials such as transition metal oxides, but also improves the electrical conductivity of the nanocomposite materials. As matter of fact, the presence of nitrogen atoms inside the graphitic network structure seems to enhance the density of the anchorage sites for depositing metal oxides or other active phase onto the nanotube surface [7]. Therefore, the development of simple methods to direct growth of VA-N-doped CNTs on a conductive substrate is of great interest in supercapacitors applications. Generally, there are two synthetic pathways to growth N-doped CNTs. One involves post-treatment of carbon nanotubes with reactive nitrogen sources, such as urea, nitric acid, or especially ammonia [8]. The other way is the chemical vapor deposition of nitrogen and carbon containing precursors, such as ammonia and acetylene, by which an *in situ* incorporation of the nitrogen atoms into the forming graphitic network becomes possible [9]. As a result, the incorporation of this heteroatom dopant into the graphitic network changes the internal structure of the CNTs into bamboo-like structures with defined compartments. This type of morphology differs notoriously from pure CNTs, which exhibit tubular structures with hollow core. Particularly, the morphology changes in the N-doped CNTs caused by the N-doping create surface defect sites and consequently breaks down the chemically inert nature of the pure-CNTs making them chemically active [2].

In the present work, Inconel®600 metallic substrates are used as alternative substrates to direct growth of VA-N-doped CNTs without additional catalyst or processing. As matter of fact, randomly oriented N-doped CNTs have already synthesized on nickel substrates from a single precursor (i.e. pyrolysis by monoethanolamine) by TCVD [10].

The as-prepared VA-N-doped CNTs were used as support for the deposition of manganese oxide by atomic layer deposition (ALD) in order to fabricate VA-N-doped CNTs/Mn_3O_4 nanocomposite electrodes as a binder-free electrode for supercapacitors applications. Particular attention is devoted to the morphological characterization of the VA-N-doped CNTs as well as VA-N-doped CNTs/Mn_3O_4 nanocomposite.

Finally, we comparatively investigated the electrochemical properties of VACNTs/Mn_3O_4 and VA-N-doped CNTs/Mn_3O_4 nanocomposites electrodes as well as the uncoated VACNTs and uncoated VA-N-doped CNTs electrodes for comparison purpose. The electrochemical behavior of the different electrodes materials was assessed using cyclic voltammetry (CV), galvanostatic charge-discharge (GCD) and electrochemical impedance spectroscopy (EIS) in aqueous 1M Na_2SO_4 as electrolyte. It was found that the VACNTs exhibited a better electrochemical performance when compared with the VA-N-CNTs in this specific configuration of binder-free electrode design. This difference in performance can be due to the size-effect of the nanotubes arrays either as in length or in outer diameter. In addition, the results suggest that the obtained nanostructured materials are promising candidates for binder-free electrodes in electrochemical capacitors applications.

VI.2. Experimental Section

VI.2.1. Sample preparation

The vertically aligned nitrogen doped carbon nanotube (VA-N-doped CNT) arrays were grown by thermal chemical vapor deposition (TCVD) technique directly on 1x1 cm^2 pretreated Inconel®600 metallic substrates and also on silicon buffered substrate from a mixture of acetylene and ammonia (C_2H_2 (10 sccm)/NH_3 (90 sccm)) at 825 °C using argon (Ar) as a carrier gas. In order to study the N-doping effect, pure VACNTs samples were also grown from a mixture of acetylene and hydrogen (C_2H_2 (10 sccm)/H_2 (100sccm)) at 650 °C using argon (Ar) as a carrier gas. Additional details about the TCVD CNTs growth process can be found in our previous works [9,11]. The growth period was 15 min for all samples at atmospheric pressure. After growth, the samples were cooled down to room temperature. Manganese oxide (Mn_3O_4) was deposited on as-prepared VA-N-doped CNT and pure-VACNTs arrays using an ARRADIANCE GEMStar-6 atomic layer deposition (ALD) reactor working in exposure mode at 200 ºC from methylcyclopentadienyl manganese tricarbonyl ($MeCpMn(I)(CO)_3$) as metal precursor and ozone (O_3). In a typical process, each ALD cycle consisted of 0.5s $MeCpMn(I)(CO)_3$ pulse, 30 s of residence time, 20 s Ar purge, 1.0s O_3 pulse, 20 s of residence time and 20 s Ar purge. The delivery lines of the circuit were heated to 130 °C to prevent the precursors from condensation throughout the deposition. More details about the ALD of Mn_3O_4 deposition can be found in our previous work [12]. Several samples, with 600 ALD cycles, were prepared.

VI.2.2. Sample characterization

Structural and morphological properties of pure-VACNTs/Mn_3O_4 and VA-N-doped CNTs/Mn_3O_4 nanocomposites were characterized by scanning electron microscopy (SEM, Hitachi SU70 microscope). Raman spectroscopy (Jobin Yvon T64000) was carried out at a 532 nm excitation wavelength. The samples were also investigated by transmission electron microscopy (TEM) and scanning transmission electron microscopy (STEM) using Hitachi H9000 LaB_6 and JEOL JEM-2200FS microscopes, respectively, operated at 200 kV. Energy electron loss spectroscopy (EELS) experiments were carried out in the image mode with a JEOL JEM-2200FS TEM equipped with an Omega imaging filter system. The samples for TEM and STEM measurements were prepared by dry adhesion of the CNTs to a holey carbon film supported on a copper grid.

The electrochemical measurements were performed using a Bio-Logic VMP3 Potentiostat-Galvanostat (Science Instruments). The experiments were conducted in a three-electrode electrochemical set-up, where the pure-VACNTs/Mn_3O_4 and VA-N-doped CNTs/Mn_3O_4 (1x1 cm^2) were used as the working electrode, with platinum foil as the counter electrode and a standard silver/silver chloride electrode (Ag/AgCl) as the reference electrode. The electrolyte (1M Na_2SO_4) was prepared from Na_2SO_4 (Sigma Aldrich, 99.0%) and Millipore water. The areal capacitance (specific capacitance) was calculated using the area of the

electrode exposed to the electrolyte during the electrochemical measurements. This area was 1 cm^2. From the cyclic voltammetry (CV) measurements, the specific capacitance *(C_{sp})* of the electrodes can be evaluated using the following equation (1):

$$C_{sp} = \frac{\int I(E)dE}{2v(E_2 - E_1)A} \qquad \text{Equation (1)}$$

where C_{sp} is the specific capacitance in mF cm^{-2}, *I(E)* is the instantaneous current in A, *v* is the scan rate in V s^{-1}, *(E_2-E_1)* is the potential range in V and *A* is the electrode area in cm^2. Therefore, the average C_{sp} was obtained by integrating positive and negative current over the CV curves. The CV curves were recorded with the samples that were first stabilized by cycling 20 times at scan of 20 mV s^{-1}. The C_{sp} was also estimated from the galvanostatic charge and discharge (GCD) cycling according to the following equation (2):

$$C_{sp} = \frac{I\Delta t}{\Delta EA} \qquad \text{Equation (2)}$$

where *I* refers to discharge current in A, *Δt* represents the discharge time in s, *A* is the electrode area in cm^2 and *ΔE* is the potential range in V. Electrochemical impedance spectroscopy (EIS) studies were carried out in the frequency region from 0.01 to 100,000 Hz with the test signal amplitude of 5 mV.

VI.3. Results and discussion

VI.3.1. Growth of VA-N-doped CNTs on Inconel substrate

The growth of vertically aligned nitrogen doped carbon nanotubes (VA-N-doped CNTs) by thermal chemical vapor deposition (TCVD) followed our previous reports [9,11]. In order to form the nanometer sized catalyst particles on the substrate, the heat treated Inconel®600 substrate (Figure VI.1a) was pretreated by thermal annealing inside of the TCVD reactor at 825 ºC under an atmosphere of: (i) Ar for 5 min and (ii) Ar/H_2 mixture for 2 min until the surface of the substrate was transformed into nanoparticles (Figure VI.1b). After the formation of the nanometer sized catalyst particles, a mixture of Ar/NH_3/C_2H_2 was used to grow the VA-N-doped CNTs at 825 ºC for 15 min.

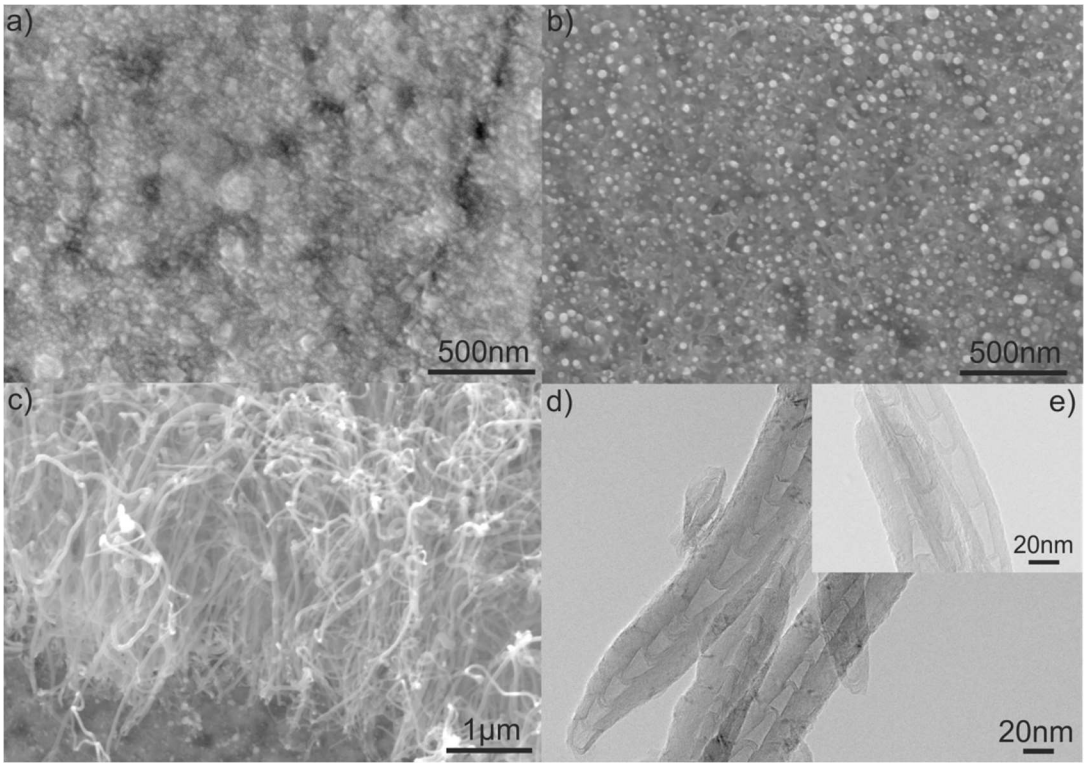

Figure VI.1. Top view SEM image of heat treated i.e., oxidized (a) and thermal annealed (b) Inconel®600 surface prior to the nanotubes growth step. Tilted SEM image (c) and TEM images (d,e) of the N-doped CNTs.

As seen from the morphology of the outer surface (Figure VI.1b), there are significant differences between the oxidized surface and the thermal annealed surface prior to the N-doped CNTs growth. It is clearly seen the formation of nanometer sized particles with a diameter size range of 20-100 nm. In our previous work [11], it was found that these catalyst particles consist mainly of iron (Fe). On the other hand, Figure VI.1c shows as-grown N-doped CNTs developed from the former catalyst particles with a good degree of vertical alignment.

Detailed information about the internal structure of the as-prepared N-doped CNTs was carried out with TEM analysis. The bamboo-like or herringbone type of N-doped CNTs is a typical structure that forms during the TCVD when using ammonia (NH_3) as the N source over an iron (Fe) catalyst [9]. The TEM images presented in Figure VI.1d,e show that the nanotubes are multiwalled and separated into a series of bamboo-like compartments, which confirms the influence of N introduction on the structure change of CNTs. In detail, the nanotubes presented in Figure VI.1d are composed of closely stacked graphitic cups with very small hollow core or inner compartment space while the inset (Figure VI.1e) shows the typical bamboo-like structure which consist of periodically curved graphitic layers. Furthermore, the curvature of the compartment graphitic layers is always directed to the tip.

Raman spectroscopy with 532 nm excitation wavelength was employed to investigate the degree of disorder or defects of the as-prepared N-doped CNTs on the two substrates (Inconel®600 and buffered Si). The Raman spectra for the as-prepared N-doped CNTs are plotted in Figure VI.2. This spectrum exhibits the D and G band located at 1340 and 1580 cm^{-1}, respectively typical of multiwalled CNTs. This observation is consistent with the TEM studies. The other band located at 2700 cm^{-1} is due to the second-order combination of 2D.

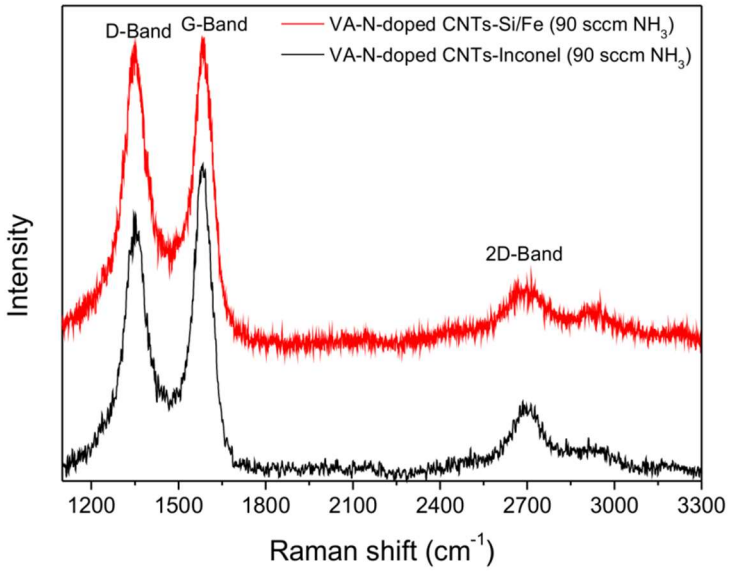

Figure VI.2. Raman spectra of VA-N-doped CNTs grown on the two substrates.

For these N-doped CNTs, the ratio of the integrated areas of the D and G bands (I_D/I_G) were calculated to be 1.15 and 1.42 for Inconel and buffered Si, respectively. Actually, there is a slightly difference in the I_D/I_G values for the N-doped CNTs grown on the two substrates. This result suggests the presence a higher degree of disorder or defects on the surface of the N-doped CNTs in the case of buffered Si as compared to those grown on Inconel substrate. The obtained results indicate that the Inconel®600 substrate provided the

suitable nucleation sites for N-doped CNTs growth coming from the morphological transformation of the substrate surface.

VI.3.2. VA-N-doped CNTs/Mn_3O_4 nanocomposite

Structural and morphology of the material significantly influences the suitability of the material for supercapacitors. The high and low-magnified SEM images (Figure VI.3a,b) show the surface morphology and vertical alignment of the as-prepared VA-N-doped CNTs/Mn_3O_4 nanocomposite supported on Inconel®600 after 600 ALD cycles. On the other hand, the energy-dispersive X-ray spectroscopy (EDS) elemental mapping investigation (Figure VI.3c) of the nanocomposite revealed that the Mn_3O_4 was homogeneously distributed over the nanotubes. From the BF-STEM and TEM images (Figure VI.3d,e), it can be seen that the nanotubes are coated with a uniform and homogeneous coating of Mn_3O_4. The BF-STEM and the high angle annular DF-STEM images (Figure VI.3f,g) taken from an individual nanotube provide direct evidence of a granular-like and conformal coating of Mn_3O_4 along the nanotube, which is seen as the darker contrast in Figure VI.3f and brighter contrast in Figure VI.3g. In the former figure the observed bright contrast regions arise from the heavier (Z-contrast) manganese atoms in Mn_3O_4. For this case, the high angle annular dark field imaging in STEM is suitable, as the contrast can be chosen such that the carbon nanotube support remains nearly invisible whilst the coating can clearly be seen. The assignment is consistent with the chemical analysis by EDS elemental mapping (Figure VI.3c). The TEM and STEM observations suggest the successful coating of the VA-N-doped CNTs by ALD process.

Electron energy loss spectroscopy (EELS) analysis performed in the TEM is also applied to analyze the elemental composition of the as-prepared nanocomposite. In Figure VI.3h an EELS spectrum collected from the N-doped CNTs coated with Mn_3O_4 (inset in Figure VI.3h). The edges of the Mn-$L_{2,3}$ peaks are located at 653.7 and 642.7 eV, while the edge of the C-*K* peak is located at 284 eV and the edge of the O-*K* peak appears at 532 eV. The observed Mn-$L_{2,3}$ peaks position is compared with those reported in the literature for Mn_3O_4 [13]. No other elements are present in the coated nanotube and this EELS result corroborates with our previous XPS studies [12] and it also confirms the interpretation of contrast variation observed in the TEM and STEM studies. In Figure VI.3i, a strong Raman band at 639.7 cm^{-1} is observed, which can be attributed to the presence of Mn_3O_4. The general similarity of the spectral features suggests that the N-doped CNTs maintain their physical properties after the Mn_3O_4 ALD deposition.

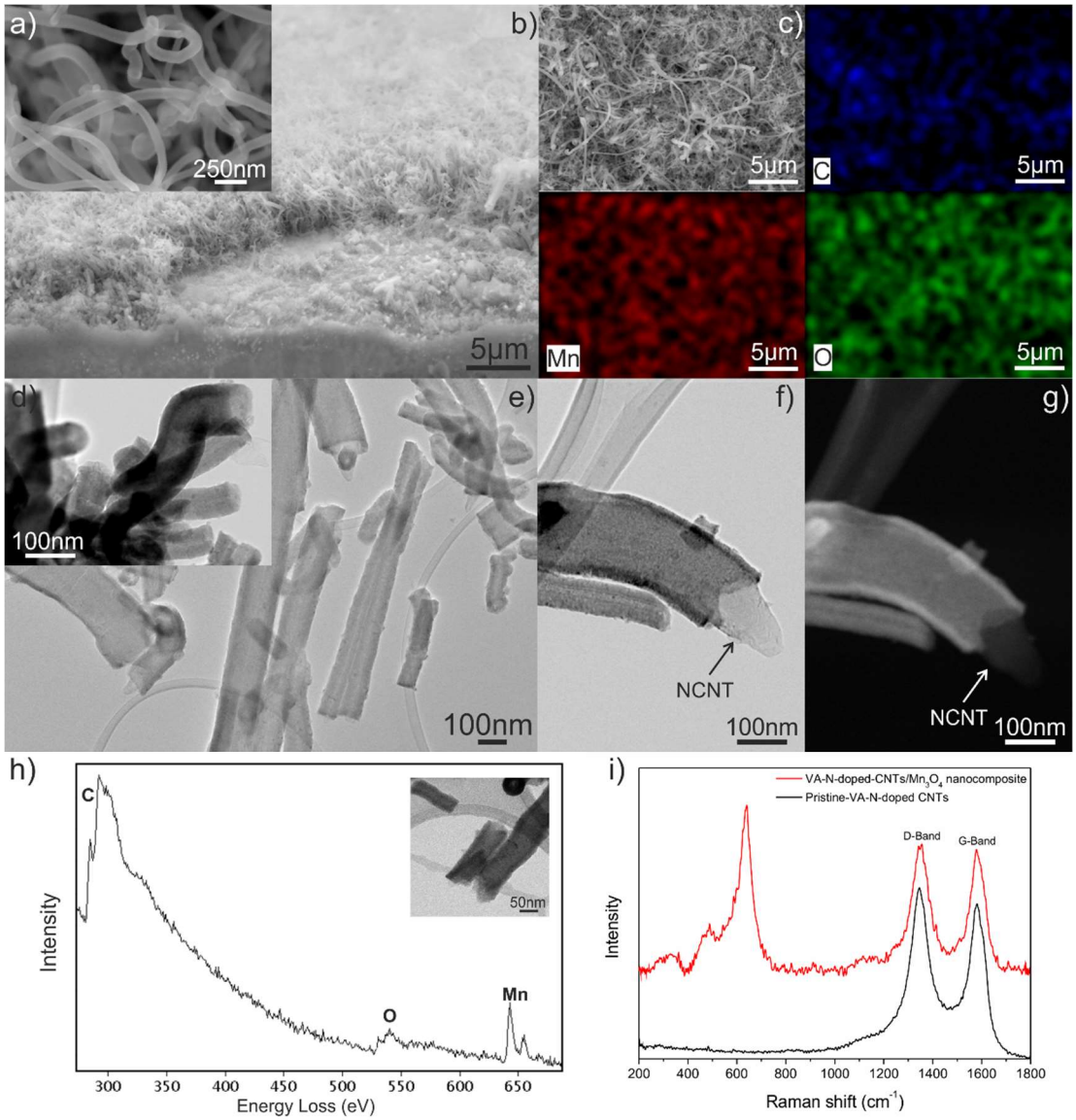

Figure VI.3. High and low-magnified side view SEM images (a,b) and low-magnified SEM image (c) of the VACNTs coated with 600 cycles of Mn_3O_4 and the corresponding EDS mapping of carbon (blue), manganese (red) and oxygen (green). BF-STEM (d) and BF-TEM images (e) of the VA-N-doped CNTs/Mn_3O_4 nanocomposite after 600 ALD cycles. BF-STEM (f) and DF-STEM (g) image recorded from N-doped CNT coated with 600 ALD cycles. The uncoated region is due to the manipulation of the sample during the TEM sample preparation and emphasizes the coating deposition. Electron energy loss spectroscopy (EELS) spectrum (h) of N-doped CNTs coated with Mn_3O_4 taken at inset region. Raman spectra (i) of the pristine (i.e. uncoated) VA-N-doped CNTs (black) and the VA-N-doped CNTs/Mn_3O_4 nanocomposite (red) after 600 ALD cycles.

VI.3.3. Electrochemical Properties

In order to further understand electrochemical properties of pure- and nitrogen doped-carbon nanotubes as electrode materials a comparative study is undertaken. Figure VI.4 shows pure-VACNTs and VA-N-doped CNTs both grown on Inconel®600 (metallic current collector) coated with Mn_3O_4 (600 ALD cycles). These nanocomposites were directly used as binder-free electrodes for supercapacitors applications. The scanning TEM (STEM) studies reveal that the Mn_3O_4 coating is uniformly distributed on the walls of the pure- (Figure VI.4e,f) and N-doped-CNTs (FigureVI.4g,h). Particularly, the high-angle annular DF-STEM images (Figure VI.4f,h) where the bright features show the Mn_3O_4. Therefore, the electrochemical performance of the VACNTs/Mn_3O_4 and VA-N-doped CNTs/Mn_3O_4 nanocomposites electrodes were investigated using cyclic voltammetry (CV), galvanostatic charge-discharge (GCD) and electrochemical impedance spectroscopy (EIS) in a three-electrode configuration. For comparison, the electrochemical behavior of uncoated VACNTs and uncoated VA-N-doped CNTs were also investigated.

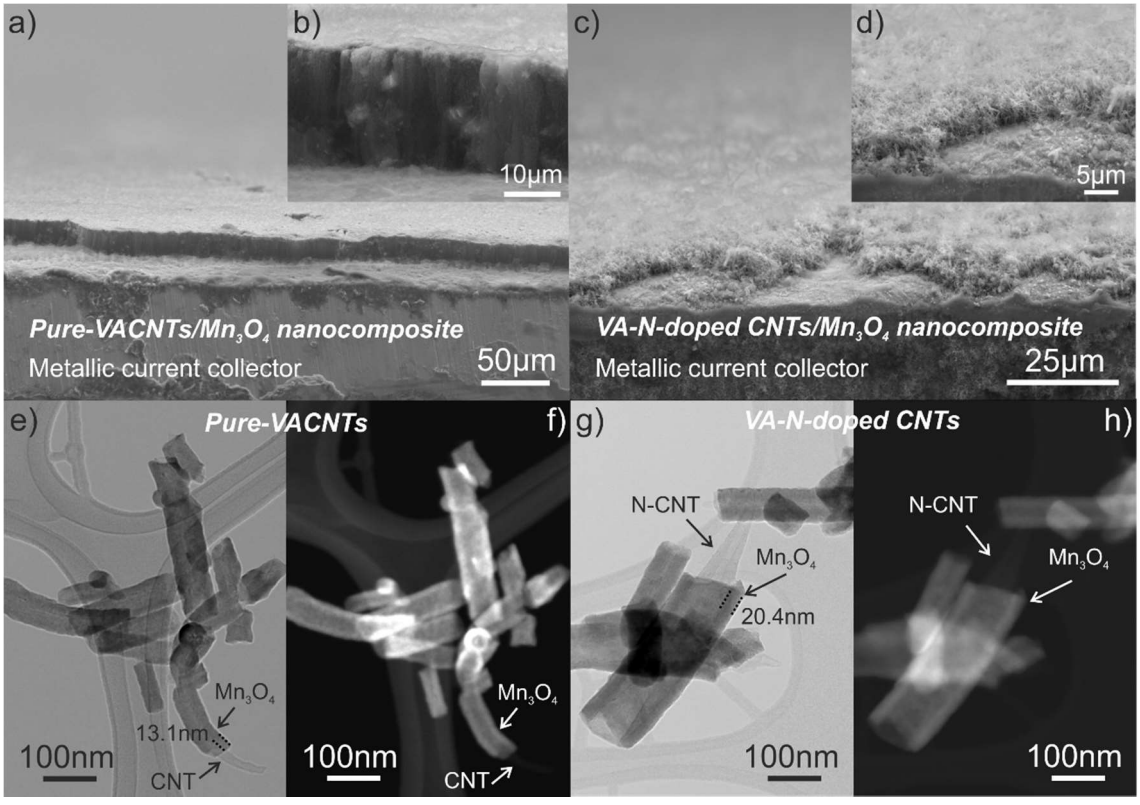

Figure VI.4. Cross-section SEM images of (a) pure VACNTs (length: 20.8 µm) and (c) VA-N-doped CNTs (length: 5.5 µm) coated with 600 cycles of Mn_3O_4 supported on Inconel®600. The insets show cross-section high-magnified SEM images of (b) VACNTs/Mn_3O_4 and (d) VA-N-doped CNTs/Mn_3O_4 nanocomposites highlighting the vertical alignment. BF-STEM (e,g) and DF-STEM (f,h) images recorded from pure- and N-doped CNTs coated with 600 ALD cycles.

Figure VI.5 compares the CV curves of the uncoated pure-VACNTs and uncoated VA-N-doped CNTs electrodes on the left panel and the VACNTs/Mn_3O_4 and VA-N-doped

CNTs/Mn_3O_4 nanocomposites electrodes (prepared at 600 ALD cycles) on the right panel, in 1M Na_2SO_4 aqueous electrolyte with potential range of -0.2 to 0.8 V. It can be seen the remarkable differences in CV curve shape between the pure-VACNTs and the VA-N-doped CNTs, either as uncoated or coated with Mn_3O_4. In detail, the uncoated VACNTs exhibited a larger rectangular curve corresponding to a superior capacitance, while VA-N-VACNTs presents a smaller rectangular-like shape in CV curve (Figure VI.5a,c). In fact, the area under the CV curves increases with scan rate. This shows that the volumetric currents are directly proportional to the scan rates of CV with negligible redox peaks indicating the typically capacitive behavior of the electric double layer capacitors (EDLCs).

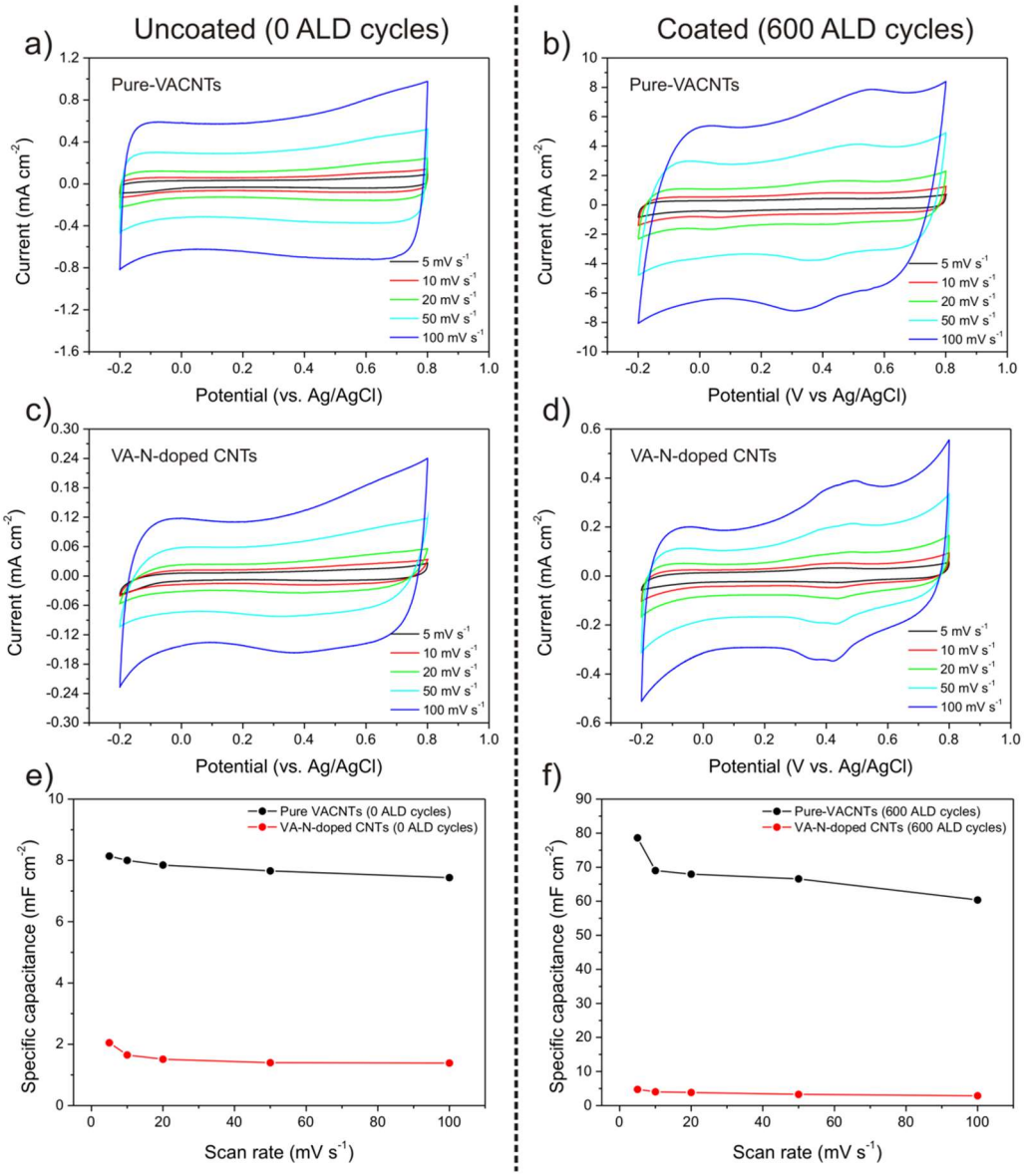

Figure VI.5. Comparison of the CV curves of (left panel) uncoated (denoted here, as 0 ALD cycles) and (right panel) coated (600 ALD cycles) VACNTs and VA-N-doped CNTs electrode. Variation of the specific capacitance of the uncoated (left panel) and the coated (right panel) pure-VACNTs and VA-N-doped CNTs electrodes with scan rate.

In the case of the coated pure-VACNTs and VA-N-doped CNTs with 600 ALD cycles the almost rectangular-like shape of the CV curves of these nanocomposites electrodes, indicates the ideal capacitance nature and the appearance of humps in the CV curves indicate that the capacitive response comes from the combination of EDLC and redox reactions, which are related to the pseudocapacitance of the Mn_3O_4. It is also possible to notice that the VACNTs/Mn_3O_4 nanocomposite electrode presents the largest integrated area resulting in a much larger capacitive current in comparison with the VA-N-doped CNTs/Mn_3O_4 nanocomposite electrode (Figure VI.5b,d). It indicated that the specific capacitance is improved resulted from the combination of the superior ELDC of the pure-VACNTs and pseudocapacitance of the Mn_3O_4. Indeed, it is possible to observe in both CV curves, a pair of redox peak around 0.4-0.5V, theses peaks may be attributed to the partial oxidation/reduction between Mn(III) and Mn(IV) which is consistent with the Pourbaix diagrams [14].

The specific capacitances of the as-prepared electrodes at various scan rates are calculated and drawn in Table VI.1. It can be also observed that the specific capacitance values decrease with the increase in scan rate Figure VI.5 e,f). This is the normal behavior of electrochemical systems. Generally, two different mechanisms have been proposed for the charge storage mechanisms of the oxide materials. One is the intercalation/deintercalation of protons or alkaline metal cations, which leads to the full utilization of the electrode material. This may be the reason for obtaining a higher specific capacitance at a lower scan rate. The second explanation relates to the surface adsorption process for a higher scan rate. This is based on the diffusion effect of the proton within the electrode materials. Hence, it is believed that part of the surface of electrode materials contributed at a high charging/discharging rate, which decreases the specific capacitance [15,16].

Table VI.1. Specific capacitance (C_{sp}) calculated from the CV curves, at different scan rates.

	Specific capacitance (C_{sp}) (mF cm^{-2})			
Scan rate	**Pure-VACNTs**		**VA-N-doped CNTs**	
(mV s-1)	0 ALD cycles	600 ALD cycles	0 ALD cycles	600 ALD cycles
5	8.14	78.62	2.05	4.76
10	8.00	69.02	1.65	4.06
20	7.85	67.96	1.51	3.83
50	7.66	66.60	1.40	3.27
100	7.44	60.38	1.39	2.87

The electrochemical performance of the electrodes reaches a maximum at 600 ALD cycles with the pure-VACNTs/Mn_3O_4 nanocomposite electrode. Compared with the VA-N-doped-CNTs/Mn_3O_4 nanocomposite, the specific capacitance of pure-VACNTs/Mn_3O_4 nanocomposite increased profoundly. All the CV curves show ideal capacitive behavior, even at 100 mV s^{-1}, revealing good electrochemical reversibility of the electrodes. To

investigate in detail the capacitive behavior of the different electrodes materials, galvanostatic charge/discharge (GCD) analysis was also conducted at different current densities, as shown in Figure VI.6. The charge curves of uncoated pure-VACNTs and uncoated VA-N-doped CNTs are nearly symmetrical with their discharge counterparts revealing an excellent electrochemical reversibility and charge-discharge properties. However, a small potential drop (IR drop) is observed at the very beginning of the discharge curve of the VA-N-doped CNTs (Figure VI.6c). This phenomenon is usually associated with equivalent series resistance (ESR) of the electrode at the beginning of discharge [17,18]. In addition, the discharge time is decreased with increasing current densities due to the insufficient accessible time of electrolyte ions to the electrodes. The shape GCD of the discharge curves of that pure-VACNTs/Mn_3O_4 and VA-N-doped-CNTs/Mn_3O_4 nanocomposites after 600 ALD cycles show the characteristics of both electric double layer capacitor and pseudocapacitance, which is in agreement with the results of the CV curves. Whereas the pseudocapacitance contributions from redox active Mn_3O_4 induces deviation from linearity in charge discharge curves [19].

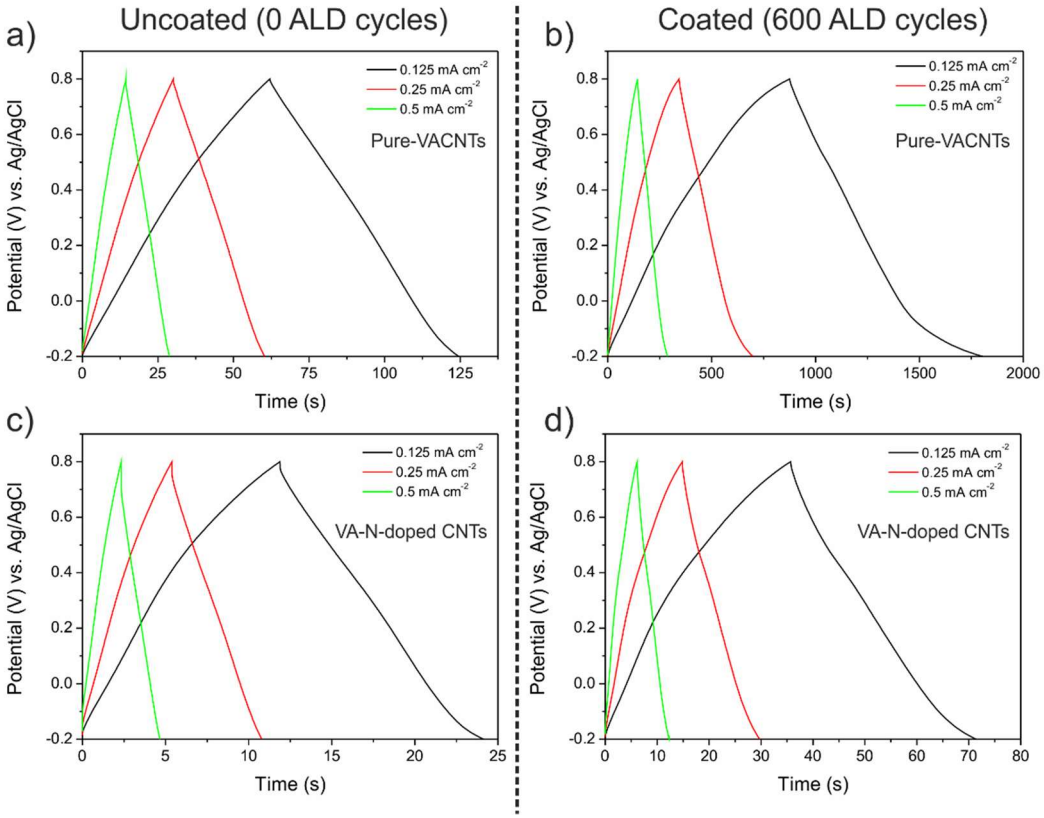

Figure VI.6. Galvanostatic charge-discharge curves at different current densities, of the different electrodes materials.

The specific capacitance (C_{sp}) can also be calculated from the GCD curves at different current densities. The calculated specific capacitances of the different electrodes materials

are summarized in Table VI.2. It is clear that the uncoated pure-VACNTs and pure-VACNTs/Mn_3O_4 nanocomposite have the larger specific capacitance, as calculated from the GCD curves. The maximum specific capacitance of 78.62 mF cm^{-2} and 117 mF cm^{-2} was obtained at 5 mV s^{-1} and 0.125 mA cm^{-2}, respectively, for the pure-VACNTs/Mn_3O_4 nanocomposite after 600 ALD cycles. This result is a nice demonstration of a synergy between the VACNTs and the Mn_3O_4 coating, since both contribute to the total specific capacitance. Further increase in ALD cycles the Mn_3O_4 can eventually become an electrically insulator coating decreasing the electron transport.

Table VI.2. Specific capacitance (C_{sp}) calculated from the GCD curves, at different current densities.

	Specific capacitance (C_{sp}) (mF cm^{-2})			
Current density (mA cm^{-2})	**Pure-VACNTs**		**VA-N-doped CNTs**	
	0 ALD cycles	600 ALD cycles	0 ALD cycles	600 ALD cycles
0.125	7.87	117.10	1.55	4.48
0.25	7.65	89.57	1.42	3.78
0.5	7.36	78.13	1.29	3.16

It is worthy to mention that the specific capacitance obtained from CV curves is comparable to the data calculated from GCD measurements. However, a small variation was observed in specific capacitance of the samples determined by GCD and CV. This can be explained by the fact that the value of specific capacitance measured by CV in one particular potential, at the same time that obtained by GCD is an average capacitance over the potential range of -0.2 to 0.8 V. Indeed, averaging the capacitance in a voltage range leads to the variation of specific capacitance [20].

The main objective of the electrochemical impedance (EIS) measurements is to gain insight of the resistive and capacitive elements associated to the electrode materials. The electrode behaves as a resistor and capacitor at high and low frequency, respectively. From Figure VI.7, it is clear that the Nyquist plot, of both nanocomposites exhibit a vertical line along the imaginary axis in the low frequency region, implying a close to ideal capacitive behavior of the two nanocomposites with low resistance.

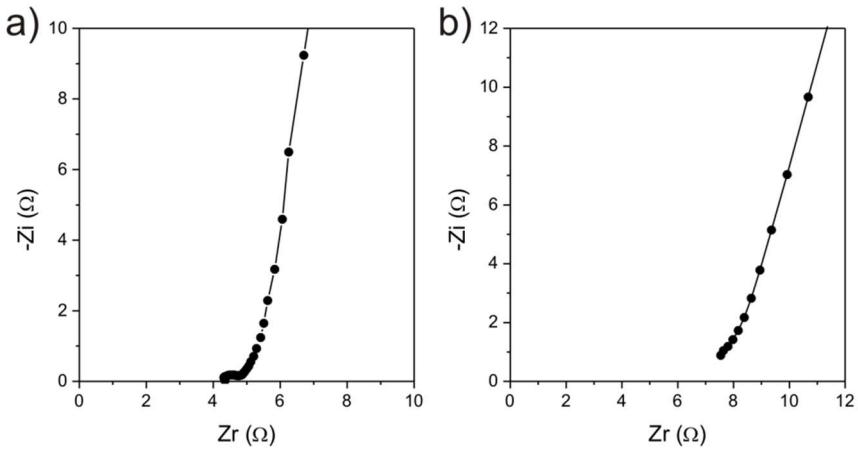

Figure VI.7. Nyquist plot of pure-VACNTs/Mn_3O_4 (a) and VA-N-doped-CNTs/Mn_3O_4 (b) nanocomposites after 600 ALD cycles.

The equivalent series resistance (ESR) obtained from the intersection of the Nyquist plot at x-axis is estimated to around 4.4 Ω and 7.5 Ω for pure-VACNTs/Mn_3O_4 and VA-N-doped-CNTs/Mn_3O_4 nanocomposites, respectively. These measured resistances include the sum of electrolyte resistance and contact resistance between the nanotubes and the current collector. Despite the fact that the sight difference in the ESR values of the two nanocomposites, the relatively low values is a consequence of the vertically aligned architecture of the nanotubes, and the good contact between the nanotubes and the Inconel®600 substrate.

The cyclic charge-discharge test is one of the important aspects to understanding the stability and service life of the capacitor for their practical applications. This test was carried up to 600 cycles of charge-discharge at 0.50 mA cm^{-2} for pure-VACNTs/Mn_3O_4 VA-N-doped CNTs/Mn_3O_4 nanocomposites electrodes materials to evaluate their stability as supercapacitor electrode material, as shown in Figure VI.8.

The insets show four galvanostatic charge-discharge cycles of both nanocomposites at a current density of 0.50 mA cm^{-2} exhibits repeated; almost identical triangular curves shapes. These results demonstrate that the hierarchical structure of both nanocomposites is very stable in the repeated cycles as supercapacitor electrodes materials with capacitance retention capability. Despite of the fact that the low values of specific capacitance, the VA-N-doped CNTs/Mn_3O_4 nanocomposite present an improved relative stability during the cycling test without any significantly changes of capacitance. In contrast, during the first 300 cycles the pure-VACNTs/Mn_3O_4 nanocomposite, the specific capacitance decrease slightly but then is maintained for the following cycles.

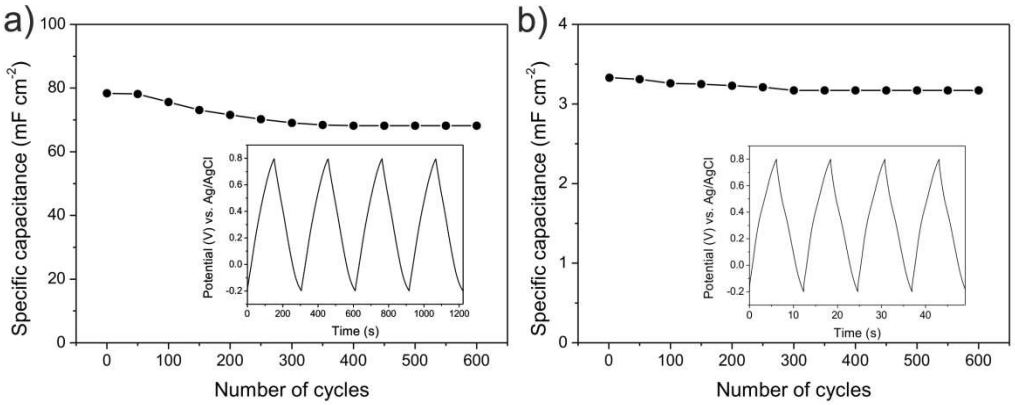

Figure VI.8. Cycling stability test of: pure-VACNTs/Mn_3O_4 (a) and VA-N-doped CNTs/Mn_3O_4 (b) nanocomposites.

One possible reason for the different electrochemical results between nanocomposites can be attributed to the final dimension of the coated nanotubes (size-effect of the nanotubes arrays). For instance, the uncoated N-doped CNTs possess a higher outer diameter size range (20-100 nm) in direct comparison with uncoated pure-CNTs (14-18 nm). In opposition, the length of the pure-VACNTs array (20.8 μm) is clearly higher than that of VA-N-doped CNTs array (5.5 μm), which can be directly associated with TCVD growth process.

From the point of view of the conformal Mn_3O_4 coating thickness, it was found that the estimated thicknesses from the STEM measurements on the coated pure- and N-doped CNTs (Figure V.I.4e,g) were 13.1 nm and 20.4 nm, respectively.

Since ALD is based on the on the self-terminated chemical reactions and the number of ALD cycles was fixed, the Mn_3O_4 deposition was mainly affected by the surface properties of both types the nanotubes. As a result, the Mn_3O_4 thickness greatly influences the electrochemical behavior of the nanocomposites electrodes and therefore it impacts on the obtained specific capacitance. Another, interesting approach would be to use water as oxygen source instead of ozone. In this case the ozone was applied not only as the oxygen source but also for the *in situ* functionalization of the CNTs. This modification of the oxygen source would lead certainly to an understanding of the effect of nitrogen incorporation into the VA-N-CNTs graphitic network towards the ALD of manganese oxide for the fabrication of the nanocomposites used as electrodes materials.

According to these remarks, it is reasonable to suggest that the pure-VACNTs offer a larger surface area for the Mn_3O_4 coating and thereby better utilization of the electrochemically active materials leading to an enhancement of the overall electrochemical performance.

Additionally, both types of vertically aligned nanotubes provide a good supporting "scaffolds" (3D current collector) for ALD of Mn_3O_4. Figure VI.9 shows the CV curves of the different electrodes. A more rectangular-like shape of CV is observed for pure-VACNTs as compared with the VA-N-doped CNTs, indicating a more ideal capacitor character. The increase in the area under CV curves is observed when the Mn_3O_4 component (100 ALD cycles) was integrated with pure- and N-doped-CNTs forming two different nanocomposites electrodes. In these nanocomposites, the vertically aligned nanotubes offered conductive pathway and supported the ALD of Mn_3O_4. The much lower current response of the Mn_3O_4 thin film (100 ALD cycles supported on planar Inconel®600 foil) highlights the importance of the vertically aligned nanotubes conductive network on the nanocomposite electrode.

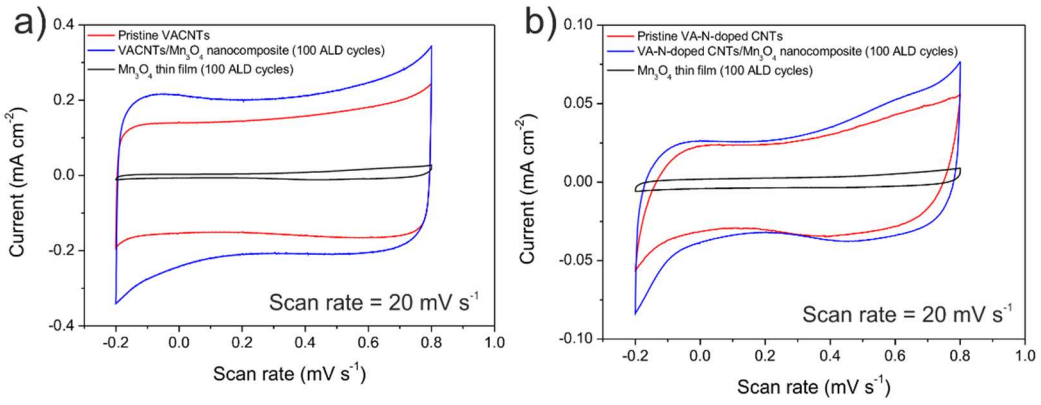

Figure VI.9. CV curves of the different electrodes: (a) pure-VACNTs, VACNTs/Mn_3O_4 nanocomposite, Mn_3O_4 thin film and (b) VA-N-doped CNTs, VA-N-doped CNTs/Mn_3O_4 nanocomposite, Mn_3O_4 thin film, at a constant rate of 20 mV s^{-1}. These results demonstrate the combined merits from the conductive network of vertically aligned nanotubes and the ALD Mn_3O_4coating.

In summary, the electrochemical studies demonstrated that the nanocomposite electrode exhibited significant increment of specific capacitance than that of uncoated CNTs, principally due to the contribution pseudocapacitive properties of the ALD of Mn_3O_4 coating. The nanocomposite electrode also demonstrated good capacitance retention upon cycling.

VI.4. Conclusions

Based on the above discussed results, it can be conclude that pure-VACNTs/Mn_3O_4 and VA-N-doped-CNTs/Mn_3O_4 nanocomposites after 600 ALD cycles are very stable with a good dynamic charge-discharge response characteristic, as supercapacitors electrode materials. As a matter of fact the increased specific capacitance of the both CNTs/Mn_3O_4

nanocomposites over both uncoated CNTs can be attributed to the synergetic effect between the EDLC-active CNTs and the redox-active Mn_3O_4. Apart from acting as an EDLC source, the CNTs also develop a conductive network path throughout the nanocomposite increasing the exposed electrochemically active surface area for redox reactions and facilitating the electron transfer reactions. Nevertheless, it was observed that the uncoated VACNTs arrays demonstrated a better electrochemical behavior in comparison with the uncoated VA-N-doped CNTs arrays in this particularly configuration of binder-free design electrode. On the other hand, VA-N-doped CNTs as a support were found to increase the cycling stability of the VA-N-doped-CNTs/Mn_3O_4 nanocomposite.

From a materials perspective, the pure-VACNTs and VA-N-doped CNTs architecture has great potential for supercapacitors applications, especially when combine with other pseudocapacitive metal oxides such as MnO_2, V_2O_5 and Co_3O_4. Therefore a nanocomposite material comprising electric double layer capacitance as well as conductive framework of the CNTs and pseudocapacitive metal oxides is of great interest due to its dual charge storage mechanism and the advantages of each mechanism are exploited in hybrid devices. Indeed, it is critical to develop ways of synthesizing new nanostructured materials with enhanced properties or combination of properties to meet future challenges in energy storage systems.

References

[1] H. Zhang, G. Cao, Y. Yang, *Energy Environ. Sci.* **2009**, *2*, 932.

[2] P. Ayala, R. Arenal, M. Rümmeli, A. Rubio, T. Pichler, *Carbon* **2010**, *48*, 575.

[3] D.S. Su, R. Schlögl, *ChemSusChem* **2010**, *3*, 136.

[4] J.P. Paraknowitsch, A. Thomas, *Energy Environ. Sci.* **2013**, *6*, 2839.

[5] S. Talapatra, S. Kar, S.K. Pal, R. Vajtai, L. Ci, P. Victor, M.M. Shaijumon, S. Kaur, O. Nalamasu, P.M. Ajayan, *Nat. Nanotechnol.* **2006**, *1*, 112.

[6] M. Inagaki, H. Konno, O. Tanaike, *J. Power Sources* **2010**, *195*, 7880.

[7] X. Meng, Y. Zhong, Y. Sun, M.N. Banis, R. Li, X. Sun, *Carbon* **2011**, *49*, 1133.

[8] C. Chen, B. Liang, D. Lu, A. Ogino, X. Wang, M. Nagatsu, *Carbon* **2010**, *48*, 939-948.

[9] R.M. Silva, A.J.S. Fernandes, M.C. Ferro, N. Pinna, R.F. Silva, *Appl. Surf. Sci.* **2015**, *344*, 57.

[10] J. Bao, N. Kishi, I. Khatri, T Soga, *Mater. Lett.* **2013**, *113*, 114.

[11] R.M. Silva, A.C. Bastos, F.J. Oliveira, D.E. Conte, Y.F. Fan, N. Pinna R.F. Silva, *J. Mater. Chem. A* **2015**, *3*, 17804.

[12] R.M. Silva, G. Clavel, Y. Fan, P. Amsalem, N. Koch, R.F. Silva and N. Pinna, *Adv. Mater. Interfaces* **2016**, *1600313* (1 of 8).

[13] L. Laffont, P. Gibot, *Mater. Charat.* **2010**, *61*, 1268.

[14] M. Pourbaix, *Atlas of Electrochemical Equilibria in Aqueous Solutions, National Association of Corrosion Engineers*, Houston, TX, (**1996**).

[15] M. Toupin, T. Brousse, D. Belanger, *Chem. Mater.* **2004**, *16*, 3184.

[16] W. Chen, R.B. Rakhi, Q. Wang, M.N. Hedhili, H.N. Alshareef, *Adv. Funct. Mater.* **2014**, *24*, 3130.

[17] B.E. Conway, in *Electrochemical Supercapacitors: Scientific Fundamentals and Technological Applications*, Plenum, New York, **1999**.

[18] S. Zhang, N. Pan, *Ad. Energy Mater.* **2014**, *1401401*, (1 of 19).

[19] S. Bose, T. Kuila, A. K. Mishra, R. Rajasekar, N. H. Kim, J. H. Lee, *J. Mater. Chem.* **2012**, *22*, 767.

[20] T.L. Kelly, K. Yano, M. O. Wolf, *Appl. Mater. Interfaces* **2009**, *1*, 2536.

Chapter VII

Chapter preface

This final chapter describes the main conclusions regarding the results obtained under this PhD thesis. The obtained results highlight the versatility of the experimental approach to elaborate nanocomposite electrodes for electrochemical capacitors as well as their advanced characterization and classification in accordance with energy storage mechanism. Our results also verify the usefulness of ALD in nanofabrication and surface engineering of nanoscale materials.

VII. Main conclusions

The controlled growth and deposition of metal oxide coatings on a variety of supports has tremendous implications not only in fundamental science but also in applied research. Atomic layer deposition (ALD) technique emerges as a promising approach to respond to these demands. This process results in a unique combination of attributes, including sub-nm precision, the capability to engineer surfaces and interfaces, and unparalleled conformality over high-aspect ratio structures.

This thesis is focused not only on the elaboration of electrochemical active development of hybrid 3D-arrays of vertically aligned carbon nanotubes coated with transition metal oxides, using ALD, but also on their advanced characterization. As result, a tree-dimensional array of metal oxide-carbon nanotube electrode is obtained. Particular emphasis was placed on the heterostructures characterization, especially on the interface between the two materials.

In the first stage, the main efforts were devoted to the growth of pure- and nitrogen doped-vertically aligned carbon nanotubes arrays on nonmetallic and metallic substrates by thermal chemical vapor deposition (TCVD). In view of the elaboration of the hybrid 3D-arrays of vertically aligned carbon nanotubes coated with transition metal oxides for application as binder-free electrodes in electrochemical capacitors, the vertical alignment of the nanotubes arrays is highly desirable because it offers an ideal nanostructure to maximize the exposed active surface area at electrode/electrolyte interfaces.

We were able to grow for the first time pure-VACNTs directly on Inconel®600, without the employment of any additional catalyst, which was used as metallic current collector allowing to directly use the pure-VACNTs as electrodes for supercapacitors applications. The electrochemical performance of theses carbon-based electrodes was assessed through the demonstration of cyclic voltammetry (CV) measurements of more than 1000 cycles without the noticeable performance degradation demonstrating the robustness of the above synthesis approach. In addition, a detailed description how the pure-VACNTs arrays are grown was carried out by means of different characterization techniques. Afterwards, this synthesis approach was also extended to the growth of VA-N-doped CNTs.

Subsequently, as one of the main points of this study, a novel manganese oxide (Mn_3O_4) atomic layer deposition (ALD) process has been developed for the coating of the carbon nanotubes arrays aiming the elaboration of heterostructures, which were further used and characterized as electrodes materials. As a result, the nanotubes were coated with a conformal granular layer of manganese oxide leading to the formation of a VACNTs/Mn_3O_4 nanocomposite electrode.

The electrochemical analysis showed excellent capacitive and cycling performance of the different carbon nanotubes/metal oxide nanocomposites. The reason for this can be well

understood if the following factors are considered. First, VACNTs arrays are directly grown on the Inconel®600, enhancing the connection between the nanotubes and the metallic current collector substrate. Such connection provides better and fast electron transport from the nanotube to the current collector. Second, the large surface area of 3D nanotube architecture favors the efficient contact between active materials and electrolyte, providing more active sites for electrochemical reactions. Third, the excellent electrochemical performance is a result of the synergetic effect of the carbon nanotubes/metal oxide unique 3D architecture. Moreover, this work also validates the nanocomposite approach for the design and elaboration of new electrochemical devices using heterogeneous nanocomposite materials.

In parallel to the nanocomposite electrodes fabrication and characterization, the surface modification of vertically aligned carbon nanotubes by *in situ* functionalization through nitrogen (N) incorporation during CNTs growth process (i.e. thermal chemical vapor deposition (TCVD) method) was carried out . This type functionalization is not a separate step from the CNT growth itself and does not decrease significantly the crystallinity of the TCVD grown nanotubes. In contrast, the conventional wet oxidation of the carbon nanotubes reported in the literature introduces two main disadvantages. First, the harsh conditions damage the structure of the CNT array such as collapse of the vertical alignment and peeling off from substrate. Second, the oxidation of the carbon nanotubes surface lead to a degradation of the electrical properties due to the large increase of oxygen content or even the breaking of the nanotubes. Nevertheless, in order to break down the chemically inert nature of the nanotubes making them chemically active, a functionalization step of the CNTs is frequently used, especially, for producing hybrid nanostructures. Our TCVD process has produced VA-N-doped CNTs with different N content incorporated into the graphitic network of the CNTs. As a matter of fact, a strong correlation between the N incorporation and morphology of the nanotubes is observed with the use of high resolution electron microscopy. One of the important advantages of N doping of the CNTs is the creation of surface defects i.e. N species or moieties. Particularly, this N species acted as active and nucleation sites during the metal oxide deposition via ALD. In this context, we used the ALD technique as an indirect probing tool of the surface defects generated by the incorporation of N atoms in the graphitic network of the CNTs, combined with high resolution electron microscopy techniques. Therefore, we focused on the ALD of ZnO because it is a well-established and yet simple chemical process, without other side reactions that can further complicate the study of the nucleation and growth onto N-doped CNTs. In this manner, the reaction between the metal precursor (diethylzinc) and surface species (i.e. N species), which played a critical role to initiate the film nucleation, was investigated. As a result, the as-prepared VA-N-doped CNTs arrays provide the necessary density of defects to obtain a conformal and uniform coating of ZnO. On the other hand the ZnO coating morphology could be controlled by the number of ALD ZnO cycles and perhaps also by the variation of the N content. Furthermore, this fundamental

understanding of nucleation and growth phenomena is of great interest for the design and engineering of functional heterostructures.

In view of what has been discussed above, the proposed *in situ* functionalization of the CNTs is an effective alternative and non-destructive strategy to the the classical wet oxidation pathways without sacrificing the quality of CNTs.

Finally, this work is the starting point for future studies devoted to the combination of VACNTs arrays supported on conductive Inconel®600 substrate with other transition metal oxides for the fabrication of nanocomposites electrodes. We foresee that, this type of hybrid nanostructure design, consisting on hierarchical CNTs arrays coated by atomic layer deposition with metal oxides, which can offer richer redox chemistry, shows a great potential for future electrochemical energy storage systems, bringing new opportunities for a wide range of applications. For instance, the supercapacitors should be embed appropriately with other electronic devices, creating multifunctional or self-powered hybrid systems. Additionally, CVD and ALD proved to be very versatile techniques for developing this type of hybrid nanostructures.

Regarding the environmental concerns it is of great interest to have research oriented towards the development of sustainable and "green materials", which are earth abundant, renewable, recyclable and non-toxic for supercapacitor designing and therefore minimizing the environmental impact of manufacturing process.

Appendix

Publications in the framework of this thesis

R.M. Silva, G. Clavel, Y. Fan, P. Amsalem, N. Koch, R.F. Silva and N. Pinna, *Adv. Mater. Interfaces* **2016**, *1600313* (1 of 8).

R.M. Silva, M.C. Ferro, J.R. Araujo, C.A. Achete, G. Clavel, R.F. Silva, N. Pinna, *Langmuir* **2016**, *32*, 7038-7044.

R.M. Silva, A.C. Bastos, F.J. Oliveira, D.E. Conte, Y. Fan, N. Pinna, R.F. Silva, *J. Mater. Chem. A* **2015**, *3*, 17804-17810.

R.M. Silva, A.J.S. Fernandes, M.C. Ferro, N. Pinna, R.F. Silva, *Appl. Surf. Sci.* **2015**, *344*, 57-64.

Other publications

A. Jaggernauth, R.M. Silva, M.A. Neto, M.J. Hortigüela, G. Gonçalves, F.J. Oliveira, R.F. Silva, M. Vila, *J. Phys. Chem. C* **2016**, *120*, 24176-24186.

M.A.O. Lourenço, R.M. Silva, R.F. Silva, N. Pinna, S. Pronier, J. Pires da Silva, M.L. Pinto, J.R.B Gomes, P. Ferreira, *J. Mater. Chem. A* **2015**, *3*, 22860-22867.

R.M. Silva, A. Pucci, C. Marichy, D. Mata, M.C. Ferro, R.F. Silva, N. Pinna, *Cryst. Eng. Comm.* **2012**, *14*, 48-52.

D. Mata, R.M. Silva, A.J.S. Fernandes, F.J. Oliveira, P.M.F.J. Costa, R.F. Silva, *Carbon* **2012**, *50*, 3585-3606.